TROPICAL PRECIPITATION SIMULATED BY THE NCAR COMMUNITY CLIMATE MODEL (CCM3): AN EVALUATION BASED ON TRMM SATELLITE MEASUREMENTS

A Dissertation

by

JONATHAN CRAIG COLLIER

Submitted to the Office of Graduate Studies of
Texas A&M University
in partial fulfillment of the requirements for the degree of

DOCTOR OF PHILOSOPHY

August 2004

Major Subject: Atmospheric Sciences

TROPICAL PRECIPITATION SIMULATED BY THE NCAR COMMUNITY CLIMATE MODEL (CCM3): AN EVALUATION BASED ON TRMM SATELLITE MEASUREMENTS

A Dissertation

by

JONATHAN CRAIG COLLIER

Submitted to Texas A&M University
in partial fulfillment of the requirements
for the degree of

DOCTOR OF PHILOSOPHY

Approved as to style and content by:

Kenneth P. Bowman
(Chair of Committee)

Gerald R. North
(Member)

Thomas T. Wilheit
(Member)

H. Joseph Newton
(Member)

Richard E. Orville
(Head of Department)

August 2004

Major Subject: Atmospheric Sciences

ABSTRACT

Tropical Precipitation Simulated by the NCAR Community Climate Model (CCM3): An Evaluation Based on TRMM Satellite Measurements. (August 2004)

Jonathan Craig Collier, B.S., University of Southern Mississippi;
M.S., Texas A&M University
Chair of Advisory Committee: Dr. Kenneth P. Bowman

This study evaluates the simulation of tropical precipitation by the Community Climate Model, Version 3, developed at the National Center for Atmospheric Research. For an evaluation of the annual cycle of precipitation, monthly-mean precipitation rates from an ensemble of CCM3 simulations are compared to those computed from observations of the TRMM satellite over a 44-month period. On regional and sub-regional scales, the comparison fares well over much of the Eastern Hemisphere south of 10°S and over South America. However, model - satellite differences are large in portions of Central America and the Caribbean, the southern tropical Atlantic, the northern Indian Ocean, and the western equatorial and southern tropical Pacific. Since precipitation in the Tropics is the primary source of latent energy to the general circulation, such large model - satellite differences imply large differences in the amount of latent energy released. Differences are seasonally-dependent north of 10°N, where model wet biases occur in realistic wet seasons or model-generated artificial wet seasons. South of 10°N, the model wet biases exist throughout the year or have no recognizable pattern.

For an evaluation of the diurnal cycle of precipitation, hourly-averaged precipitation rates from the same ensemble of simulations and for the same 44-month period are compared to observations from the Tropical Rainfall Measuring Mission (TRMM) satellite. Comparisons are made for 15° longitude × 10° latitude boxes and for larger geographical areas within the Tropics. The temporally- and spatially-averaged hourly precipitation rates from CCM3 and from TRMM are fit to the diurnal harmonic by the method of linear least-squares regression, and the phases and the amplitudes of the diurnal cycles are compared. The model's diurnal cycle is too strong over major land masses, particularly over South America (by a factor of 3), and is too weak over many oceans, particularly the northwestern Tropical Pacific (by a factor of 2). The model-satellite phase differences tend to be more homogeneous. The peak in the daily precipitation in the model consistently precedes the observations nearly everywhere. Phase differences are large over Australia, Papua New Guinea, and Saharan Africa, where CCM3 leads TRMM by 4 hours, 5 to 6 hours, and 9 to 11 hours respectively. A model sensitivity experiment shows that increasing the convective adjustment time scale in the model's deep convective parameterization reduces its positive amplitude bias over land regions but has no effect on the phase of the diurnal cycle.

ACKNOWLEDGMENTS

This material is based upon work supported by a NASA Earth System Science fellowship and by NASA grant NAG5-4753 to Texas A&M University. The author thanks the Goddard Space Flight Center for making the TRMM satellite data available online via the TRMM Science Data and Information System; the Community Climate Model group at NCAR for developing and assistance with running CCM3; and the Program for Climate Model Diagnosis and Intercomparison at Lawrence Livermore National Laboratory for providing the sea-surface temperature data set in CCM3 format. The author appreciates the guidance of his advisory committee as well as the thoughtful suggestions of anonymous reviewers who helped bring the two papers, which comprise this dissertation, to publication.

TABLE OF CONTENTS

CHAPTER Page

I INTRODUCTION 1

II THE NCAR COMMUNITY CLIMATE MODEL, VERSION 3 . . . 3

- A. Conservation of Momentum, Energy, Mass, and Water Vapor . . 3
- B. Discretization 7
- C. Physical Parameterizations 10
  - a. Deep convection 10
  - b. Shallow and mid-level convection 19
  - c. Large-scale stable condensation 21

III THE TROPICAL RAINFALL MEASURING MISSION (TRMM) SATELLITE 23

IV METHODS 26

- A. TRMM Data 26
- B. GCM Simulations 27

V RESULTS 30

- A. Comparison of Annual Cycles 30
  - a. Region A: the central and eastern Pacific 39
  - b. Region B: Central America, the Caribbean, the Gulf of Mexico, and the far eastern Pacific 40
  - c. Region C: South America and the Tropical Atlantic 42
  - d. Region D: Northern Africa and Southern Asia 44
  - e. Region E: the Maritime Continent and the Western Tropical Pacific 47
  - f. Region F: the Southern Eastern Hemisphere 49
  - g. Summary 50
- B. Comparison of Diurnal Cycles 54
  - a. Harmonic analysis 57
  - b. Summary 83

VI A MODEL SENSITIVITY STUDY 87

CHAPTER Page

VII SUMMARY AND CONCLUSIONS 103

REFERENCES 107

VITA 116

LIST OF FIGURES

FIGURE Page

1 Illustration of the vertical structure of CCM3. 8

2 Illustration of the (Zhang and McFarlane 1995) parameterization for deep convection in CCM3. 14

3 Illustration of the (Hack 1994) parameterization for shallow and mid-level convection in CCM3. 20

4 Diagram showing how the CCM3 simulation ensemble was generated. Note that the record of TRMM data, which begins in November, 1997, continues as of this writing. 29

5 Map of the 48 regions of comparison (a) and monthly-mean precipitation rates in mm day^{-1} for January, 1998 - August, 2001 as simulated by the 8 members of the CCM3 ensemble for 14W (b) and 15E (c). Gray curves represent the individual member means, and the heavy black curve represents the ensemble mean. 31

6 Climatological annual-mean precipitation rate in mm day^{-1} as simulated by CCM3 (a) and as observed by TRMM (TMI+PR) (b) for the period 1 January 1998 - 31 August 2001. The climatological mean difference (CCM3-TRMM) is plotted in (c). 33

7 Precipitation rates (mm day^{-1}) simulated by CCM3 (top) and those estimated by TRMM (TMI+PR) data (bottom) averaged over the four meteorological seasons, from 1998 - 2001. 34

8 Time series of CCM3 and TRMM monthly-mean precipitation rates in mm day^{-1} as from January, 1998 through August, 2001 for 48 separate regions in the Tropics. CCM3 ensemble-average mean: solid, TRMM mean: dash. 36

9 CCM3 (solid) and TRMM (dashed) monthly-mean precipitation rates in mm day^{-1} for the southern Tropical Pacific Ocean (boxes 5W, 11W, and 12W of Figure 8(a)). 40

FIGURE Page

10 Same as in Figure 9 except for the Central American-Caribbean-far eastern Pacific region (boxes 7W, 8W, 9W, 13W, and 14W of Figure 8(a)). 41

11 Same as in Figure 9 except for the southern tropical Atlantic region (boxes 22W and 23W of Figure 8(a)). 43

12 Same as in Figure 9 except for the equatorial Africa region (boxes 2E (southern half) and 3E of Figure 8(b).) 45

13 Same as in Figure 9 except for the south-central Asia - northern Indian Ocean region (boxes 7E - 10E and western portions of boxes 13E and 14E of Figure 8(b).) 46

14 Same as in Figure 9 except for the northwestern tropical Pacific Ocean region (boxes 19E and 20E of Figure 8(b).) 48

15 Same as in Figure 9 except for the western equatorial Pacific Ocean region (boxes 21E and 22E of Figure 8(b).) 49

16 Categorical absolute (a) and relative differences (b) between CCM3 and TRMM total precipitation for the 44-month comparison period. Types of model - satellite differences are plotted in (c), where a + or a - refers to the model's wet or dry bias respectively. Each location corresponds to one of the subregions examined above. 51

17 Bar charts representing the magnitudes of 44-month total precipitation in cm y^{-1} as simulated by CCM3 and as observed by TRMM. The CCM3 precipitation bar (on the left) is partitioned into a convective part (black) and large-scale stable part (white). The percentage of the CCM3 precipitation that is convective is written above the CCM3 bar. The TRMM (TMI+PR) precipitation bar is shown in dark gray. 53

18 Scatter plots of CCM3 and TRMM regional-mean monthly-mean precipitation rates (mm day^{-1}) for Northern Hemisphere (a), Southern Hemisphere (b), ocean (c), and land (d) regions. Rank correlation coefficients are printed in the lower right-hand corner of each plot. The solid black line represents the line of unit correlation. 55

FIGURE Page

19 Map of the 144 regions used for the diurnal cycle comparison. Climatological-mean hourly precipitation rates from CCM3 and from TRMM are averaged over each of the above regions. Note that the grid appears irregular due to the fact that the region boundaries were chosen to line up with the model's grid, which is irregularly spaced. 58

20 Number of samples by the TRMM satellite of the diurnal cycle of precipitation for the 144 regions used in the comparison. The period spans 44 months, from January, 1998 through August, 2001. 59

21 The TRMM (top left) and CCM3 (top right) climatological-mean hourly precipitation as a fraction of daily mean (solid) and the diurnal harmonic fit (dashed) for region 12B. In the bottom panel, the phases and amplitudes of the diurnal cycles are represented by arrows (CCM3: heavy; TRMM: light) and uncertainty circles (CCM3: solid; TRMM: dashed). A circle which surrounds the arrow's origin indicates that the diurnal harmonic fit is not significant at the 5% level. For clarity, the arrows and associated uncertainty circles have been scaled by a common scale factor. 62

22 Phase of the climatological-mean diurnal cycle for regions between the International Date Line and 90°W (CCM3: heavy arrow; TRMM: light arrow), with associated circles of uncertainty. 64

23 Map showing the boundaries of the two zones between the International Date Line and 90°W over which CCM3 and TRMM hourly precipitation rates were averaged for comparison. 66

24 The TRMM and CCM3 climatological-mean hourly precipitation for the northeastern Tropical Pacific Ocean zone (a) and for the southeastern Pacific Ocean zone (b), expressed as a fraction of daily mean (solid) with its diurnal harmonic fit (dashed) on the left. On the right, the phases and amplitudes of the diurnal harmonic fits are expressed in arrow-uncertainty circle format (CCM3: heavy arrow, solid circle; TRMM: light arrow, dashed circle). 67

25 Same as in Figure 22 except for regions between 90°W and the Prime Meridian. 69

FIGURE Page

26 Map showing the boundaries of the three zones between 90°W and the Prime Meridian over which CCM3 and TRMM hourly precipitation rates were averaged for comparison. 70

27 Same as in Figure 24 except for the South America zone (a), the northern Tropical Atlantic Ocean zone (b), and the southern Tropical Atlantic Ocean zone (c). 72

28 Same as in Figure 22 except for regions between the Prime Meridian and 90°E. 74

29 Map showing the boundaries of the three zones between the Prime Meridian and 90°E over which CCM3 and TRMM hourly precipitation rates were averaged for comparison. 75

30 Same as in Figure 24 except for the northern Africa zone (a), and the southern Africa zone (b). 76

31 Same as in Figure 24 except for the south-central Asia zone (a) and the South Indian Ocean zone (b). 78

32 Same as in Figure 22 except for regions between 90°E and the International Date Line. 79

33 Map showing the boundaries of the zones between 90°E and the International Date Line over which CCM3 and TRMM hourly precipitation rates were averaged for comparison. 81

34 Same as in Figure 24 except for the southeast Asia zone (a), the Maritime Continent zone (b), and the Australia zone (c). 82

35 Same as in Figure 24 except for the northwestern Tropical Pacific Ocean zone (a) and the southwestern Tropical Pacific Ocean zone (b). . . 84

36 Difference between CCM3 and TRMM precipitation rate (mm hr^{-1}) as averaged over DJF, 1998 for four separate values of $\tau = s\tau_0$. 89

FIGURE Page

37 Difference between CCM3 and TRMM precipitation rate (mm hr^{-1}) as averaged over MAM, 1998 for four separate values of $\tau = s\tau_0$. 90

38 Difference between CCM3 and TRMM precipitation rate (mm hr^{-1}) as averaged over JJA, 1998 for four separate values of $\tau = s\tau_0$. 91

39 Difference between CCM3 and TRMM precipitation rate (mm hr^{-1}) as averaged over SON, 1998 for four separate values of $\tau = s\tau_0$. 92

40 Monthly-mean precipitation rates (mm day^{-1}) for 1998 for various western geographical zones in the Tropics. The red curve represents a simulation with $\tau = 0.8\tau_0$, the black curve represents a simulation with $\tau = \tau_0$, the green curve represents a simulation with $\tau = 1.2\tau_0$, and the blue curve represents a simulation with $\tau = 1.5\tau_0$. The dashed black curve represents the TRMM monthly means. Plots are annotated with the relative and absolute differences per year in % and cm y^{-1} respectively. The yellow dot indicates the "best" comparison. 94

41 Same as in Figure 40 except for eastern geographical zones. 95

42 Hourly-mean precipitation rates (mm hr^{-1}) averaged over 1998 for western geographical zones. The red curve represents a simulation with $\tau = 0.8\tau_0$, the black curve represents a simulation with $\tau = \tau_0$, the green curve represents a simulation with $\tau = 1.2\tau_0$, and the blue curve represents a simulation with $\tau = 1.5\tau_0$. The dashed black curve represents the TRMM monthly means. Plots are annotated with the relative differences amplitude (in %). 97

43 Same as in Figure 42 except for eastern geographical zones. 98

44 Hourly-mean precipitation rates (mm hr^{-1} averaged over the 44-month comparison period for western geographical zones. The black curve represents a simulation with $\tau = \tau_0$, the blue curve represents a simulation with $\tau = 1.5\tau_0$, and the dashed black curve represents the TRMM monthly means. Plots are annotated with the relative differences amplitude (in %). 99

FIGURE Page

45 Same as in Figure 44 except for eastern geographical zones. 100

46 Difference between CCM3 and TRMM precipitation rate (mm hr^{-1}) as averaged over 4 three month seasons for 1998-2001 for $\tau = \tau_0$ and $\tau = 1.5\tau_0$. 101

CHAPTER I

INTRODUCTION*

The purpose of this study is to measure the performance of a general circulation model in its simulation of precipitation in the Tropics. The motivations for a model validation of this kind are numerous. Between 30°S and 30°N, vast acreage is devoted to the production of citrus, corn, cotton, rice, wheat, and sugar (Espenshade 1995). According to figures obtained from the Population Reference Bureau, as of mid-2002, over 2.8 billion people were living in the Tropics, 1.5 billion alone in southeast Asia. Residents of the Tropics constitute approximately 45% of the Earth's population of around 6.2 billion (Population Reference Bureau 2003). Thus a large part of the human population benefits from the accurate prediction of long-term changes in precipitation within these latitudes.

Additionally, precipitation in the Tropics is a large source of latent energy. The energy released upon condensation in the Tropics constitutes three-fourths of the energy used to drive the general circulation (Kummerow et al. 1998). Therefore, variability in the horizontal distribution and intensity of tropical convection has global effects, as evidenced in the teleconnections of the El Niño - Southern Oscillation (ENSO) phenomenon. See Ropelewski and Halpert (1987, 1989), Montroy (1997), Mo and Higgins (1998), Lau and Wu (2001), and Adler et al. (2000), among others.

General Circulation Models (GCMs) use Newton's equations of motion and the laws of thermodynamics along with parameterizations for sub-grid scale processes to simulate the atmospheric and oceanic circulations and the land surface. Essentially, they are mod-

---

This dissertation follows the style and format of *Journal of Climate*.

*Parts of Chapters I - V are reprinted from "A Comparison of Tropical Precipitation Simulated by the Community Climate Model (CCM3) with That Measured by the Tropical Rainfall Measuring Mission (TRMM) Satellite" by J. Craig Collier, Kenneth P. Bowman, and Gerald R. North, 2004, *Journal of Climate*, in press, with permission from the technical editor (journals) for the American Meteorological Society.

els of the entire climate system and can be used to assess the impacts of variability in the mean state of the atmosphere. Long simulations (of several tens of years) can be used to predict climate change. Validation studies of the precipitation simulated by GCMs are numerous, many concentrating on specific regions of the Earth. Examples include the studies of (Kirkyla and Hameed 1989) and (Chen et al. 1996) (United States), (Chen and Yen 1994) (Indian monsoon), (Busuioc et al. 1999) (Romania), (Trigo and Palutikof 2001) (Iberian peninsula), and the 32-model intercomparison of (Sperber and Palmer 1996) which examined the simulation of interannual rainfall variability in the Brazilian Nordeste, African Sahel, and the Indian subcontinent.

Since tropical precipitation is so important to the circulation of the atmosphere and thus to the climate system itself, its simulation by these models should be evaluated. This kind of evaluation may be performed by comparing the model with observations. In recent years, an important new dataset has become available, that of the Tropical Rainfall Measuring Mission (TRMM) satellite, which is a joint venture between the U.S. National Aeronautics and Space Administration (NASA) and the Japan National Space Development Agency (NASDA). One of the primary goals of this mission, as stated by (Simpson et al. 1988), is to help modelers of the general circulation know the location and amount of latent energy released in the atmosphere to improve climate modeling (Kummerow et al. 2000). Launched on November 27, 1997, the TRMM satellite orbits at an altitude of approximately 401 km, boosted from an altitude of 350 km in 2001[1], and is equipped with a microwave radiometer and a precipitation radar. The microwave radiometer can infer rainfall rates between roughly 38°S and 38°N, and the precipitation radar can infer rainfall rates between roughly 36°S and 36°N.

---

[1] The data for this study are derived from observations at its pre-boost altitude.

CHAPTER II

THE NCAR COMMUNITY CLIMATE MODEL, VERSION 3

By the early 1980s, the atmospheric general circulation model was becoming increasingly important as a device for modeling the Earth's climate. This three-dimensional model predicts all the atmospheric variables important to climatic processes in the atmosphere and ocean, which requires considerably more computational power than its simpler predecessors, the energy balance model, the radiative-convective model, and the statistical-dynamical model, which are at most 2-dimensional and only predict a few of the variables simulated by a GCM. In 1983, the National Center for Atmospheric Research (NCAR) developed its first atmospheric general circulation model, Community Climate Model Ver. 0. The model is updated every 4 to 5 years, and in 1998, its 4th generation, Community Climate Model Ver. 3, was released.

A. Conservation of Momentum, Energy, Mass, and Water Vapor

A CCM3 simulation is based on equations of motion derived from Newton's Second Law in the inertial reference frame:

$$\sum \mathbf{F} = m\mathbf{a}, \tag{2.1}$$

where $\sum \mathbf{F}$ represents the sum of forces acting to cause the acceleration a (in m s^{-2}) of atmospheric mass m (in kg). The acceleration a can be written as $D\mathbf{U}/Dt$, or the rate of change of velocity (in m s^{-1}) of an atmospheric parcel. The primary forces acting on atmospheric mass are those due to the pressure gradient($F_p = V\nabla p$, where p is in Pascals), the Earth's gravitation ($F_g = m\mathbf{g}*$, where $g*$ is in m s^{-2}), friction (F_f), and, in the inertial reference frame, the centrifugal force ($F_{cent} = m\Omega^2\mathbf{R}$, where Ω is the Earth's rotation rate in rad s^{-1} and R is the the distance of the parcel from the Earth's axis in m,) and the

Coriolis force ($F_{cor} = 2m\mathbf{\Omega} \times \mathbf{U}$). Independent of mass m, Newton's second law becomes an equation of conservation of momentum for the parcel:

$$\frac{D\mathbf{U}}{Dt} = -2\mathbf{\Omega} \times \mathbf{U} - \frac{1}{\rho}\nabla p + \mathbf{g} + \mathbf{F_f}, \tag{2.2}$$

where g includes the effects of the Earth's gravitation and its centrifugal force, which act opposite to each other. Given that $\mathbf{U} = u\hat{i} + v\hat{j}$+w$\hat{k}$, (2.2) can be rewritten as the following three equations of motion:

$$\frac{Du}{Dt} - \frac{uv\tan\phi}{a} + \frac{uw}{a} = -RT\frac{\partial \ln p}{\partial x} + 2\Omega v \sin\phi - 2\Omega w \cos\phi + F_{f,x}, \tag{2.3}$$

$$\frac{Dv}{Dt} + \frac{u^2\tan\phi}{a} + \frac{vw}{a} = -RT\frac{\partial \ln p}{\partial y} - 2\Omega u \sin\phi + F_{f,y}, \tag{2.4}$$

$$\frac{Dw}{Dt} - \frac{u^2 + v^2}{a} = -RT\frac{\partial p}{\partial z} - g + 2\Omega u \cos\phi + F_{f,z}, \tag{2.5}$$

where a is the radius of the Earth, and R is the gas constant and T is the virtual temperature which follow the equation of state: ($p = \rho RT$). A scale analysis shows that many of the terms in equations (2.3) - (2.5) are sufficiently small to be ignored for synoptic scale motions so that the momentum equations can be rewritten

$$\frac{Du}{Dt} - fv = -RT\frac{\partial \ln p}{\partial x} + F_{f,x}, \tag{2.6}$$

$$\frac{Dv}{Dt} + fu = -RT\frac{\partial \ln p}{\partial y} + F_{f,y}, \tag{2.7}$$

and

$$-RT\frac{\partial \ln p}{\partial z} = g. \tag{2.8}$$

By applying $\hat{k} \cdot \nabla\times$ to the sum of equations (2.6) and (2.7) and using (2.8), a compact equation governing the horizontal motion of an atmospheric parcel is derived:

$$\begin{aligned}\frac{\partial(\zeta+f)}{\partial t} &= -\mathbf{U}\cdot\nabla\left(\zeta+f\right)-\left(\zeta+f\right)\left(\nabla\cdot\mathbf{V}\right)\left(\frac{\partial w}{\partial x}\frac{\partial v}{\partial z}-\frac{\partial w}{\partial y}\frac{\partial u}{\partial z}\right)+\\ &\quad \frac{1}{\rho^2}\left(\frac{\partial \rho}{\partial x}\frac{\partial p}{\partial y}-\frac{\partial \rho}{\partial y}\frac{\partial p}{\partial x}\right)+F_\zeta, \qquad (2.9)\end{aligned}$$

where ζ is the vertical component of vorticity ($\nabla\times\mathbf{U}$), and (2.9) is usually called the vorticity equation. Note that for CCM3, whose variables are predicted on values of longitude (λ) and latitude (ϕ), the differentials of x and y in (2.9) are expressed as differentials of λ and ϕ:

$$dx = a\cos\phi d\lambda \qquad (2.10)$$

$$dy = ad\phi. \qquad (2.11)$$

In addition, CCM3 uses a more general vertical coordinate, η, which is monotonic with pressure p, is unity at the surface, is zero at the top of the atmosphere (where pressure is 0), and is η_t at the top of the model. The vertical velocity $D\eta/Dt$ is related to $w = Dz/Dt$ as follows:

$$\frac{D\eta}{Dt} = w\frac{\partial\eta}{\partial z}. \qquad (2.12)$$

Making the above coordinate transformations, the model's version of (2.9) is expressed:

$$\begin{aligned}\frac{\partial\zeta}{\partial t} &= -U\dot{\nabla}\left(\zeta+f\right)-\left(\zeta+f\right)\left(\frac{1}{a\cos\phi}\frac{\partial u}{\partial\lambda}+\frac{1}{a}\frac{\partial v}{\partial\phi}\right)-\left(\frac{1}{a\cos\phi}\frac{\partial\dot{\eta}}{\partial\lambda}\frac{\partial v}{\partial\eta}-\frac{1}{a}\frac{\partial\dot{\eta}}{\partial y}\frac{\partial u}{\partial\eta}\right)+\\ &\quad \frac{1}{\rho^2}\left(\frac{1}{a^2\cos^2(\phi)}\frac{\partial\rho}{\partial\lambda}\frac{\partial p}{\partial\phi}-\frac{1}{a^2\cos\phi}\frac{\partial\rho}{\partial y}\frac{\partial p}{\partial\lambda}\right)+F_\zeta, \qquad (2.13)\end{aligned}$$

where $u = a\cos\phi D\lambda/Dt$ and $v = aD\phi/Dt$. A divergence equation can be obtained by applying the divergence operator ($\nabla\cdot$) to the sum of equations (2.6) and (2.7) to obtain

$$\begin{aligned}\frac{\partial\delta}{\partial t} &= -\nabla^2(E+\Phi)+\left(\frac{\partial v}{\partial\lambda}+\frac{\partial u}{\partial\phi}\right)^2-\hat{k}\cdot(\nabla\times\nabla(\zeta+f))-\nabla\dot{\eta}\cdot\frac{\partial\mathbf{V}}{\partial\eta}+\\ &\left(\nabla\dot{\eta}\frac{\partial}{\partial\eta}\right)(\nabla\cdot\mathbf{V})+\frac{1}{a^2\cos^2(\phi)\rho^2}\left(\frac{\partial\rho}{\partial\lambda}\frac{\partial p}{\partial\phi}+\frac{\partial\rho}{\partial\phi}\frac{\partial p}{\partial\lambda}\right)+F_\delta, \qquad (2.14)\end{aligned}$$

where $\delta = \nabla\cdot\mathbf{U}$, $E = (u^2+v^2)/2cos^2\phi$ is kinetic energy and $\Phi = RT\ln p$ is geopotential.

CCM3 conserves not only momentum but also energy. According to the First Law of Thermodynamics,

$$c_p^*\frac{DT}{Dt}-RT\frac{D\ln p}{Dt}=J, \qquad (2.15)$$

where c_p^* is the specific heat capacity of air at constant pressure(in J K^{-1}), T is temperature (in K), and J is the heating rate (in J s^{-1}). Terms representing the diffusion of temperature ($F_{T,H}$) and frictional heating ($F_{F,H}$) are added to the right-hand side to obtain the model's thermodynamic equation:

$$\begin{aligned}\frac{\partial T}{\partial t} &= -\frac{1}{a\cos^2\phi}\left[\frac{\partial}{\partial\lambda}(u\cos(\phi)T)+\cos(\phi)\frac{\partial}{\partial\phi}(v\cos(\phi)T)\right]+T\delta-\\ &\dot{\eta}\frac{\partial T}{\partial\eta}+\frac{J}{c_p^*}+\frac{\omega RT}{pc_p^*}+F_{T,H}+F_{F,H}, \qquad (2.16)\end{aligned}$$

where $\omega = Dp/Dt$.

Additionally, CCM3 also conserves mass and water vapor[1]. Conservation of mass follows from a continuity equation:

$$\frac{\partial\pi}{\partial t}=-\int_1^{\eta_t}\nabla\cdot\left(\frac{\partial p}{\partial\eta}\mathbf{V}\right)d\eta, \qquad (2.17)$$

where π is surface pressure. Equation (2.17) says that the rate of change of surface pressure (the mass of the atmosphere per unit area) must equal the sum over the atmospheric column of the convergence of all fluxes of mass by the horizontal wind. Conservation of water

---

[1] Ad hoc mass and water vapor correctors are applied at the end of a computational time step to ensure conservation.

vapor follows from an equation for the tendency of specific humidity ($q = m_v/m$, where m_v is the mass of water vapor in kg):

$$\begin{aligned}\frac{\partial q}{\partial t} &= \frac{-1}{a\cos^2(\phi)}\left[\frac{\partial}{\partial\lambda}\left(u\cos(\phi)q\right) + \cos(\phi)\frac{\partial}{\partial\phi}\left(v\cos(\phi)q\right)\right] + \\ &\quad q\delta - \dot{\eta}\frac{\partial q}{\partial\eta} + S, \end{aligned} \tag{2.18}$$

which states that any changes in the mass of water vapor following a parcel must equal the rate of increase due to some source S.

B. Discretization

Linearizing the above equations about a reference state and omitting the diffusion terms, the prognostic equation for an arbitrary variable is written as the sum of a group of linear terms and the sum of a group of nonlinear terms:

$$\frac{\partial\psi}{\partial t} = \sum_i \mathcal{L}_i + \sum_j \mathcal{N}_j. \tag{2.19}$$

Nonlinear terms $\mathcal{N}_j$ are treated with centered differences. Linear terms $\mathcal{L}_i$ are treated implicitly as averages of the values at the next and previous time steps. Temporal derivatives are solved via leapfrog differencing, with a Robert time filter (Robert 1966) applied to derivatives of $\psi = u, v, T, q,$ or π for smoothness of the solution. Vertical derivatives are solved via finite differences, constrained by the requirement that they conserve the global integral of total energy (kinetic + internal) in the absence of any sources and sinks. CCM3 has 18 vertical levels, each representing a single value of η. Each level is indexed by an integer value k, and variable values are predicted on the level interfaces $k - 1/2$, $k + 1/2$, etc. The vertical coordinate, η, is given by terrain-following $\sigma = p/p_s$ coordinates for lower-most levels, by pure pressure (p) coordinates at upper-most levels, and by a hybrid $\sigma - p$ coordinate for levels in between. See Figure 1 for an illustration.

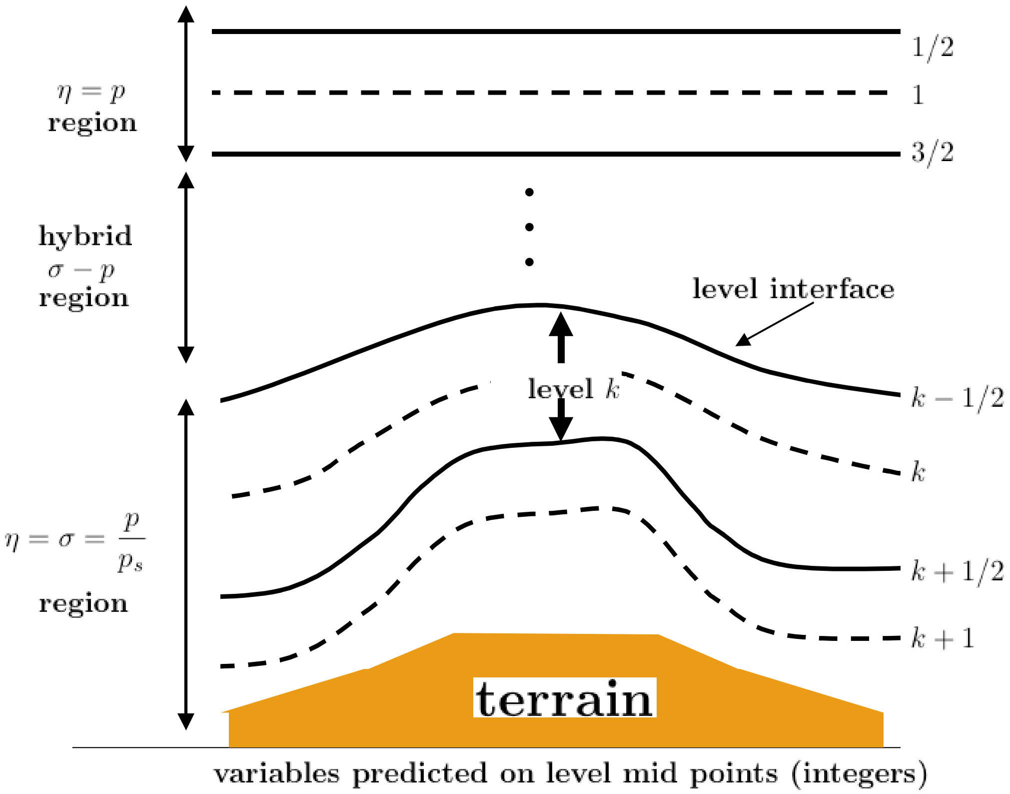

Fig. 1. Illustration of the vertical structure of CCM3.

The horizontal derivatives of terms in $\mathcal{L}_i$ are determined via the spectral transform method. The spectral formulation is more efficient for the computation of gradients Henderson-Sellers (1996). An arbitrary variable, ψ, a function of longitude (λ) and latitude (ϕ) is represented by the following sum:

$$\psi\left(\lambda, \phi\right) = \sum_{m=-M}^{M} \sum_{n=|m|}^{|m|+l} \psi_n^m Y_n^m, \tag{2.20}$$

where ψ_m^n is a complex spectral coefficient, and Y_m^n is a basis function. The basis function appropriate for atmospheric GCMs is the spherical harmonic, which is a function of λ and ϕ as follows:

$$Y_m^n = P_n^m\left(\sin\phi\right)\exp\left(im\lambda\right), \tag{2.21}$$

where P_n^m is a Legendre polynomial of order zero, or one of a set of linearly-independent solutions to Legendre's differential equation:

$$\left(1 - x^2\right) y'' - 2xy' + \gamma y = 0. \tag{2.22}$$

Therefore, ψ is given as

$$\psi\left(\lambda, \phi\right) = \sum_{m=-M}^{M} \sum_{n=|m|}^{|m|+l} \psi_n^m(\sin\phi)\exp\left(im\lambda\right). \tag{2.23}$$

Spectral coefficients $\psi^m(\sin\phi)$ are determined by transform over λ and $\sin\phi$:

$$\psi_n^m\left(\sin\phi\right) = \int_{-1}^{1} \frac{1}{2\pi} \int_0^{2\pi} \psi\left(\lambda, \sin\phi\right)\exp\left(-im\lambda\right) d\lambda, \tag{2.24}$$

where the inner integral (a Fourier Transform) is performed by Fast Fourier Transform (FFT) and the outer integral (a Legendre Transform) is performed by Gaussian quadrature. The limiting indices M and N are the highest Fourier wavenumber and the highest degree of the Legendre polynomial respectively. The most common Fourier wavenumber of truncation used in CCM3 is 42, which is the number used in this study. CCM3 uses a triangular truncation such that $M = N = 42$, which has the advantage of providing a fairly uniform Gaussian grid. The numbers of longitudes and latitudes resulting from this truncation are 128 and 64 respectively, which prescribes a grid spacing of roughly 2.8° by 2.8°.

Lastly, horizontal diffusion terms (F_δ, F_ζ, etc.) are computed implicitly via time splitting after the transformations into spectral space and the solution of the semi-implicit equations. In the top three model levels, a harmonic diffusion operator (∇^2) is used, while in all other model levels, a biharmonic diffusion operator is used (∇^4).

C. Physical Parameterizations

A variety of physical processes important to the climate system vary on length scales which are smaller than those defined by the model's Gaussian grid. Thus the effects of these processes must be represented outside the solution of the above governing equations. A description of the many parameterizations used in CCM3 is deferred to the available literature. For those for clouds, see (Slingo 1987, 1989; Ebert and Curry 1992; Cess 1985; Liou 1992); for radiative fluxes, see (Ramanathan 1976; Ramanathan and Downey 1986); for surface fluxes, see (Holtslag and Boville 1993); for boundary layer height, see (Vogelzang and Holtslag 1996); and for gravity wave drag, see (McFarlane 1987; Lindzen 1992). Parameterizations which are classified as adjustment physics, and which are necessary for the production of precipitation in this model, are discussed below.

a. Deep convection

At the center of the convective parameterizations in CCM3 is the problem of eliminating hydrodynamic instabilities, which are defined based on temperature lapse rates. The means for eliminating the instabilities is convection, or the upward transport of excess sensible and latent energy from the surface. For a model whose smallest length scale is 2.8°, convection and cloud formation is a sub-grid scale (cloud scale) phenomenon, whose contribution to changes in grid-scale (large-scale) energy ($S = c_pT$) and moisture (q) at any location in the atmosphere add to the large-scale contributions in budget equations. In simplest notation, the balances are expressed mathematically as

$$\left(\frac{\partial S}{\partial t}\right) = LSC(S_{ls}) + CSC(S_{cs}) + \epsilon_s \tag{2.25}$$

and

$$\left(\frac{\partial q}{\partial t}\right) = LSC(q_{ls}) + CSC(q_{cs}) + \epsilon_q, \tag{2.26}$$

where LSC is large-scale convergence, expressed generally as

$$LSC(\psi_{ls}) = \nabla \cdot \mathbf{U_{ls}}\psi_{ls}, \tag{2.27}$$

and CSC is cloud-scale convergence, which is typically only important in the vertical:

$$CSC(\psi_{cs}) = \frac{\partial}{\partial z}\left(\dot{\eta}_{cs}\psi_{cs}\right). \tag{2.28}$$

The last term, ϵ, represents large-scale non-dynamical contributions to energy and moisture such as condensation or evaporation. The convective parameterizations describe the cloud-scale contributions (the vertical convergences of cloud-scale vertical transports) in terms of known grid-scale quantities. The parameterization for deep convection in CCM3 is a scheme designed by (Zhang and McFarlane 1995), which was first implemented in the Canadian Climate Centre GCM. A brief description follows.

A necessary condition for the activation of convection is that the environment at a location is conditionally unstable. That is, an unsaturated parcel at the surface can be lifted to become unstable. The amount transported due to convection within a cloud must be distinguished from transport of the quantity outside the cloud, since the sum of both convergences yield a change in temperature for the grid box. The heating due to cumulus convection is then the total convergence for the grid box *minus* the convergence of the quantity in the large-scale environment. For heating,

$$CSC(S_{cs}) = -\frac{1}{\rho}\frac{\partial}{\partial z}\left(M_u S_u + M_d S_d - M_c S_{ls}\right) + L(C - E), \tag{2.29}$$

where M_c is the total mass flux (kg m^{-2} s^{-1}) which is the sum of the mass flux due to updrafts (M_u) and downdrafts (M_d); S_u, S_d, and S_{ls} are the quantities of dry static energy carried in updrafts, downdrafts, and in the large-scale environment; L is the latent energy of vaporization; and C and E are the large-scale condensation and evaporation rates. For moistening the grid box, a similar expression applies:

$$CSC(q_{cs}) = -\frac{1}{\rho}\frac{\partial}{\partial z}\left(M_u q_u + M_d q_d - M_c q_{ls}\right) - (C - E) \tag{2.30}$$

Note that discretization is not used in this scheme, so vertical coordinate z is used here for illustrative purposes. The convergence of (S or q) by an updraft or downdraft mass flux (M_u or M_d) is proportional to the difference between the entrainment (E) and detrainment (D) of (S, q) by the updraft or downdraft in the cloud plus or minus any condensational/evaporational contributions. For updrafts, we have

$$\frac{\partial}{\partial z}\left(M_u S_u\right) = \left(E_u - D_u\right) S + LC_u \tag{2.31}$$

and

$$\frac{\partial}{\partial z}\left(M_u q_u\right) = \left(E_u - D_u\right) q - C_u, \tag{2.32}$$

where C_u is condensation of water vapor within the updraft. The updraft is represented by an ensemble of plumes which all begin at the same level with the same initial mass flux. The top of the shallowest convective plume is known as the detrainment level, and can be no lower than the level of minimum saturated moist static energy ($h^* = c_p + Lq$). This level represents the bottom of the updraft detrainment layer. Each plume in the updraft ensemble has a characteristic rate of entrainment of environmental air Λ_D (m^{-1}), which depends on its level of detrainment z. Each plume thus carries a different mass depending on the amount of mass it brings in or entrains. Some plumes may be entraining a lot, while others may be entraining very little. The plume which detrains at the level of minimum h^* has entrainment rate Λ_0, which is the maximum entrainment rate of all plumes. All other plumes, which detrain above the level of minimum h^*, that is, within the updraft detrainment layer, entrain at a lower rate than Λ_0. See Figure 2.

The parameterization requires that each plume detrains with a temperature that is equivalent to the environmental temperature at its detrainment level z, which is ensured by requiring that $h(z) = h^*(z)$. Thus, with this condition and the set relationship between entrainment rate and plume detrainment level, an expression for the mass flux due to updrafts (an ensemble of plumes) can be written for any level z:

$$M_u(z) = \frac{M_b}{\Lambda_0} \int_0^{\Lambda_D(z)} \exp\left[\Lambda(z - z_b)\right] d\Lambda_D, \tag{2.33}$$

where the mass flux due to updrafts at some level z is the integral over all possible entrainments up to this level. Note that the integrand is an exponential function of height from cloud base z_b. The integral acts to amplify the amount of mass coming up at cloud base M_b, normalized by the maximum possible entrainment rate. The integral evaluates to

$$M_u(z) = \frac{M_b}{\Lambda_0(z - z_b)} \left(\exp\left(\Lambda_D(z)(z - z_b)\right) - 1\right). \tag{2.34}$$

The above equality is subject to the plume detrainment condition, expressed mathematically as

$$h_b - h^*(z) = \Lambda_D(z) \int_{z_b}^{z} \left[h_b - h(z')\right] \exp\left[\Lambda_D(z' - z)\right] dz', \tag{2.35}$$

which essentially states that the difference in a plume's moist static energy upon ascent from cloud base (z_b) and that which it has when detraining ($h^*(z)$) should equal what it

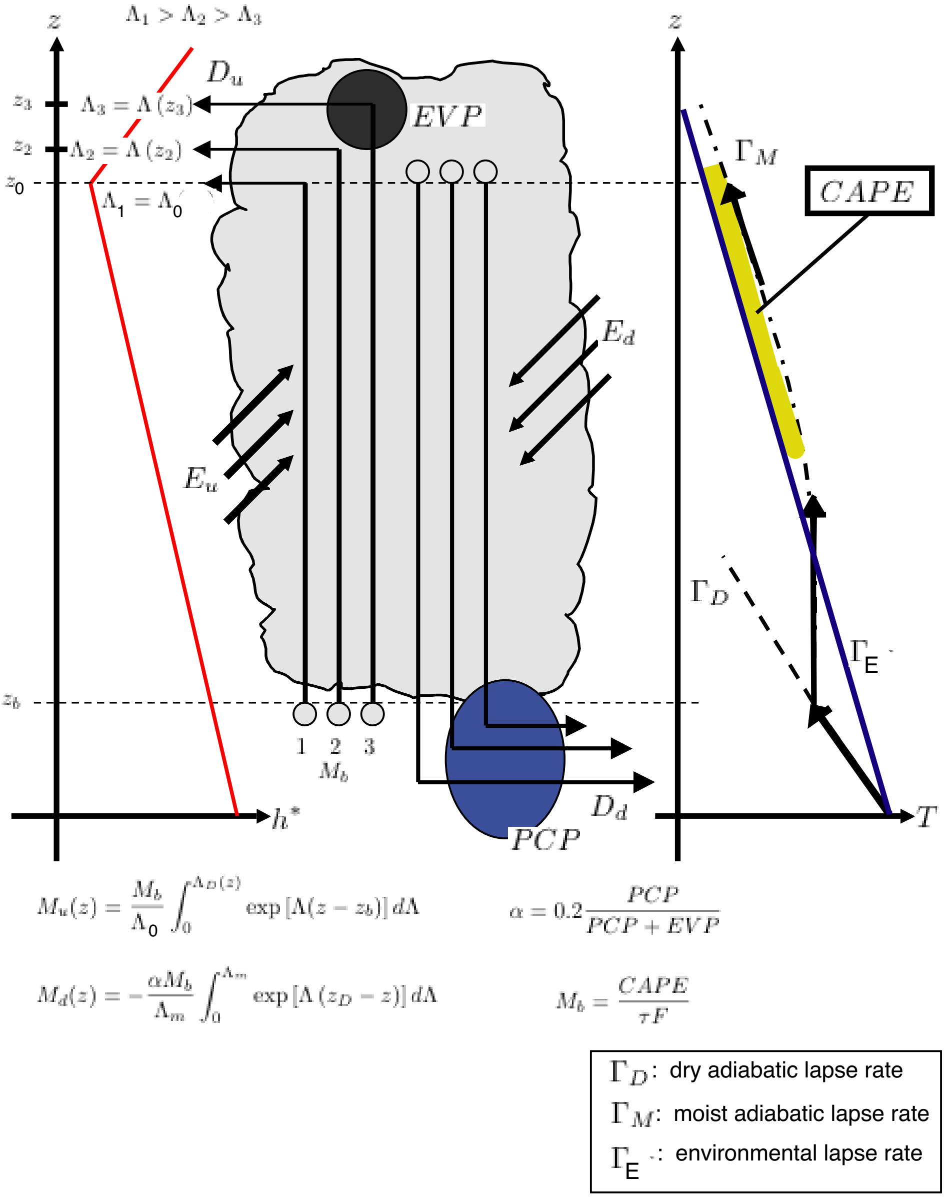

Fig. 2. Illustration of the (Zhang and McFarlane 1995) parameterization for deep convection in CCM3.

starts with (h_b) *minus* dilution due to all entrainment. Equation (2.35) allows numerical solution for the maximum entrainment rate Λ_D, given the atmospheric profile of h.

The detrainment layer is defined as the layer in which $\partial\Lambda_D/\partial z < 0$. Differentiating (2.34) with respect to z gives

$$\begin{aligned}\frac{\partial M_u}{\partial z} &= \frac{M_b}{\Lambda_0}\left(\frac{\partial \Lambda_D}{\partial z}\right)\exp\left(\Lambda_D(z-z_b)\right) + \frac{M_b\Lambda_D}{\Lambda_0(z-z_b)}\exp\left(\Lambda_D(z-z_b)\right) + \\ &\quad \frac{M_b}{\Lambda_0(z-z_b)^2}\left[\exp\left(\Lambda_D(z-z_b)\right)-1\right]. \end{aligned} \tag{2.36}$$

The only term on the right-hand side in (2.36) which can contribute to a decrease in M_u with altitude is the first term, which is only less than zero if $\partial\Lambda_D/\partial z < 0$. Therefore, the detrainment rate due to an updraft at any level can be expressed

$$D_u(z) = -\frac{M_b}{\Lambda_0}\left(\frac{\partial \Lambda_D}{\partial z}\right)\exp\left(\Lambda_D(z-z_b)\right),\ \frac{\partial \Lambda_D}{\partial z} < 0 \tag{2.37}$$

The entrainment rate due to an updraft at a level is represented by the sum of the remaining terms on the right-hand side of (2.36):

$$\begin{aligned}E_u(z) &= \frac{M_b\Lambda_D}{\Lambda_0(z-z_b)}\exp\left[\Lambda_D(z-z_b)\right] + \\ &\quad \frac{M_b}{\Lambda_0(z-z_b)^2}\left[\exp\left(\Lambda_D(z-z_b)\right)-1\right]. \end{aligned} \tag{2.38}$$

Expressions (2.37) and (2.38) can then be substituted into the convergence-by-updraft terms (2.31) and (2.32).

The same formulation applies for the convergence of (S, q) by downdrafts and is written

$$\frac{\partial}{\partial z}\left(M_d S_d\right) = \left(E_d - D_d\right)S + LC_d \tag{2.39}$$

and

$$\frac{\partial}{\partial z}\left(M_d q_d\right) = \left(E_d - D_d\right)q - C_d. \tag{2.40}$$

The downdraft is similar to an updraft in that it is represented by an ensemble of plumes. Each plume begins at the same level $z_D = z_0$, the level of minimum h^*, or the bottom of the updraft detrainment layer, and with the same mass flux, which is proportional to the cloud-base updraft mass flux, M_b. For all levels of downdraft plume detrainment, the maximum entrainment rate (Λ_m) is constant, unlike that for updraft plumes. Detrainment is confined to the subcloud layer ($z < z_b$). Intuition tells us that the downdraft mass flux $M_d(z)$ should increase with decreasing z, thus as the plumes entrain more mass. But what initially drives the downdraft ensemble of plumes downward is a constant multiple of what the updraft ensemble of plumes starts with, M_b. The constant (α) is itself proportional to the ratio of total rain water (PCP) to the sum of total rain water and the water vapor (EVP) that remains in the updraft upon arrival in the updraft detrainment layer:

$$\alpha = 0.2\frac{PCP}{PCP + EVP}. \tag{2.41}$$

Total rain water is determined as follows. Cloud liquid water (ρ_l) decays exponentially with height above the surface with a scale height (h_l) that is proportional to the vertically-integrated water vapor (Kiehl et al. 1996). Thus

$$\rho_l(z) = 0.00021 \exp\left(-z/h_l\right) \tag{2.42}$$

in kg m^{-3}. The amount of ρ_l at any level z which gets converted to rain water is given as

$$R_r(z) = c_0 M_u(z) \rho_l(z), \tag{2.43}$$

where $c_0 = 2 \times 10^{-3}$ m^{-1}. The available precipitate is then

$$PCP = \int_{z_b}^{z_T} R_r(z) dz, \tag{2.44}$$

in m s^{-1}, where z_T is the top of the convective layer. The water vapor that remains in the updraft once it reaches the detrainment layer is just the vertically-integrated convergence of water vapor due to the downdraft mass flux ($M_d(z)$) *minus* any water vapor that entrains into the downdraft during its cloud traversal:

$$EVP = \int_{z_b}^{z_D} \left(\frac{\partial}{\partial z} \left(M_d q_d \right) - E_d q \right) dz. \tag{2.45}$$

Based on the knowledge that the downdraft mass flux starts as αM_b and increases due to the plumes' entrainments (the maximum of which is Λ_m), an expression for the downdraft mass flux M_d at any level z can be written

$$M_d(z) = -\frac{\alpha M_b}{\Lambda_m} \int_0^{\Lambda_m} \exp\left[\Lambda \left(z_D - z\right)\right] d\Lambda, \tag{2.46}$$

which is similar in appearance to $M_u(z)$. When evaluated,

$$M_d(z) = -\frac{\alpha M_b}{\Lambda_m (z - z_b)} \left[\exp\left[\Lambda_m \left(z_D - z\right)\right] - 1\right], \tag{2.47}$$

which is then differentiated with respect to z to determine E_d and D_d as for E_u and D_u. Since detrainment of plumes only occurs for $z < z_b$, downdraft detrainment is given as

$$\begin{aligned} D_d(z) \quad = \quad & \frac{\alpha M_b}{\Lambda_m (z_D - z)} \left[\exp\left(\Lambda_m \left(z_D - z\right)\right) + 1\right] \\ & + \frac{\alpha M_b}{\Lambda_m} \left(z_D - z\right)^2 \left[\exp\left(\Lambda_m \left(z_D - z\right)\right]\right., \; z < z_b. \end{aligned} \tag{2.48}$$

Since entrainment by plumes only occurs for $z > z_b$, downdraft entrainment is given as

$$E_d(z) = \frac{\alpha M_b}{\Lambda_m \left(z_D - z\right)^2}, \; z > z_b. \tag{2.49}$$

Upon determination of M_b, expressions (2.48) and (2.49) can be substituted into the convergence-by-downdraft terms (2.39) and (2.40), which can then be substituted into (2.29) and (2.30) for the adjustment to stability.

Initiation of convection and its development take from the large-scale environment the potential energy which exists in the atmosphere due to the hydrodynamic instability (see

Figure 2). This potential energy, convective available potential energy (or CAPE, $\mathcal{C}$) (J kg^{-1}), is taken from the environment in the form of energy and water vapor, encapsulated in virtual potential temperature:

$$\Theta_V(z) = (1 + 0.61q)T\left(\frac{p(0)}{p(z)}\right)^{R/c_p} \tag{2.50}$$

The amount of CAPE used is the integral over the convective layer of the fractional amount of Θ_V consumed by plumes, which is expressed as the difference between Θ_V of undiluted rising plumes (or $\Theta_{V,p}$) and the large-scale (environmental) Θ_V:

$$\mathcal{C} = g\int_{conv} \frac{\Theta_{V,p} - \Theta_V}{\Theta_V} dz \tag{2.51}$$

in J kg^{-1}. The relationship between the rate of change of $\mathcal{C}$ and cloud-base mass flux (M_b) is linear:

$$\frac{\partial \mathcal{C}}{\partial t} = -M_b F, \tag{2.52}$$

where F must be the CAPE consumption rate (s^{-1}) by dimensional analysis, and is given as the time-derivative of the integrand in (2.51). If CAPE is consumed exponentially with time then

$$\mathcal{C} = \mathcal{C}_0 \exp\left(-\frac{t}{\tau}\right), \tag{2.53}$$

and necessarily,

$$M_b = \frac{\mathcal{C}}{\tau F}. \tag{2.54}$$

So the parameterization is closed. The value of τ represents the primary tunable parameter in the Zhang and McFarlane scheme. Physically, τ represents the time scale of CAPE consumption, or the time scale at which the hydrodynamic instability is eliminated. In this way, it is the time scale of the deep convection, and it determines the vigor with which deep convection is initiated and maintained (through (2.34) and (2.47)). Finally, through equations (2.43) and (2.44), it regulates the amount of precipitation in deep convection.

b. Shallow and mid-level convection

The scheme for shallow and mid-level convection was designed by (Hack 1994) and is the single convection scheme for the previous generation of this model. In CCM3, it serves to generate convection which is "not treated by the primary convective parameterization scheme" (Kiehl et al. 1996). Its goal is similar to that of the deep convection scheme: to quantify the convergence of energy and water vapor due to convection within a cloud. Instead of distinguishing between updrafts and downdrafts, this scheme lumps the transports together into one term, a convective mass flux M_c. The cloud-scale contributions to grid-scale heating and moistening are given as

$$CSC(S_{cs}) \approx -M_c(z)\left(S_{ls}(z) - S_{cs}(z) + L\rho_{ls}(z)\right) \tag{2.55}$$

and

$$CSC(q_{cs}) \approx -M_c(z)\left(q_{ls}(z) - q_{cs}(z) - \rho_{ls}(z)\right) \tag{2.56}$$

The parameterization is based on a three-level model atmosphere. (See Figure 3.)

Unlike the deep-convective scheme, discretization is important. The lowest layer $k+1$ is the sub-cloud layer in which non-entraining (saturated) convective parcels have their roots. The middle layer k is an in-cloud layer in which condensation and rain-out processes occur. And the highest layer $k-1$ is a partially-in-cloud layer in which there is active detrainment occurring. Layers $k+1$ and k are both moist-adiabatically unstable, which is to say that a non-entraining (saturated) parcel of air at level $k+1$ is unstable if lifted up to level k. Rainout in layer k is given as

$$LR_r^k = L(1-\beta)M_c\rho_{l,k}, \tag{2.57}$$

where R_k represents the cloud liquid water at level k that gets converted to rain, $\rho_{l,k}$ is the available cloud liquid water at k, and β is an undetermined detrainment parameter,

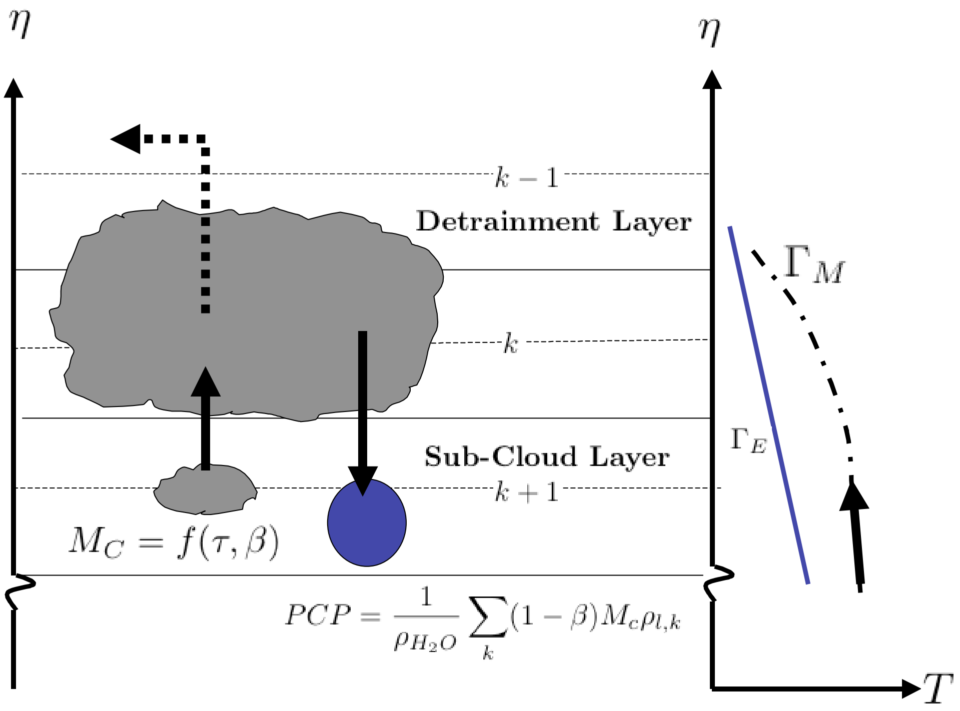

Fig. 3. Illustration of the (Hack 1994) parameterization for shallow and mid-level convection in CCM3.

constrained to lie between 0 and 1. Convective mass flux m_c is expressed as a complicated function of a convective adjustment time scale τ, and β.

The adjustment process begins with a guess of the value for detrainment parameter β. The guess is refined subject to the following requirements:

1. $M_c > 0$,
2. the resulting adjustment cannot result in the supersaturation of detrainment layer $k-1$, and
3. if moist static energy ($h = c_pT + Lq$) increases from inside the cloud to the detrainment layer, then the rate of increase with altitude cannot increase with time

Once β is chosen subject to these conditions, the convective mass flux M_c is then determined, and substituted into (2.55) and (2.56) for the adjustment in layers $k-1$ through $k+1$. Here again, as in the deep-convective parameterization, time scale τ is a tunable parameter, which represents the time scale of the convection. Since the convective mass flux M_c depends on τ, so does the amount of precipitation, through (2.57) since the precipitation rate is given by

$$PCP = \frac{1}{\rho_{H_2O}} \sum_k R_k \tag{2.58}$$

in m s^{-1}.

c. *Large-scale stable condensation*

Stable condensation occurs when the lapse rate is stable but the atmosphere at a level is supersaturated (i.e., $q_k > q_k^*$), where q_k^* is the saturation specific humidity. If this situation occurs, T_k and q_k are adjusted so that the supersaturated location is just saturated ($q_k = q_k^*$).

The new specific humidity is given by a first-order Taylor series approximation to be

$$q_k^{new} = q_k^* + \frac{dq_k^*}{dT}\left(T_k^{new} - T_k\right), \tag{2.59}$$

where the temperature change due to the release of latent energy upon condensation is given by the Clausius-Clapeyron equation:

$$T_k^{new} - T_k = \frac{L}{c_p}\left(q_k - q_k^{new}\right). \tag{2.60}$$

The rainout from the condensation at level k is given as

$$R_k = \frac{\left(q_k^{new} - q_k\right)\Delta p_k}{2g\Delta t} \tag{2.61}$$

in kg m^{-2} s^{-1}. Not all of this water actually reaches the ground since CCM3 allows for the systematic evaporation of some of the stratiform precipitation based on a parameterization from (Sundqvist 1998). In the global, annual average, the evaporation contributes to an approximate 20% reduction in the stratiform precipitation rate, which serves to moisten the middle and lower levels of the troposphere (Kiehl et al. 1996).

CHAPTER III

THE TROPICAL RAINFALL MEASURING MISSION (TRMM) SATELLITE

The most recent satellite used to measure rainfall is that of the Tropical Rainfall Measuring Mission, a joint venture between the National Aeronautics and Space Administration (NASA) and the National Space Development Agency (NASDA) of Japan[1]. One of the primary purposes of the satellite, as described in Simpson et al. (1988) over a decade before its launch, is to provide modelers with a measured distribution of the latent energy released in the atmosphere for the improvement of their models. The satellite itself orbits at an altitude of 401 km above the Earth's surface, boosted from a lower orbit of 350 km in 2001 for better fuel efficiency [2]. The satellite's orbit is circular and is oriented at a 35° inclination angle to allow for better coverage of the Tropics between 35°S and 35°N. It has a ground-track speed of 6.9 km s^{-1}. The antenna is shaped like a paraboloid oriented at an angle of 49° from nadir, which yields an incidence angle at the Earth's surface of 52.8°. Radiation is received through an aperture of length 61 cm and a focal length of 50.8 cm, while the antenna itself rotates around a nadir axis at a speed of 31.6 rotations per second, carving out a circle on the Earth's surface. Data are recorded from either the forward or backward 130° arc. The horizontal distance traversed in the arc is a swath width of 759 km (Kummerow et al. 2000; Huang 2001).

One of the primary intruments on board TRMM for measuring rainfall is the TRMM Microwave Imager (TMI), a 9-channel microwave radiometer. TMI measures the microwave energy emitted by the Earth-atmosphere system in channels between 10.65 and 85.5 GHz. The size of the instrument's field of view depends on the frequency, ranging

---

[1] NASDA was reborn as JAXA, the Japan Aerospace Exploration Agency, on October 1, 2003.

[2] The TRMM data used in this study comes from its pre-boost orbit.

from 63 km × 37 km at 10.65 GHz to 7 km × 5 km at 85.5 GHz (Kummerow et al. 1998). Microwave (frequencies between 1 and 300 GHz) sensors are ideal for rainfall measurement since hydrometeors are excellent absorbers (and emitters) of microwave energy [3] The first microwave sensor (or radiometer) used to measure global rainfall is the Electrically Scanning Microwave Radiometer (ESMR), which was launched on board the Nimbus 5 satellite in 1972. TMI measures the microwave energy in terms of a brightness temperature (T_B), which is defined in terms of radiance (L). The radiance of an object is the rate of transfer of energy per unit area per unit solid angle. Planck's Law describes the radiance of a perfect absorber or emitter (a blackbody[4]) as a function of frequency ν and temperature T:

$$L_\nu(T) = \frac{2\hbar\nu^5}{c^4}\frac{1}{\exp\left(\hbar\nu/kT\right) - 1}, \tag{3.1}$$

where $\hbar$ is Planck's constant in J s^{-1}, c is the speed of light in m s^{-1}, and k is Boltzmann's constant in J K^{-1}. For microwave frequencies, where $kT >> \hbar\nu$, the Rayleigh-Jeans approximation can be used:

$$L_\nu(T) \approx \frac{2k\nu^4}{c^4}T_B, \tag{3.2}$$

where T_B is brightness temperature, which is proportional to the radiance. Oceans emit relatively weakly in the microwave band of radiation. Therefore, to TMI, oceans appear cold. Hydrometeors (especially liquid precipitation) emit relatively strongly so that rain appears warm against a cold ocean surface. Over land, emissivity is a complicated function of vegetation, soil type, and time of year, among other variables. Thus over land, microwave measurements of rainfall are more ambiguous.

Wilheit et al. (1977) first explored the relationship between microwave brightness

---

[3] Liquid water drops are also good scatterers of microwave radiation, though algorithms which compute rainfall rates rely most on hydrometeor emission (Kummerow et al. 2000).

[4] A blackbody absorbs all incident radiation and emits the maximum possible radiation for all frequency bands and in all directions.

temperatures and rainfall rates over the ocean in an emission-based, plane-parallel microwave radiative transfer model. Wilheit et al. (1991) developed an algorithm to estimate monthly rain totals for 5° cells over water using brightness temperatures from the Defense Meteorological Satellite's SSM/I (Special Sensor Microwave Imager). It is based on a combination of the observed brightness temperatures from the 19.35 and 22.235 GHz channels. Measurements from TMI are translated to equivalent rainfall rates with a similar procedure (Kummerow et al. 2000), though some of the actual measuring channels are different from those used by the DMSP SSM/I.

Since microwave measurements of precipitation over land are less reliable than those over ocean, another instrument on board TRMM measures rainfall in a different way. The TRMM satellite is equipped with a precipitation radar which measures reflectivity of hydrometeors. The precipitation radar (PR), operating at a 13.8 GHz frequency, can measure the three-dimensional rainfall distribution. The energy backscattered by precipitation and received by the radar is converted to an equivalent precipitation rate, as explained in (Kummerow et al. 2000).

At present, the TRMM satellite remains in orbit, and fortunately, it observed most of the strong 1997-1998 El Niño event, allowing modelers to take advantage of this rich dataset for evaluating their simulations of ENSO. Our research uses the TRMM satellite data from both instruments, i.e., the merged dataset based on PR/TMI algorithm 2B31 (Kummerow et al. 2000), to evaluate the National Center for Atmospheric Research Community Climate Model Version 3 (CCM3) in the simulation of tropical precipitation.

CHAPTER IV

METHODS

A. TRMM Data

This study uses the TRMM 3G68 dataset, which was obtained from the TRMM Science Data and Information System (TSDIS). It consists of essentially instantaneous precipitation rates derived from TMI, from PR, and from the combination of both instruments averaged over $0.5^\circ \times 0.5^\circ$ latitude-longitude boxes between 38°S and 38°N. For validating CCM3, we use the precipitation rates from the combination of TMI and PR. Generally, the TRMM satellite is able to observe a given location in the Tropics about once per day, at a different time each day, with a cycle of 46 days, the period of its orbital precession (Negri and Bell 2002). Therefore, for the 44-month period considered here (January, 1998 - August, 2001), there are about 1320 observations of each of the aforementioned boxes. For each box, we estimate there to be about 28 samples of the diurnal cycle. Precipitation is highly variable in both space and time, and the incomplete nature of the satellite's sampling introduces an error in the retrieval relative to actual ground truth. This error is known as sampling error and has been the subject of several studies (see Shin and North (1988), Bell and Kundu (1996), Bell and Kundu (2000), Bell et al. (2001), Bell and Kundu (2003), and Bowman (2004) for example). According to Shin and North (1988), TRMM sampling errors in monthly-mean rain rates in wet areas of the Tropics would be less than 10% when averaging the observations on areas of $5^\circ \times 5^\circ$. And the results of Bowman et al. (2003) show that very-long-term averages of satellite-derived rain rates compare remarkably well with those measured by rain gauges on areas as small as $1^\circ \times 1^\circ$. According to Negri, et al. (Negri and Bell 2002) for estimation of the diurnal cycle from TRMM, sampling errors in hourly rain rates, averaged over 36 months and boxes of size $5^\circ \times 5^\circ$ range from 15% to 48% for the PR and 13% to 34% for the TMI. As the boxes we are using for comparison are much larger than $5^\circ \times 5^\circ$, and thus include more samples, we expect the sampling errors to be smaller.

B. GCM Simulations

One of the inputs for the model is a monthly-mean sea surface temperature boundary condition. For this study, we used sea surface temperatures provided to us by the Program for Climate Model Diagnosis and Intercomparison (PCMDI) at Lawrence Livermore National Laboratory (Taylor et al. 2000). Additionally, the model requires a time-variant ozone mixing ratio boundary dataset, and an initial conditions dataset that includes initial values of prognostic variables (Kiehl et al. 1996).

Climate models may exhibit considerable internal variability or noise, partly due to fluctuations on synoptic time scales. Consequently, as has been shown by Barnett (1995) in his GCM simulations, a single model simulation of an interannual climate event or a climate forecast is woefully inadequate for the accurate evaluation of a model's performance. We will show that this finding is also valid for CCM3. To distinguish the model's response to natural variations in the SST boundary condition (external variability) from its response to its own internal variability, it is helpful to look at statistics from an ensemble of simulations. Therefore, for this project, we carried out eight separate CCM3 simulations, each forced by exactly the same sea surface temperature boundary condition and differing only in their initial conditions. While the sensitivity of extended-range forecast models to initial conditions is quite significant (Lorenz 1963; Tracton and Kalnay 1993), the actual initial conditions are largely irrelevant to climate forecasts (Barnett 1995), since a climate simulation "forgets" its initial conditions after some limit of deterministic predictability. Therefore, to generate our ensemble, we modified initial conditions among the members by adding random perturbations to the temperature field of a 4-month spin-up run (September 1, 1996 - January 1, 1997). By the beginning of the TRMM observing period, in late November of 1997, the realizations have decorrelated from each other and can be treated as statistically independent. Inter-member correlations are never identically zero since the observed sea surface temperature field, common to all the members, exerts a common forcing. See Figure 4 for a diagram of how the ensemble of simulations was generated.

The precipitation rates of each simulation, both convective and large scale, are saved as hourly averages. Because the simulations were conducted with 20-minute time steps, each hourly average is the average of 3 time steps. The annual and diurnal cycles of precipitation are compared between model and satellite. For the annual cycle analysis, CCM3 monthly, seasonal, or annual means shown are *ensemble* monthly, seasonal, or annual means, and all TRMM results are either monthly, seasonal, or annual means averaged onto the CCM3 grid. For the diurnal cycle analysis, CCM3 climatological hourly means shown are *ensemble* climatological hourly means, and and all TRMM results are climatological hourly means averaged onto the CCM3 grid. Since the sampling errors associated with TRMM are too large on the model's grid, both datasets will be spatially averaged over much larger regions (greater than $5^\circ \times 5^\circ$) for the model validation.

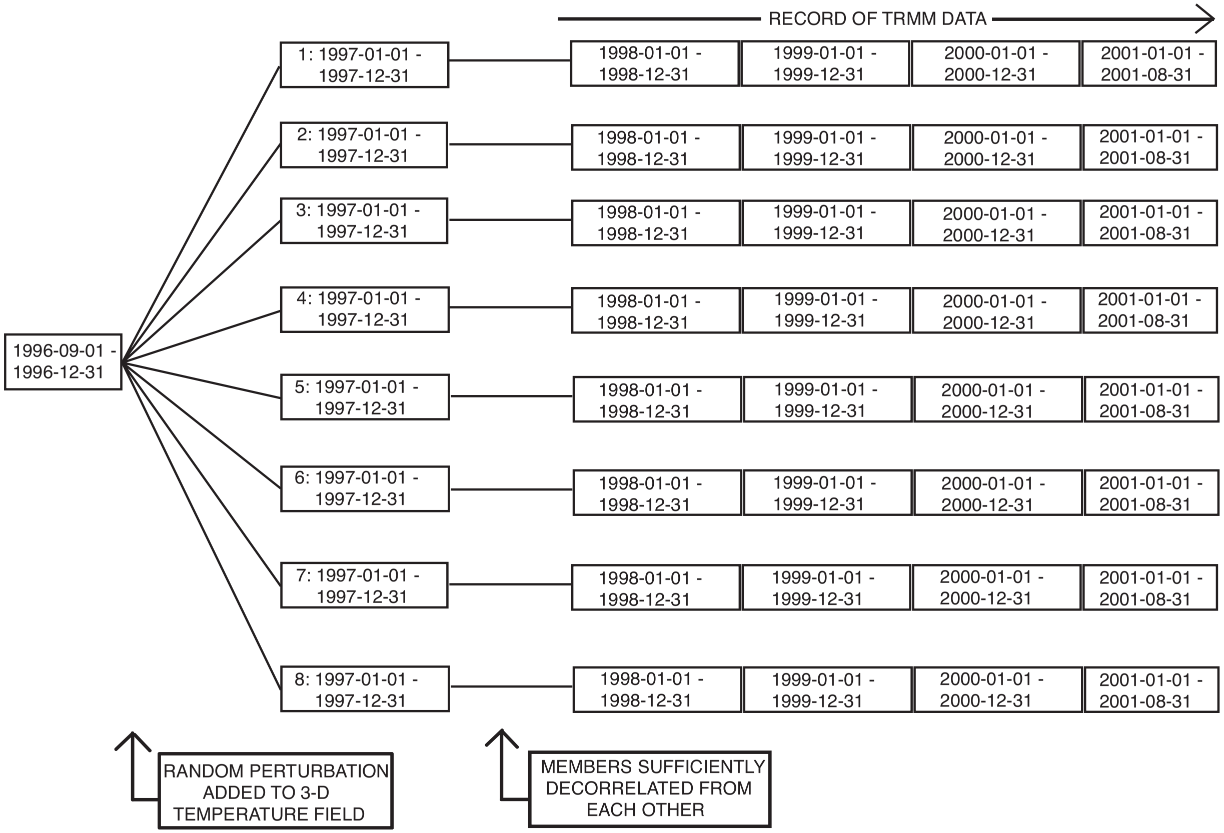

Fig. 4. Diagram showing how the CCM3 simulation ensemble was generated. Note that the record of TRMM data, which begins in November, 1997, continues as of this writing.

CHAPTER V

RESULTS

A. Comparison of Annual Cycles

*Before discussing the comparison of annual cycles, we briefly address the variability across the ensemble. For the purposes of analyzing the model's internal variability and for the comparison that follows, we divided the Tropics into 48 separate, non-overlapping regions with partitions resting halfway between two adjacent grid points. See Figure 5(a) which is a map of their locations. Boxes are numbered down the columns and then across the rows, each box labeled with a suffix of 'W' or 'E' depending on whether it is west or east of the Prime Meridian. Time series are computed from the monthly means averaged over all grid points within a box. For example, the results to be shown for box 1W are monthly means averaged over all grid points between longitudes 178.6°E and 136.4°W, and between latitudes 19.5°N and 30.7°N. Longitudes and latitudes are rounded off to the first decimal place for brevity. Figures 5(b) shows area-averaged monthly-mean precipitation rates for all eight ensemble members for box 14W. The ensemble mean is shown in heavy black. Figure 5(c) shows the results for box 15E.

For box 14W, the model exhibits remarkably little variability across the ensemble. Each of the 8 curves falls very close to the ensemble mean. This is not the case for box 15E. Here, the model exhibits considerably more spread among the simulations. Notice that a clearly-defined seasonal oscillation is evident, which is the model's response to SST variations.

---

*Parts of Chapter V are reprinted from "The Diurnal Cycle of Tropical Precipitation in a General Circulation Model" by J. Craig Collier and Kenneth P. Bowman, 2004, *Journal of Geophysical Research - Atmospheres*, in press, with permission from Dr. Alan Robock, editor of *JGR - Atmospheres*.

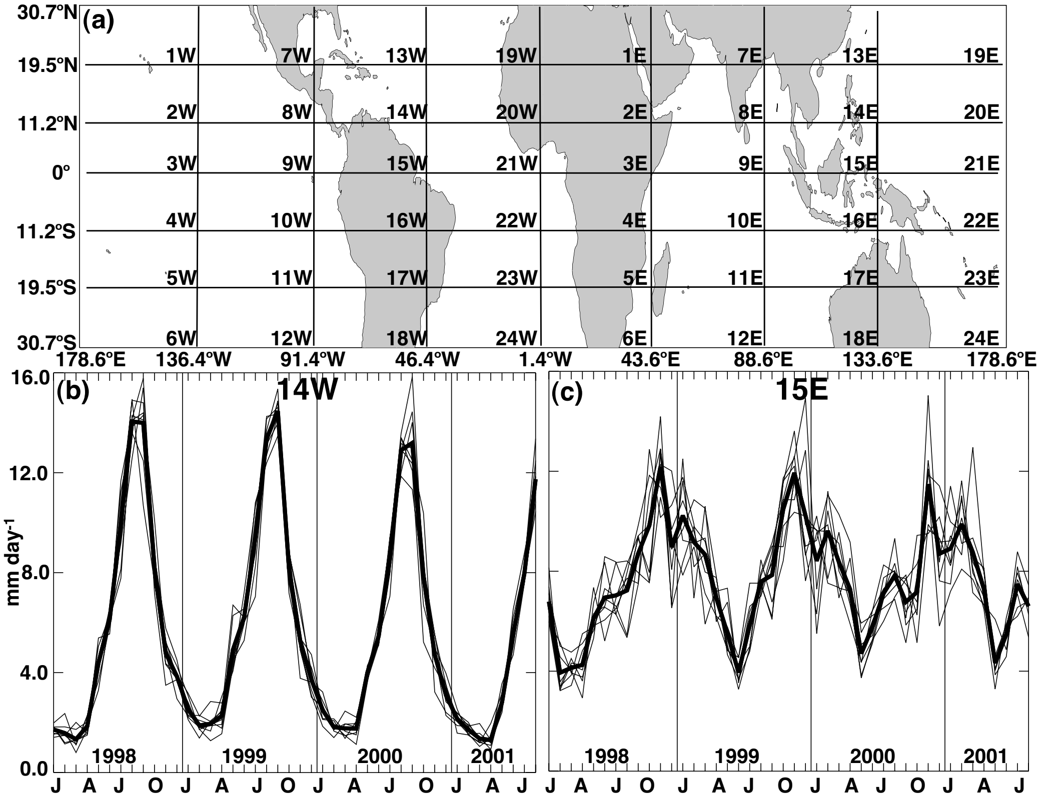

Fig. 5. Map of the 48 regions of comparison (a) and monthly-mean precipitation rates in mm day^{-1} for January, 1998 - August, 2001 as simulated by the 8 members of the CCM3 ensemble for 14W (b) and 15E (c). Gray curves represent the individual member means, and the heavy black curve represents the ensemble mean.

The comparison of the simulated and observed precipitation rates is now discussed. Figure 6 shows a map of the climatological annual-mean precipitation rate in the Tropics, as computed from the CCM3 simulations and from the TRMM observations for the period 1 January 1998 - 31 August 2001. These results are presented on the model's approximate $2.8° \times 2.8°$ grid.

Features of the large-scale general circulation are evident in the annual-mean precipitation intensity. The model clearly depicts the ITCZ regions straddling the Equator and thereas of subsidence in the subtropics. It also captures the ascent and descent regions of the Walker Circulation in the Pacific Ocean. Along the Equator, more intense precipitation occurs over the Indian Ocean and the Maritime Continent, while less precipitation occurs in the eastern Pacific. The geographical distributions of mean precipitation agree fairly well with the TRMM climatology, but there are regions of overestimation by the model (see Figure 6(c), which plots the absolute differences). These include the Caribbean and eastern Pacific, equatorial Africa, and the Indian Ocean. There are also regions where the model underestimates precipitation. These are generally smaller in area and include parts of northwestern and southeastern South America, the central equatorial Atlantic, western equatorial Africa, extreme southeastern Asia, and parts of the Maritime Continent.

Maps of the climatological seasonal means (Figure 7) show the tendency for CCM3 to simulate larger time-mean precipitation rates than observed by TRMM. At this point, it should be noted that the TRMM seasonal means are the time averages of 12 months of TRMM data (four 3-month seasons). CCM3 results, on the other hand, are computed using 8 times as much data. In addition, the CCM3 rain fields are available much more frequently than the TRMM observations. Therefore, when averaging over these shorter time periods, the CCM3 maps are generally smoother than the corresponding TRMM maps; this is particularly evident in maps of monthly means (not shown). Despite the substantially greater amount of averaging, the CCM3 data have numerous localized regions with higher precip-

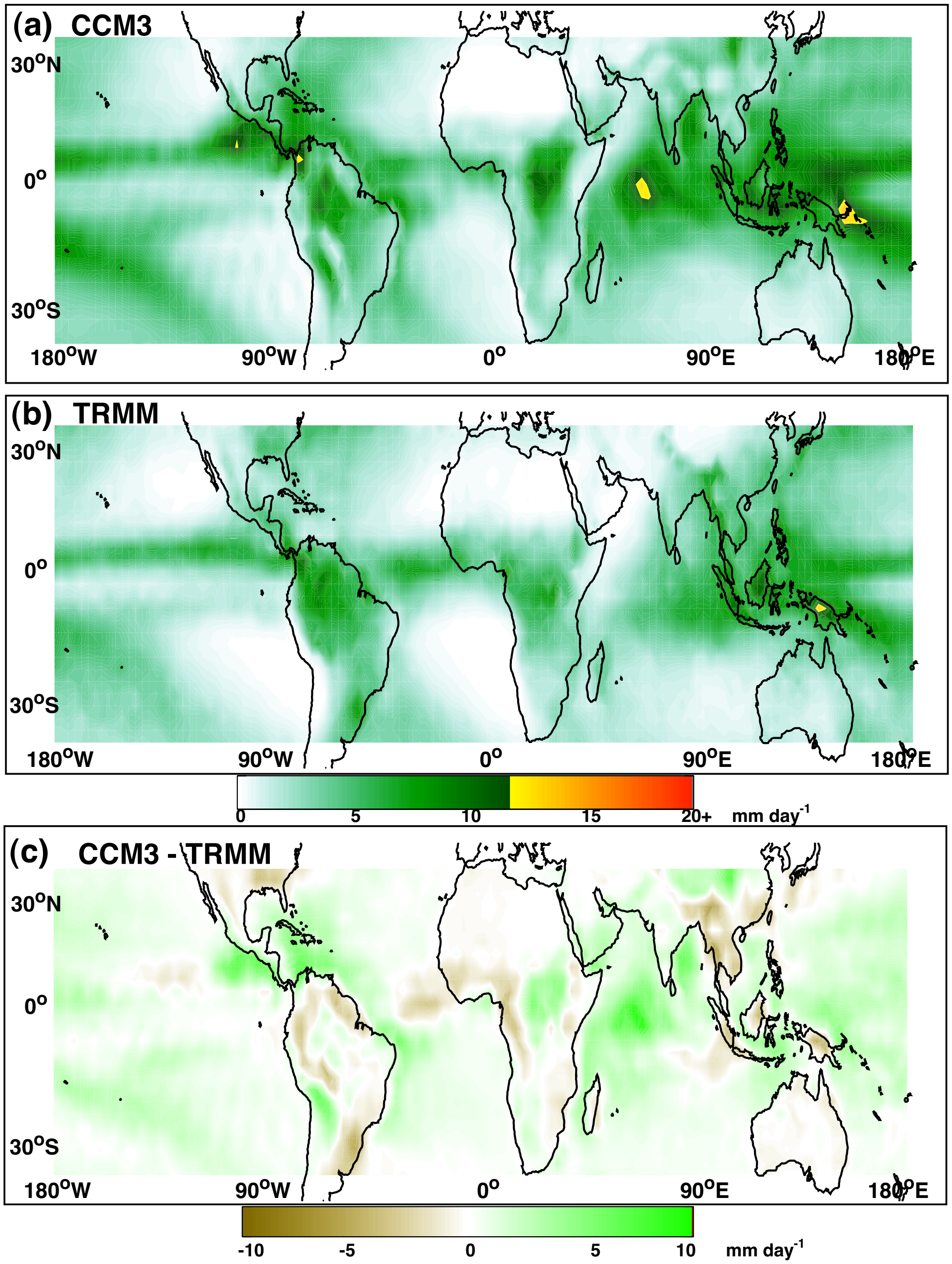

Fig. 6. Climatological annual-mean precipitation rate in mm day^{-1} as simulated by CCM3 (a) and as observed by TRMM (TMI+PR) (b) for the period 1 January 1998 - 31 August 2001. The climatological mean difference (CCM3-TRMM) is plotted in (c).

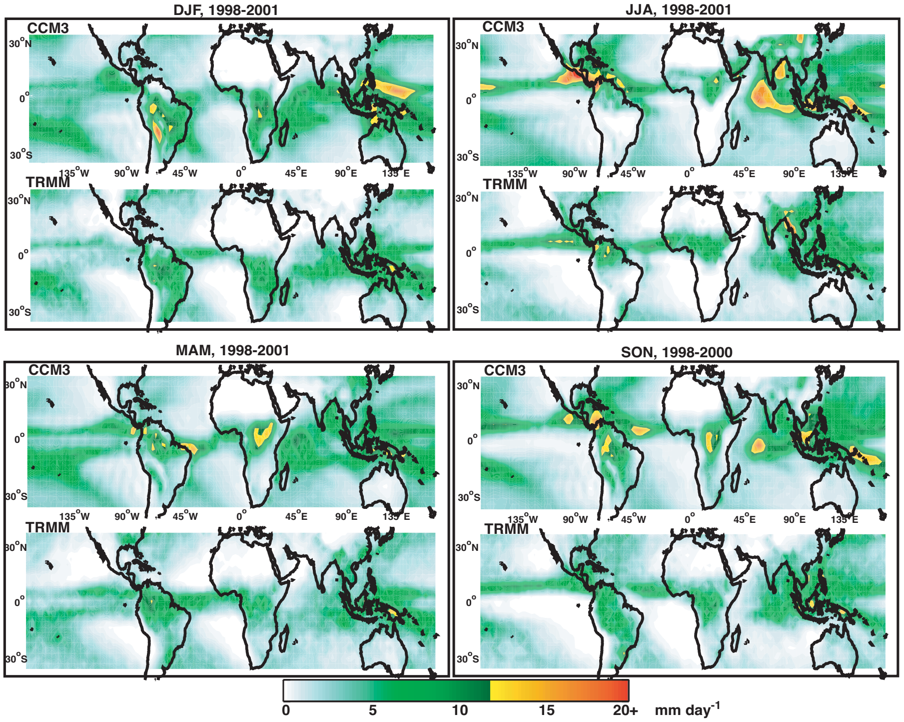

Fig. 7. Precipitation rates (mm day^{-1}) simulated by CCM3 (top) and those estimated by TRMM (TMI+PR) data (bottom) averaged over the four meteorological seasons, from 1998 - 2001.

itation rates than seen by TRMM. For example, during DJF, simulated precipitation rates are quite high over portions of eastern South America and the western equatorial Pacific Ocean, compared to the TRMM observations. During MAM, large localized differences are evident in equatorial Africa and in the western equatorial Atlantic. In JJA, the largest differences are concentrated in two regions: Central America (and the adjacent waters) and in the northern Indian Ocean. The differences in these regions are large not only in magnitude but also in spatial scale. In SON, model - satellite differences are more localized. Relative to TRMM observations, CCM3 simulates too much precipitation in portions of the Caribbean, the central Equatorial Atlantic, equatorial Africa, the central Indian Ocean, and the western equatorial Pacific.

To provide a more detailed view of the time structure of the differences between the model and the data, we compare the fields month by month in each of the 48 boxes described earlier. These may be seen in Figure 8. Note that the 48 boxes range in size from $45^\circ \times 8.3^\circ$ to $45^\circ \times 11.2^\circ$ and thus are large enough to compare monthly means without worrying about the sampling errors associated with the TRMM observations. However, it is important to observe two points regarding these time series. First, the monthly means associated with these boxes are averages over at least 48 $2.8^\circ \times 2.8^\circ$ model grid boxes, while the above maps of the annual and seasonal means are produced on the model's approximate $2.8^\circ \times 2.8^\circ$ grid. Therefore, some of the details evident on the model's grid can be blurred or hidden in the averages over these larger boxes. Second, due to its orbital precession, TRMM requires at least 1.5 months to completely sample the diurnal cycle of rainfall over a given grid box. Therefore, in a given month, boxes with a strong diurnal cycle may experience most of their rain in hours unobserved by the satellite, biasing low the satellite monthly mean. It has been noted by (Lin et al. 2002) that this phenomenon may introduce a spurious signal into a monthly time series, the size of which is difficult to estimate.

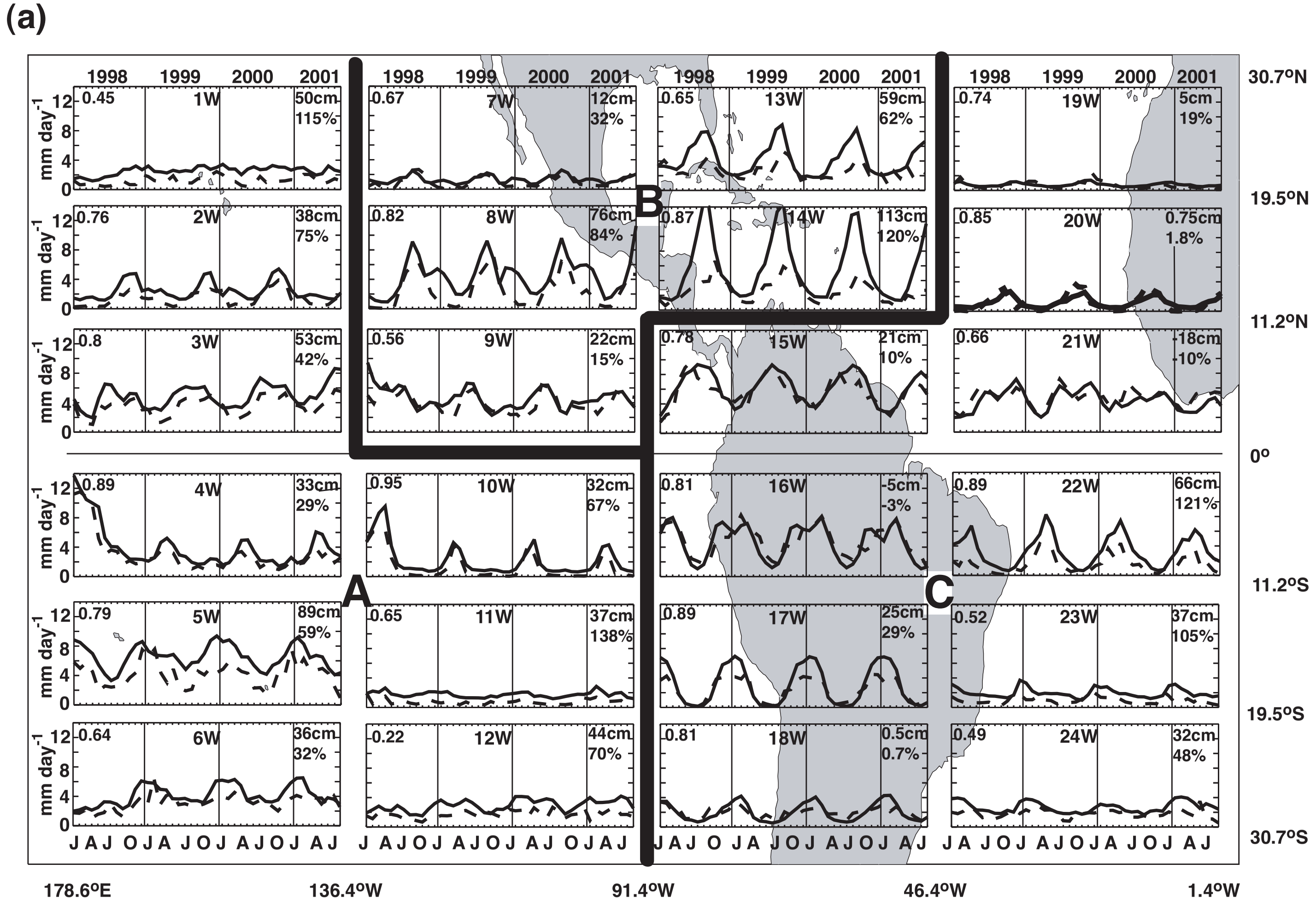

Fig. 8. Time series of CCM3 and TRMM monthly-mean precipitation rates in mm day^{-1} as from January, 1998 through August, 2001 for 48 separate regions in the Tropics. CCM3 ensemble-average mean: solid, TRMM mean: dash.

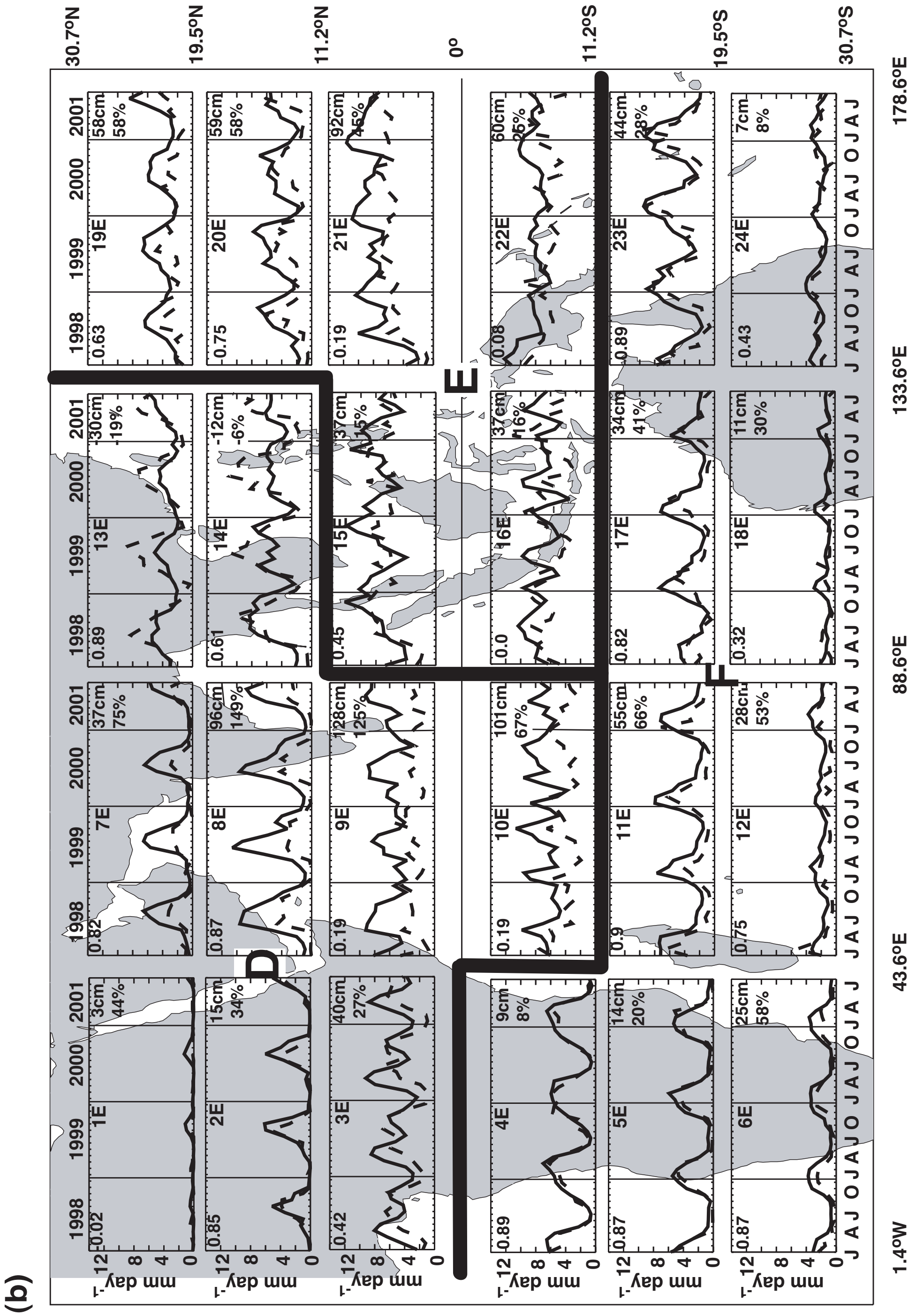
(b)
30.7ºN
19.5ºN
11.2ºN
0º
11.2ºS
19.5ºS
30.7ºS
1.4ºW
43.6ºE
88.6ºE
133.6ºE
178.6ºE
1998
1999
2000
2001
mm day-1
12
8
4
0
J A J O J A J O J A J O J A J
D
E
F
1E 0.02 3cm 44%
2E 0.85 15cm 34%
3E 0.42 40cm 27%
4E 0.89 9cm 8%
5E 0.87 14cm 20%
6E 0.87 25cm 58%
7E 0.82 37cm 75%
8E 0.87 96cm 149%
9E 0.19 128cm 125%
10E 0.19 101cm 67%
11E 0.9 55cm 66%
12E 0.75 28cm 53%
13E 0.89 -30cm -19%
14E 0.61 -12cm -6%
15E 0.45 37cm 15%
16E 0.0 37cm 16%
17E 0.82 34cm 41%
18E 0.32 11cm 30%
19E 0.63 58cm 58%
20E 0.75 59cm 58%
21E 0.19 92cm 45%
22E 0.08 60cm 25%
23E 0.89 44cm 28%
24E 0.43 7cm 8%

Time series of monthly-mean precipitation rates are shown in Figure 8. In order to quantitatively measure how well one series tracks the other, the Spearman rank correlation coefficient is computed for each box. It is a nonparametric statistic that assumes no a priori knowledge of the distributions of the monthly means (Deshpande et al. 1995), and its value may span the real numbers from -1 to 1. In Figure 8, the coefficient is printed in the top left-hand corner of each region's plot. A deficiency of the difference map of Figure 6(c) is that it is not useful for discerning the model's underestimations or overestimations *relative* to what TRMM observes. While the absolute differences are more important for evaluating the model's simulation of latent heating, the relative differences are important for appraising the model's success with precipitation; relative differences can be large in regions where TRMM observes little to no rainfall. Therefore, the absolute and relative differences in total precipitation as simulated by the model and as observed by the satellite are computed for each of the 48 regions. Total precipitation refers to the sum over all 44 months of the monthly-mean precipitation rates weighted by the number of days in each month. The absolute difference in total precipitation refers to CCM3 total precipitation - TRMM total precipitation, where the sign of the difference is retained. That is, an absolute difference that is less than zero indicates that when rainfall is totaled over the comparison period, the model exhibits a dry bias. The relative difference is the ratio of this absolute difference to the TRMM total precipitation multiplied by 100. In Figure 8, the absolute and relative differences are printed in the top right-hand corner of each region's plot, the absolute differences expressed in centimeters per year, and the relative differences in %. We divided the Tropics into 6 geographical regions, labeled ‘A’ through ‘F’ and discuss each region in turn. Where absolute and relative differences in total precipitation are quite large, the region is further subdivided into smaller boxes for closer inspection. However, even these smaller boxes are large enough that we expect TRMM sampling errors to be sufficiently small. Within these subregions, large model - satellite differences are diagnosed as either wet-season, dry-season, or seasonally-invariant, based on relative differences between the monthly means.

a. Region A: the central and eastern Pacific

Over the central and eastern Pacific, CCM3 performs reasonably well in its simulation of precipitation. For example, the model simulates well the annual cycle of precipitation, where it is discernible in the observations. The simulations of boxes 3W, 4W, and 10W are good examples. The simulation of box 4W in the central Pacific is particularly noteworthy in that CCM3 tracks TRMM closely during the relatively wet El Niño period of 1998 and then continues to simulate the normal annual cycle thereafter. In boxes where the model's phase of the monthly precipitation is simulated well, the correlation coefficient is high, as would be expected. Even where the annual cycle is somewhat less pronounced, the model results remain close to the observations, such as in box 6W. However, where the model correctly captures the phase of the annual cycle, its precipitation rates do not always agree so well with the observations in magnitude. Absolute and relative differences are particularly high in boxes 5W, 11W, and 12W. For a better understanding of where and when the largest of the differences occur, these regions are further subdivided, as seen in Figure 9.

Over this region of the southern Tropical Pacific, differences in the monthly means are generally independent of season and are highest in boxes 1 and 2, where, compared to the satellite observations, the model simulates at least 85 cm more precipitation per year during the comparison period. Figure 7 suggests that the large model - satellite differences here are caused by the model's generating a South Pacific Convergence Zone (SPCZ) which is both too large and too intense. The absolute differences in total precipitation taper toward the South American coast, as do the monthly-mean precipitation rates in general. However,

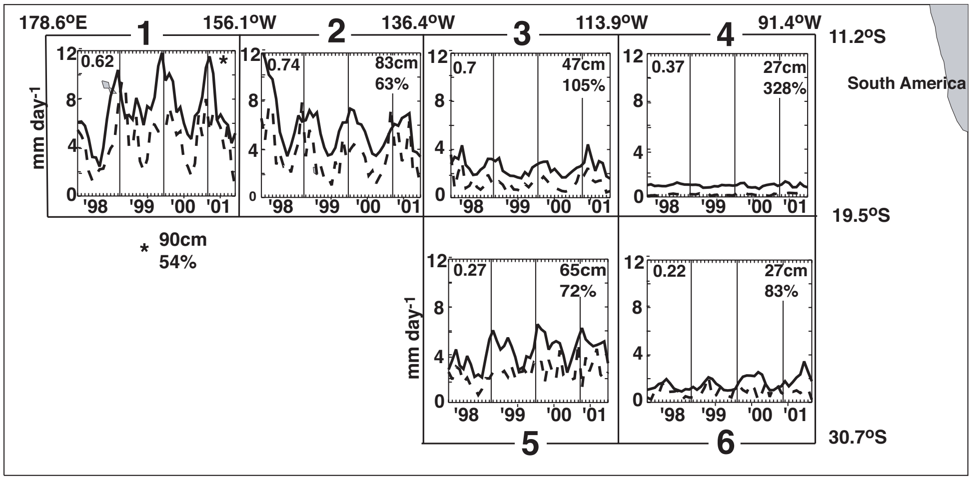

Fig. 9. CCM3 (solid) and TRMM (dashed) monthly-mean precipitation rates in mm day^{-1} for the southern Tropical Pacific Ocean (boxes 5W, 11W, and 12W of Figure 8(a)).

relative differences are larger over this part of the region. For example, the model simulates nearly 450% too much precipitation in box 4 and in excess of 100% too much precipitation in box 3. In spite of its difficulties with simulating magnitude in these dry areas, the model is reasonably successful with capturing the annual cycle. The success is most evident in boxes 1 and 2 where it correctly simulates maxima in DJF and minima in JJA. However, the model's maxima and minima are large relative to the observations.

b. Region B: Central America, the Caribbean, the Gulf of Mexico, and the far eastern Pacific

In contrast to region A, where the model - satellite differences are relatively small except in the southern-most boxes, differences are quite large in most of region B, encompassing Central America, the Caribbean, the Gulf of Mexico, and the far eastern Pacific. While

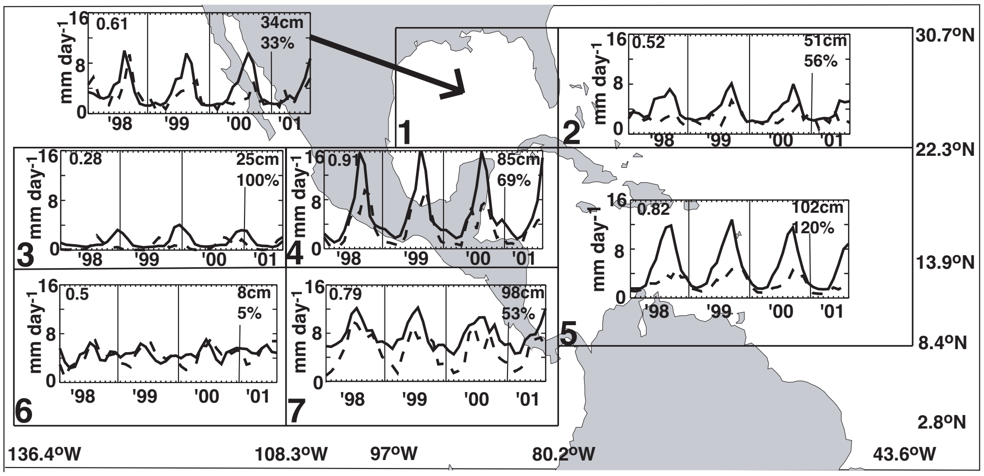

Fig. 10. Same as in Figure 9 except for the Central American-Caribbean-far eastern Pacific region (boxes 7W, 8W, 9W, 13W, and 14W of Figure 8(a)).

the simulation in box 7W is satisfactory, the model exhibits problems with magnitude elsewhere. In box 8W, the model simulates two precipitation peaks per year, which is not seen by the satellite. Overestimation by the model appears both in JJA and in DJF. In boxes 13W and 14W, it is largely confined to JJA. Differences in the monthly means are considerable in box 14W, where simulated precipitation rates are some 3 times higher than observed by TRMM during this period, resulting in excessive rates of near 14 mm day^{-1}. In box 9W, where absolute and relative differences in total precipitation are small, the model appears to be having trouble capturing the annual cycle. This region is further subdivided for a more precise evaluation in Figure 10.

Over this region, model - satellite differences are much more seasonally-dependent than they are over the southern tropical Pacific. In box 5, the model produces three times as much precipitation in the wet season despite fair agreement with the satellite observations during the dry season. In box 4, the model's overestimation is as large as 100% in both the wet and dry seasons despite fair agreement during the transitional periods of the year. In box 7, the simulation is relatively satisfactory during the wet season, but significantly wet-biased during the dry season, estimating between 2 and 6 times the satellite-measured precipitation during this time. Box 3 is drier than the other boxes examined here. However, in this box, the relative difference in total precipitation is large. Relative to the observations, the annual maximum is simulated late in the year and is about twice as high. In contrast to boxes 3, 4, 5 and 7, where absolute and/or relative differences in total precipitation are significant, these differences are almost negligible in box 6. Here, the simulation disagrees with the observations in the phase of the annual cycle. Annual maxima are placed reasonably correctly, but annual minima are consistently about 1/3 of a year (4 months) behind their location in the data. The model is comparatively successful with both magnitude and phase in boxes 1 and 2, except for a model wet bias of around 100% in the August-September timeframe. In terms of the total precipitation over the comparison period, the absolute and relative differences in these two boxes are quite a bit lower than those of boxes 4 and 5 to the south.

c. Region C: South America and the Tropical Atlantic

Compared to the rest of the tropical Western Hemisphere, the simulation over the continent of South America (boxes 15W - 18W) is superior. In general, the CCM3 annual cycle and magnitudes of precipitation are in good agreement with TRMM. Over the northern tropical Atlantic (boxes 19W, 20W, and 21W), agreement is also quite good. Boxes 19W and 20W are dry compared to the rest of region C, and the model's low monthly-mean precipitation rates closely follow those observed. Box 21W is considerably wetter throughout the year, but the CCM3 monthly means are still quite close to those observed, and the annual cycle

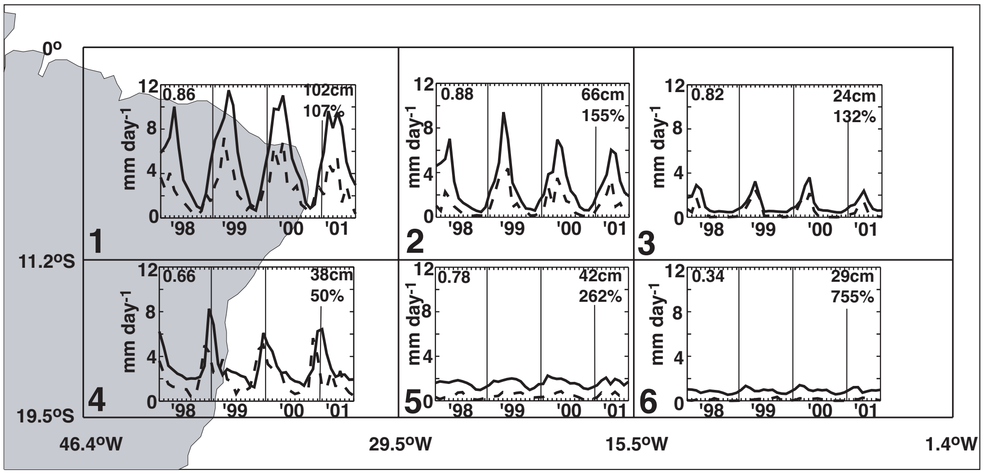

Fig. 11. Same as in Figure 9 except for the southern tropical Atlantic region (boxes 22W and 23W of Figure 8(a)).

evident here is similarly well-simulated. As a whole, region C shares a similarity with central and eastern Pacific region A: the simulation and observations are in good agreement except in the southern oceanic boxes, where simulated magnitudes are too large. The most problematic portion of the region resides in southeastern boxes 22W and 23W, where the model tends to be consistently too wet throughout the period. Absolute and relative differences in total precipitation are quite large in these two boxes. See Figure 11, in which this area is further partitioned.

Like those of the southern tropical Pacific, the model-satellite differences in the subregions of the southern tropical Atlantic are largely independent of season. Also like those of the southern tropical Pacific, the differences are exclusively ones of magnitude. Where an annual cycle is evident, such as in boxes 1, 2, and 4, CCM3 simulates it well. In this region, the largest absolute difference in total precipitation is in box 1, encompassing extreme eastern South America and the adjacent ocean. Here, the model's monthly means are nearly consistently between 100 and 150% larger than the satellite's monthly means throughout the year, excepting reasonable agreement in November. The same behavior can be seen in box 4, yet, as in box 1, there are single months where the model output and satellite data agree. Relative differences are huge in arid boxes 5 and 6, where there is no annual cycle present. For example, in box 5, over the comparison period, the model simulates 265% too much rain, and in box 6, it simulates over 700% too much, the largest relative difference in total precipitation found in the Tropics of the Western Hemisphere.

d. Region D: Northern Africa and Southern Asia

In northern Africa and southern Asia, the comparison does not fare well. In box 3E, the model output and satellite data is not well-correlated. CCM3 simulates a semiannual maximum in precipitation which appears unfounded in the TRMM data. Though the model's second precipitation peak (in October) lies relatively close to the observations, the first one greatly exaggerates precipitation in January through April, and the relative minimum between the two peaks actually underestimates precipitation from May to October. A partitioning of this region into smaller boxes, as seen in Figure 12, shows that the model's behavior with respect to the satellite observations varies considerably on smaller spatial scales.

In equatorial Africa, model - satellite differences are highly spatially-dependent. In box 1, while the model agrees well with the satellite during the dry season, it is too dry during the wet season. In box 4, the model is too dry during the wet season and too wet during the dry season, indicating that the monthly means are out of phase. CCM3 overestimates total precipitation in boxes 2, 3, 5, and 6. In box 2, the model's monthly means are in good agreement with those of TRMM during the dry months of DJF, but when there is

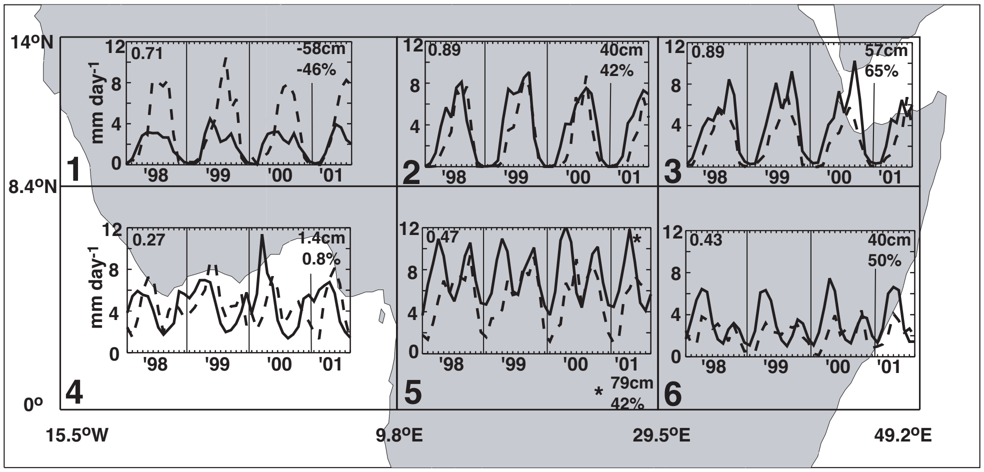

Fig. 12. Same as in Figure 9 except for the equatorial Africa region (boxes 2E (southern half) and 3E of Figure 8(b).)

observed precipitation, they are consistently higher. Exceptions occur during SON of 1998 and 1999. In box 3, the model - satellite differences are seasonally-invariant: the model's wet bias is present throughout the year, even in the rainless months of DJF. The model - satellite difference in total precipitation is largest in box 5, where the contrast between the monthly means is dramatic. Here, CCM3 most prominently simulates the semiannual cycle evident in the larger-scale average, but this feature is not well supported by the TRMM data. The model's maxima are consistently higher than those of the observations, and its minima in DJF are far too high.

Returning to Figure 8(b), in south-central Asia and the northern Indian Ocean, the disparity between CCM3 and TRMM is also quite large. In this region, absolute differences in total precipitation are especially large in boxes 8E, 9E, and 10E, and with few exceptions throughout the 44-month period, the model consistently overestimates precipitation in these

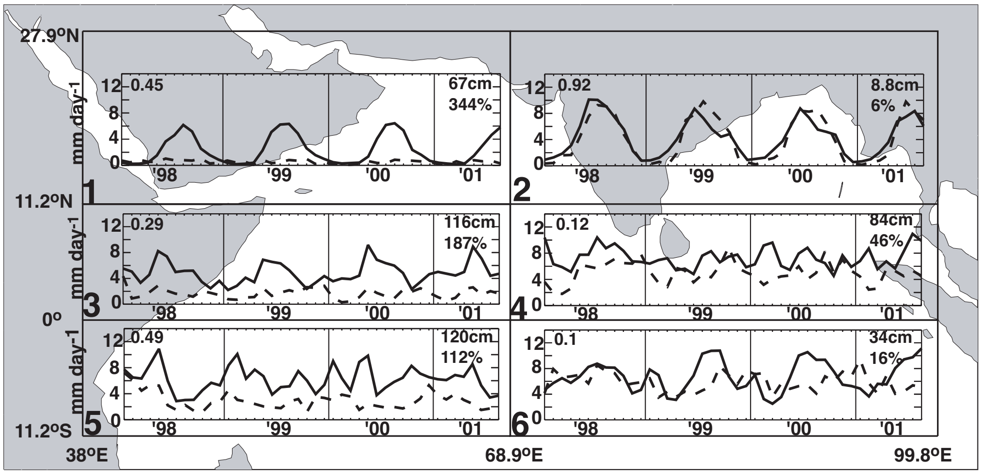

Fig. 13. Same as in Figure 9 except for the south-central Asia - northern Indian Ocean region (boxes 7E - 10E and western portions of boxes 13E and 14E of Figure 8(b).)

boxes. This region is subdivided in Figure 13 for a more detailed consideration.

One of the outstanding features of Figure 13 is the model's excessive precipitation rates in box 1 (the southern Arabian peninsula) during JJA. Here, the model's overestimation is on the order of 300%. According to TRMM observations, monthly-mean precipitation rates are less than 1 mm day^{-1} every month of the year, in stark contrast to the model's simulation of an average 6 mm day^{-1} during the month of August. This model - satellite difference can hardly be classified as a wet-season model wet bias, since there is no seasonal variation evident in the TRMM observations. It appears that the model is creating a wet season that does not exist. According to the seasonal-means map (Figure 7) the source of the artificial wet season in JJA appears to be an extension of a rainfall belt stretching across equatorial Africa, from Guinea on the Atlantic coast, through the Congo, and then northeastward into Saudi Arabia. However, in contrast to CCM3, TRMM data suggest that this belt does not extend as far east and that there is a clearly-defined “dry” spot over Saudi Arabia, consistent with its small monthly means.

The precipitation of box 2 is simulated much more satisfactorily. This box is dominated by a monsoon-type climate, wherein strong southwesterlies during the summer months transport moisture from the Indian Ocean into the Indian subcontinent (Pant and Kumar 1997), (Kendrew 1961). Here, the model’s timing of the onset of the monsoon is about right, according to the TRMM observations. In this box, the model’s total wet bias is less than 10 cm year^{-1}. In boxes 3-6, where there is little annual cycle evident, the comparison fares better in boxes 4 and 6 than in boxes 3 and 5. Precipitation in box 6 is simulated remarkably well during all of 1998. By contrast, in boxes 3 and 5, the absolute difference in total precipitation is quite large (over a meter per year), yet it is difficult to discern any systematic pattern to the model’s wet bias.

e. Region E: the Maritime Continent and the Western Tropical Pacific

There appears to be little seasonal variation in the precipitation over the Maritime Continent, both in the observations and in the simulations. In boxes 15E and 16E, monthly means are high throughout the year (greater than 6 mm day^{-1}). There are intermittent periods of model overestimation and underestimation, but the total precipitation received over a course of a year is in good agreement with the observations, relative to the rest of region E. Over the western tropical Pacific, CCM3 does not behave as well. Consider the partitioning of boxes 19E and 20E in Figure 14 for example.

While the model performs comparatively well in box 1, its wet bias in boxes 2-6 lies between 50 and 80 cm year^{-1}. CCM3 appears to be simulating a strong seasonality to the precipitation in boxes 2 and 3, though such a seasonal variation is not apparent in the observations. Thus, it is difficult to classify the model - satellite differences here,

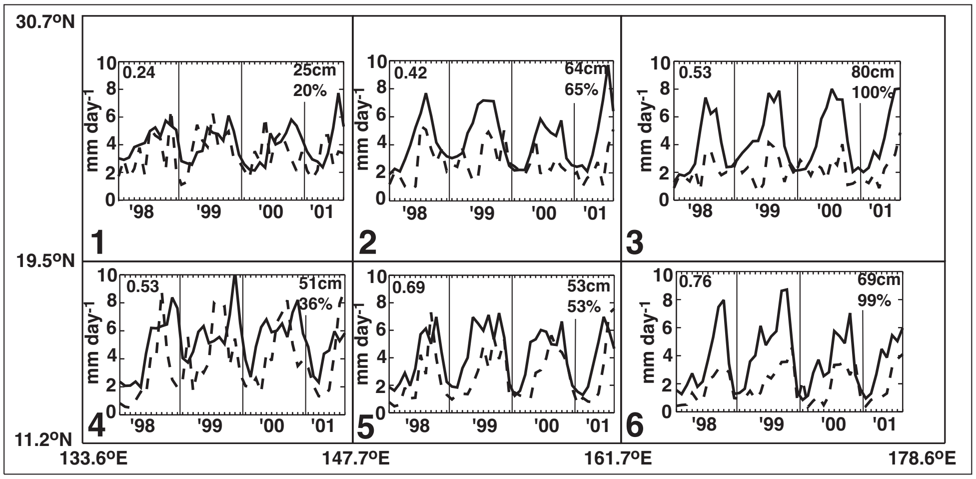

Fig. 14. Same as in Figure 9 except for the northwestern tropical Pacific Ocean region (boxes 19E and 20E of Figure 8(b).)

except to conclude that the model appears to behave as it does over the Arabian peninsula, simulating unrealistic wet seasons, during which precipitation rates are too high compared to the observations. In box 6, where an annual cycle appears slightly better supported, the model's wet bias is over 100% during the wet season months.

The most remarkable feature of the model's performance in boxes 21E and 22E of Figure 8(b) (partitioned in Figure 15) is its close agreement with TRMM observations over New Guinea and Papua New Guinea (box 4). Absolute and relative differences in total precipitation in box 4 are particularly small. However, in the other 5 subdivisions, the comparison is quite poor. For example, in boxes 1 and 2, CCM3 overestimates DJF precipitation by about 100%. Here, as over the Arabian peninsula and in subregions of the northwestern tropical Pacific, the model appears to be simulating an unrealistic wet season. The wet bias is of a similar magnitude in box 3, though it resides in JJA, where a wet season

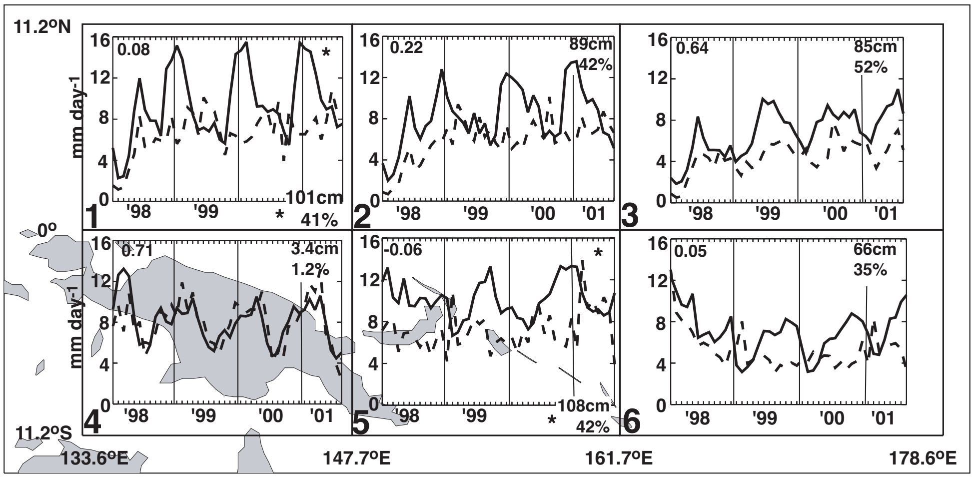

Fig. 15. Same as in Figure 9 except for the western equatorial Pacific Ocean region (boxes 21E and 22E of Figure 8(b).)

actually appears supported by TRMM observations. In boxes 5 and 6, the model appears to be tracking the overall trend in the precipitation observed by the satellite, but there are periods of excessive precipitation, particularly in the latter halves of 1999 and 2000.

f. Region F: the Southern Eastern Hemisphere

In contrast to the previous regions discussed, there is very little to be criticized of the model's performance in the southern Eastern Hemisphere. Annual cycles and magnitudes of precipitation are simulated quite well from southern Africa to Australia. Absolute differences in total precipitation are generally less than half a meter per year and relative differences are generally less than 60%. Where its measure is useful, the rank correlation between CCM3 and TRMM is high, indicating the model's success in capturing the annual cycle. The largest differences in total precipitation are found in boxes 11E and 12E of the southern Indian Ocean. These are caused by a small, consistent month-to-month model wet bias. Overall, the model's simulation over Region F is a testament to the fact that, in certain areas, CCM3 can simulate both wet and dry climates well, since they are both present here; contrast box 23E with box 18E, for example.

g. Summary

The results of this study illustrate that there are large regions of the Tropics in which monthly-mean precipitation rates, computed from an ensemble of CCM3 simulations, disagree with those computed from observations made by the TRMM satellite. Similarly, there are large regions where CCM3 and TRMM monthly means agree well. We summarize the differences on fairly coarse regional and subregional scales in Figure 16. The top two panels ((a) and (b)) plot categorical absolute and relative differences in total (44-month) precipitation for the previously-examined subregions. The bottom plot (c) labels the differences as occurring in the wet season (W) or in the dry season (D), as phase differences (P), or as differences which are consistent throughout the period or have no discernible seasonal variation to them (C), or which are associated with artificial wet seasons created by the model (A). The model's bias is indicated by a + or a - for wet or dry respectively.

Where there are differences, they are almost universally positive, indicating the model's wet bias throughout the Tropics. Negative model - satellite differences evident in the annual-difference plot (Figure 6(c)) are not nearly as large on the regional and subregional scales considered here; the positive differences are far more prominent. The only exception is in the interior Guinea lands of western Africa (near the intersection of the Prime Meridian and 15°N). Here, the model consistently underestimates wet-season precipitation. Regions where absolute differences are large and positive correspond to regions where CCM3 simulates too much condensational heating, and unrealistically large amounts of latent energy

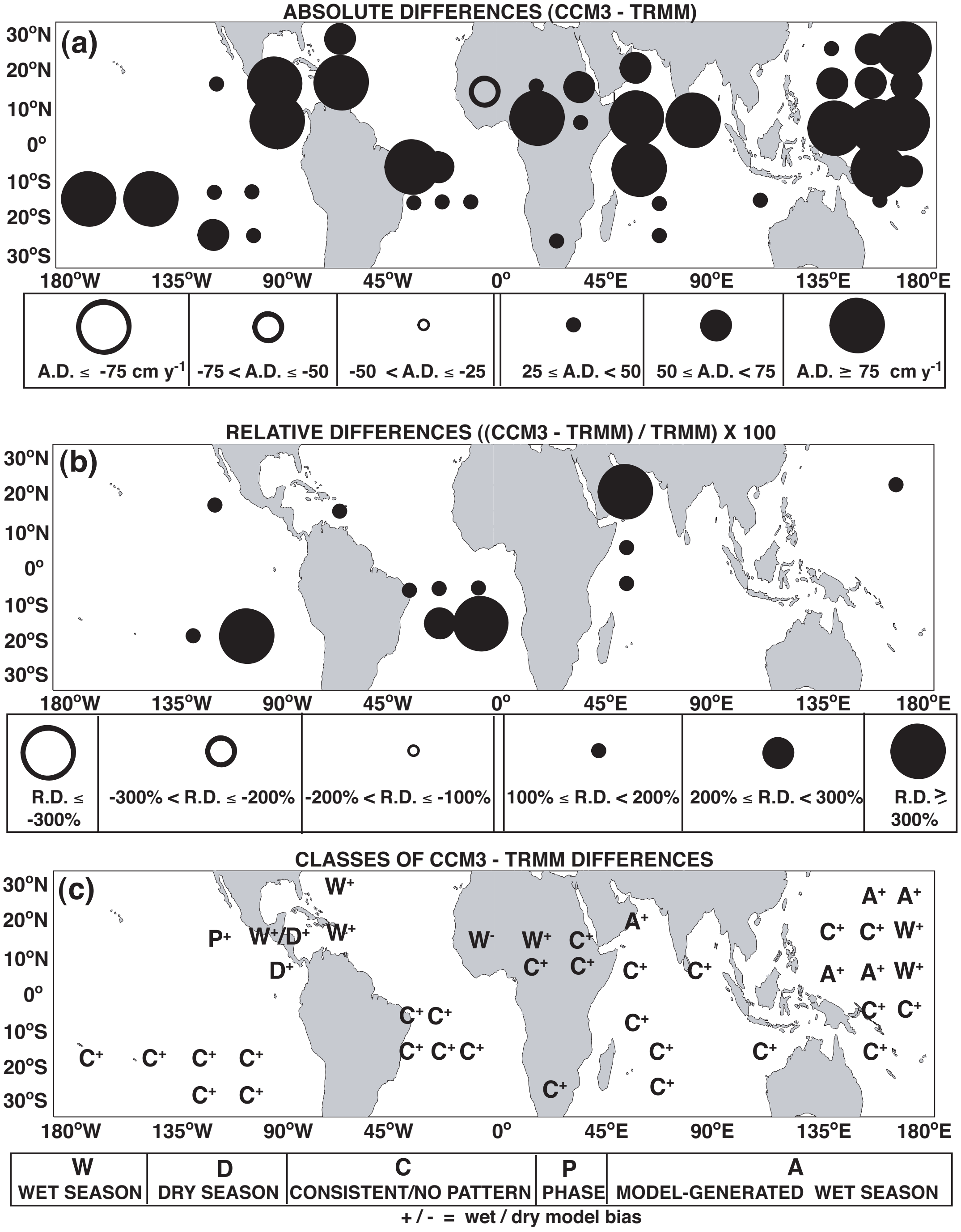

Fig. 16. Categorical absolute (a) and relative differences (b) between CCM3 and TRMM total precipitation for the 44-month comparison period. Types of model - satellite differences are plotted in (c), where a + or a - refers to the model's wet or dry bias respectively. Each location corresponds to one of the subregions examined above.

can have effects on the simulation of the general circulation. In the central south Pacific, the large positive absolute differences between the model and satellite monthly means are most likely caused by the model's generation of a South Pacific Convergence Zone (SPCZ) which is too large and too intense. Outside this region, the largest positive absolute differences tend to be north of 10°S and along the western edges of the Atlantic, the Indian, and the Pacific ocean basins. North of the Equator, about half of the largest model - satellite differences are wet biases in the wet season or wet biases in model-generated artificial wet seasons. South of the Equator, they are all wet biases with no seasonal dependence.

In locations where absolute differences are large, CCM3 does a poor job of simulating both precipitation and latent heating. However, there are locations where absolute differences are comparatively small but relative differences are extreme. Prime examples include portions of the Arabian peninsula and the southern tropical Atlantic, where absolute differences in total precipitation are less than 75 cm year^{-1}, but relative differences are greater than 300% and 700% respectively. In such regions, the model's over-release of latent energy is not as important as its failure to simulate what is climatologically reasonable "weather".

It should be noted that the previous analysis has not distinguished between the convective and large-scale stable parts of the model's precipitation. However, the precipitation as simulated by CCM3 in the Tropics is overwhelmingly convective in nature. See Figure 17, which shows the magnitudes of model-generated precipitation, partitioned into its convective and large-scale stable parts, and TRMM-observed precipitation, totaled over the comparison period. In all regions, the model's large-scale stable portion is smaller than not only its convective portion but also the portion observed by TRMM. Thus the model's wet biases are wet biases in convective precipitation.

In light of the problem regions described above, the model's simulation of the annual cycle of precipitation agrees quite well with the TRMM observations over South America

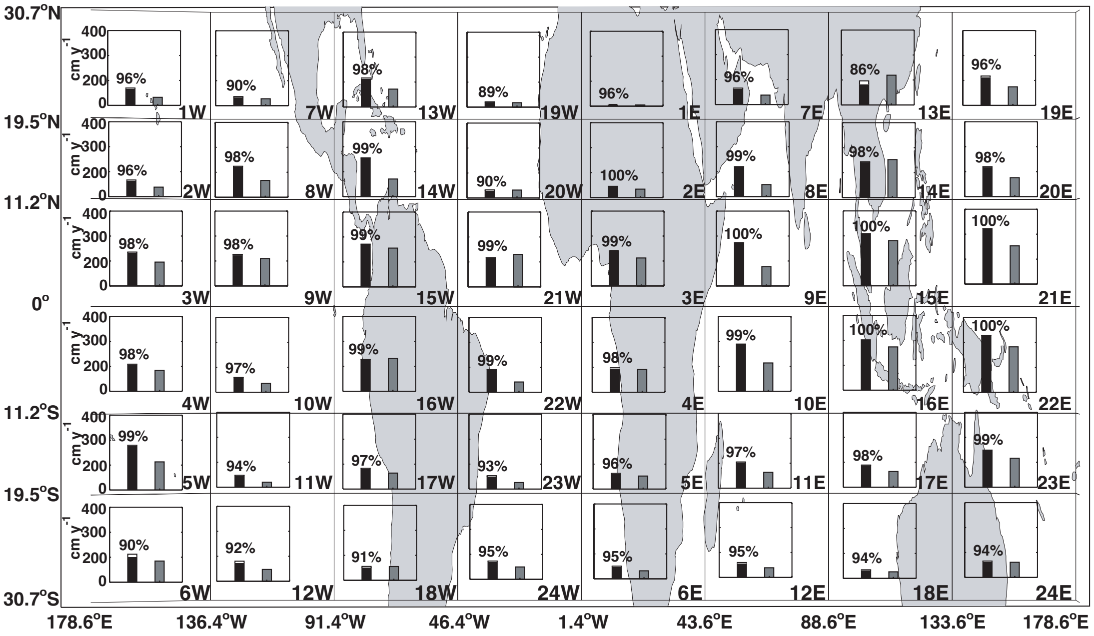

Fig. 17. Bar charts representing the magnitudes of 44-month total precipitation in cm y^{-1} as simulated by CCM3 and as observed by TRMM. The CCM3 precipitation bar (on the left) is partitioned into a convective part (black) and large-scale stable part (white). The percentage of the CCM3 precipitation that is convective is written above the CCM3 bar. The TRMM (TMI+PR) precipitation bar is shown in dark gray.

and most of the southern Eastern Hemisphere (generally south of 10°S), including Australia and southern Africa. Over these regions, absolute and relative differences between the model- and satellite-derived monthly means are small, and the rank correlations are large. In general, the model's wet bias throughout the Tropics tends to be smaller over the Southern Hemisphere than over the Northern Hemisphere, and it tends to be smaller over land than over ocean. This general conclusion is supported by scatter plots of the regional-mean monthly-mean CCM3 and TRMM precipitation rates, specific to hemisphere and land/ocean (see Figure 18).

B. Comparison of Diurnal Cycles

Many previous studies have investigated the diurnal cycle of precipitation and/or convection over ocean and over land, as measured by various Earth-observing systems. Well over 100 studies document the phenomenon (Wallace 1975). While these studies generally agree that the magnitude of the diurnal cycle is larger over the continents than over the oceans, several also show that land regions exhibit maxima in precipitation between noon and midnight while ocean regions have maxima between midnight and noon. In Tropical latitudes, these studies include analyses of surface-based measurements from island and continental stations from the Tropical West Pacific to South America and Africa (Gray and Jacobson 1977); reflectivity and microwave data from the Tropical Rainfall Measuring Mission (TRMM) satellite (Nesbitt and Zipser 2003); infrared, passive microwave, and gauge data (Janowiak et al. 1994); infrared data from American geostationary satellites (Meisner and Arkin 1987); microwave data from the Defense Meteorological Satellite Program (DMSP) satellite (Sharma et al. 1991); and gauge data from the Tropical Atmosphere Ocean (TAO) mooring array for the Coupled Ocean Atmosphere Response Experiment (COARE) (Cronin and McPhaden 1999). However, regional exceptions have

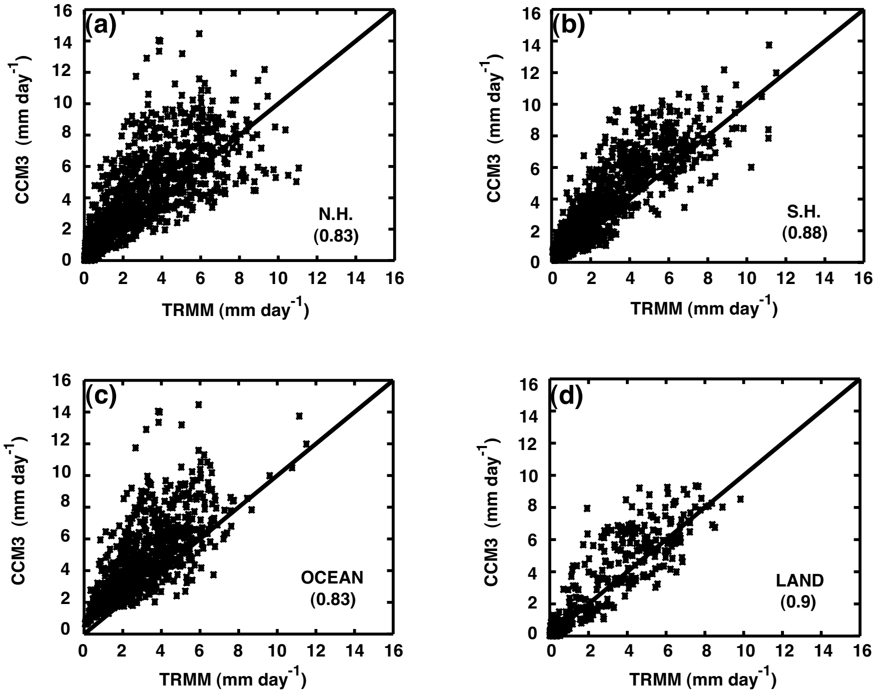

Fig. 18. Scatter plots of CCM3 and TRMM regional-mean monthly-mean precipitation rates (mm day^{-1}) for Northern Hemisphere (a), Southern Hemisphere (b), ocean (c), and land (d) regions. Rank correlation coefficients are printed in the lower right-hand corner of each plot. The solid black line represents the line of unit correlation.

been found (e.g., the eastern Atlantic (McGarry and Reed 1978; Reed and Jaffe 1981), the southern Pacific and Atlantic Ocean dry zones (Chang et al. 1995), and the South Pacific Convergence Zone (SPCZ) (Albright et al. 1985)). In addition, the diurnal variation itself can depend on the intensity of precipitation (i.e., drizzle vs. thunderstorms) (Dai 2001).

As observational studies abound, so do studies on the causes of the diurnal cycle of precipitation and why it varies geographically and, in general, from land to ocean. According to (Wallace 1975), the theories for the diurnal cycle of convectively-based precipitation over land can fall into one of two categories. The first consists of theories based on thermodynamic processes which affect static stability; the second groups together theories which explain the diurnal cycle of convection by dynamical processes affecting convergence in the boundary layer, such as the land and seabreeze circulations in coastal areas. For the oceanic diurnal cycle, theories have been proposed by (Kraus 1963), (Brier and Simpson 1969), and (Gray and Jacobson 1977), among others and are summarized nicely by (Nesbitt and Zipser 2003). The cause for the morning peak remains widely debated.

General circulation models should simulate accurate monthly-mean precipitation amounts for the right reasons (Trenberth et al. 2003), simulating the local timing correctly. A variety of studies have used observations of the diurnal cycle to compare with modeling results. Examples include analysis of output from the Colorado State University General Circulation Model over Tropical lands and oceans ((Randall et al. 1991)) and over South America ((Lin et al. 2000)), output from the NCAR Community Climate Model Ver. 2 (CCM2) ((Chen et al. 1996)) and CCM3 ((Dai et al. 1999)) over the U.S., output from the NCAR Community Climate System Model version 2 (CCSM2) ((Dai and Trenberth 2004)), and output from the European Centre for Medium-Range Weather Forecasts (ECMWF) model over Amazonia (Betts and Jakob (2002a), (Betts and Jakob 2002b)). We apply a similar evaluation to CCM3 in the Tropics.

For the diurnal cycle comparison, a different regional grid is used than that used for the annual cycle comparison. Regions in this comparison are roughly 15° longitude east to west so that each column represents a particular local hour. The regions are roughly 10° latitude south to north. Figure 19 shows the map of the regions used in this analysis.

Figure 20 shows how many times the diurnal cycle is sampled by TRMM within each of the regions. Note that there is a maximum number of observations in the northernmost and southernmost rows of regions. These regions are near the highest latitudes sampled by the TRMM satellite. At these latitudes, the satellite orbit is nearly parallel to the latitude lines, so more samples are collected than at lower latitudes.

a. Harmonic analysis

The phases and amplitudes of the diurnal cycles, as simulated by CCM3 and as observed by TRMM, are compared on a regional basis as follows. We compute the regional-mean precipitation rate at hour h of day d, $\overline{r(h,d)}$, by averaging over all 2.8°× 2.8° grid boxes $i = 1, \ldots, S$ within the region:

$$\overline{r(h,d)} = \sum_{i=1}^{S} w(h,d)_i r(h,d)_i, \tag{5.1}$$

where

$$w(h,d)_i = \begin{cases} 1/S & \text{for CCM3} \\ \frac{\alpha(h,d)_i}{\sum_{i'=1}^{S} \alpha(h,d)_{i'}} & \text{for TRMM,} \end{cases}$$

such that $\alpha(h,d)_i$ is the fractional area observed by TRMM in grid box i at time (h,d). Next, we compute the "climatological-mean" regional-mean precipitation rate at hour h, $R(h)$, by averaging the regional mean at this hour over all days in the comparison period ($d = 1, \ldots, D = 1338$) using the time analogue of (5.1):

$$R(h) = \sum_{d=1}^{D} W(h,d)\overline{r(h,d)}, \tag{5.2}$$

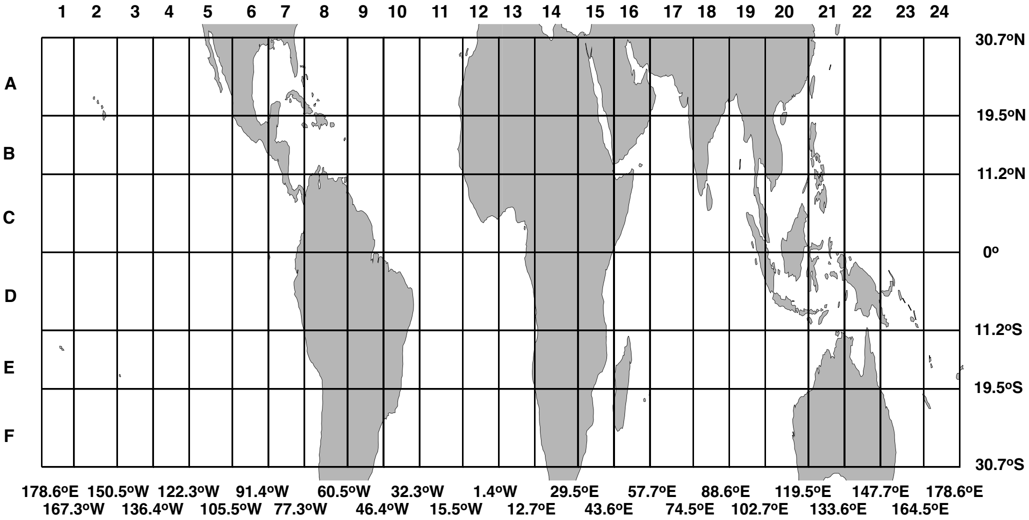

Fig. 19. Map of the 144 regions used for the diurnal cycle comparison. Climatological-mean hourly precipitation rates from CCM3 and from TRMM are averaged over each of the above regions. Note that the grid appears irregular due to the fact that the region boundaries were chosen to line up with the model's grid, which is irregularly spaced.

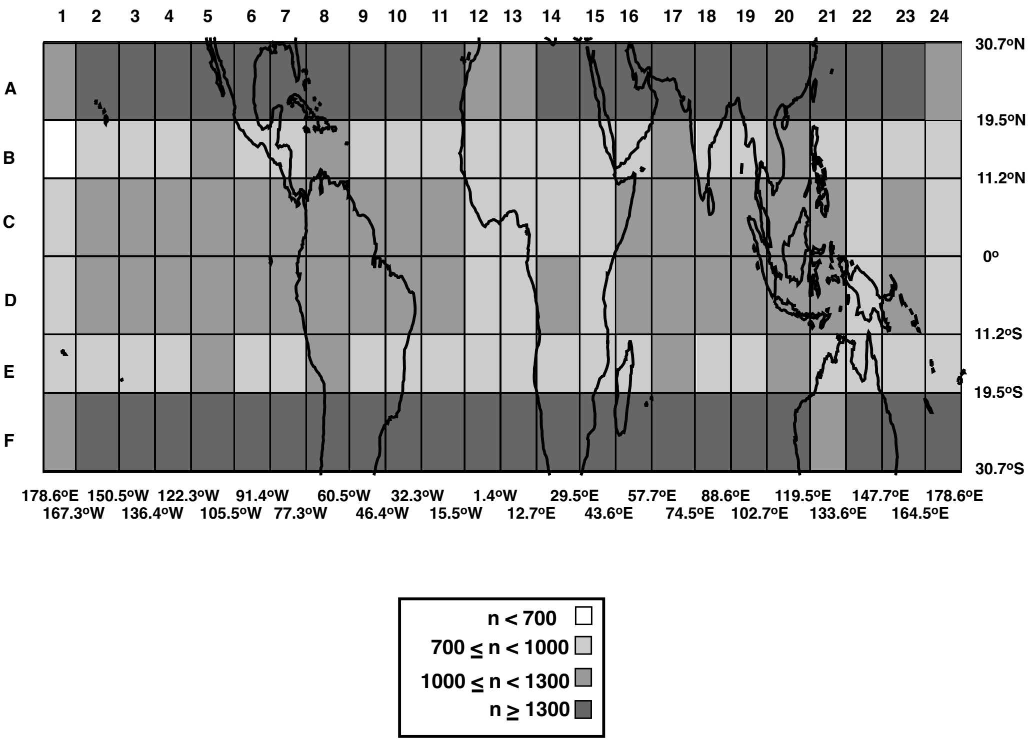

Fig. 20. Number of samples by the TRMM satellite of the diurnal cycle of precipitation for the 144 regions used in the comparison. The period spans 44 months, from January, 1998 through August, 2001.

where

$$W(h,d) = \begin{cases} 1/D & \text{for CCM3} \\ \frac{A(h,d)}{\sum_{d'=1}^{D} A(h,d')} & \text{for TRMM precipitation rates,} \end{cases}$$

such that $A(h,d) = \sum_{i=1}^{S} \alpha(h,d)_i$. The climatological-mean regional-mean hourly precipitation rates $R(h)$, $h = 0.5, 1.5, \ldots, 23.5$, then are fit to the following model:

$$f(h) = a \cos \frac{2\pi k}{N} h + b \sin \frac{2\pi k}{N} h + c, \tag{5.3}$$

such that

$$R(h) = f(h) + \delta(h), \tag{5.4}$$

where $N = 24$, $k = N/24$ for the 24-hour (diurnal) harmonic, and $\delta(h)$ is a residual such that $E[\delta(h)] = 0$, $E[\delta(h)^2] = \sigma^2$, and $E[\delta(h)\delta(h')] \neq 0$, $h \neq h'$. Parameters a, b, and c are determined by linear least-squares regression and are equivalent to those obtained by fitting the regional means $\overline{r(h,d)}$, to (5.3) with $N = 24D$ and $k = D$ for all $h = 0.5, \ldots, 23.5$ and $d = 1, \ldots, D = 1338$. Note that we use a weighted linear least-squares regression for the TRMM means, where the weight at each hour h is proportional to the area of the region observed at h totaled over all days in the 44-month comparison period.

Alternately, (5.3) can be expressed as

$$f(h) = A \cos\left(\frac{2\pi k}{N} h - \phi\right) + c, \tag{5.5}$$

where $A = \sqrt{a^2 + b^2}$ and $\phi = \arctan(b/a)$, representing the amplitude and phase of the diurnal cycle respectively. The test to verify the least-squares estimates of A and ϕ yields the following condition on the underlying least-squares estimates of parameters a and b:

$$(\hat{a} - a)^2 + \left(\hat{b} - b\right)^2 \leq \frac{4s^2}{N} F_{2;N-3}(\epsilon), \tag{5.6}$$

where s^2 is the least-squares estimate of σ^2 and $F_{2;N-3}$ is the $(1-\epsilon)$ cutoff value of the

F probability distribution function with 2 and (24(samples) - 3(coefficients) =) 21 degrees of freedom. The confidence region is then the circumference and interior of the circle with center (a, b) and radius $\sqrt{4s^2F_{2,21}(\epsilon)/24}$. It is important to note that this test assumes that the data we fit to (5.3) are independent and that the resulting residuals of the fit are normally distributed. While these assumptions may not be valid in the strictest sense, a $(1-\epsilon)$% confidence circle still provides a useful metric for this comparison, as its size is directly proportional to the sum of the squared differences (s^2) between the fit and the data. For our purposes we set $\epsilon = 0.05$ and use the resulting circle to represent the *uncertainty* associated with fitting $R(h)$ to $f(h)$. Contained within each *uncertainty circle* are points (A, ϕ) which may be assumed to represent $f(h)$ within a constant level of uncertainty. Assuming the data are independent and that the residuals are normally-distributed, all points (A, ϕ) within the circle would pass the goodness-of-fit test at the 95% level. For further details on the statistical test, we refer the reader to Anderson (1978).

Figure 21 demonstrates the application of the above method to a region in western Africa (region 12B). The top panel of the figure shows a least-squares fit to the climatological-mean regional-mean diurnal cycle as observed by TRMM and as simulated by CCM3. In the bottom panel, the phases and amplitudes of the harmonic fits to the diurnal cycles are represented by arrows and uncertainty circles as cast into the standard 24-hour clock. For both the CCM3 and TRMM results, the uncertainty circle gives an estimate of the sampling error associated with fitting the diurnal cycle. Due to the large sample size, the CCM3 sampling errors are generally small. Because the TRMM sample sizes are much smaller, sampling errors can be substantial. In the following discussion, results will be presented in the above arrow - circle format. In general, differences in phase and magnitude between the model output and the satellite data are measured based on distances between the arrowheads, which represent the *most likely* values of amplitude and phase.

Figure 22 shows the phases and relative amplitudes of the diurnal harmonic fits to the

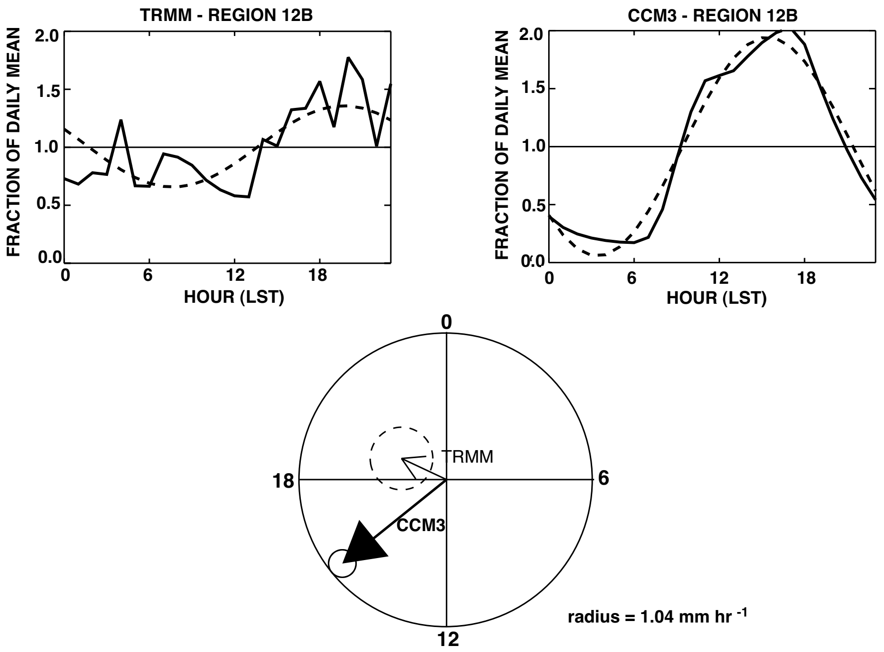

Fig. 21. The TRMM (top left) and CCM3 (top right) climatological-mean hourly precipitation as a fraction of daily mean (solid) and the diurnal harmonic fit (dashed) for region 12B. In the bottom panel, the phases and amplitudes of the diurnal cycles are represented by arrows (CCM3: heavy; TRMM: light) and uncertainty circles (CCM3: solid; TRMM: dashed). A circle which surrounds the arrow's origin indicates that the diurnal harmonic fit is not significant at the 5% level. For clarity, the arrows and associated uncertainty circles have been scaled by a common scale factor.

climatological-mean regional-mean diurnal cycles of precipitation for all regions between the International Date Line and 90°W. Each arrow-circle diagram is plotted on top of its region on the map, where north indicates hour 0, east indicates hour 6, south indicates hour 12, and west indicates hour 18, all hours in local standard time. As in Figure 21, the uncertainty circles provide bounds on a range of amplitudes and phases that fit the diurnal harmonic, in as much as it is an appropriate model. If the uncertainty circle surrounds the origin of its arrow, an amplitude of zero is possible, indicating that the precipitation over the associated region demonstrates no significant diurnal signal. If the CCM3 circle overlaps the TRMM circle, and if neither circle surrounds the origin of its arrow, the phase and magnitude differences between the diurnal cycles lie within the measured uncertainty of the fit, and thus are not significantly different. It is important to note that for each region, the lengths of both arrows and the radii of the uncertainty circles have been magnified (or demagnified) by a scale factor common to the region. The scaling was done so that the diagrams from all regions could be seen, since the diurnal cycles over some regions are much stronger than those over others. As a result, the amplitudes of the diurnal cycles cannot be compared *between* regions. The level of magnification is indicated by background shading in the region (lightest shading represents a downscaling (less than 100%) or slight upscaling (between 100% and 200%) while darkest shading represents a large upscaling (greater or equal to 600%)). The largest magnification is done where diurnal signals are weak.

For most of these regions, the model simulates diurnal variations of precipitation that are statistically significant. However, in some regions, a great amount of magnification is needed in order to see them (i.e., the southwestern regions 1E, 2E, 1F, and 2F). In most regions, there is very little uncertainty with the diurnal harmonic fit to the CCM3 output, both in amplitude and in phase. The model simulates an early-morning peak in the day's precipitation in nearly all regions, save regions close to Central America (5A, 6A, 6B, and 6C). These are coastal regions, where there may be competing influences from differing

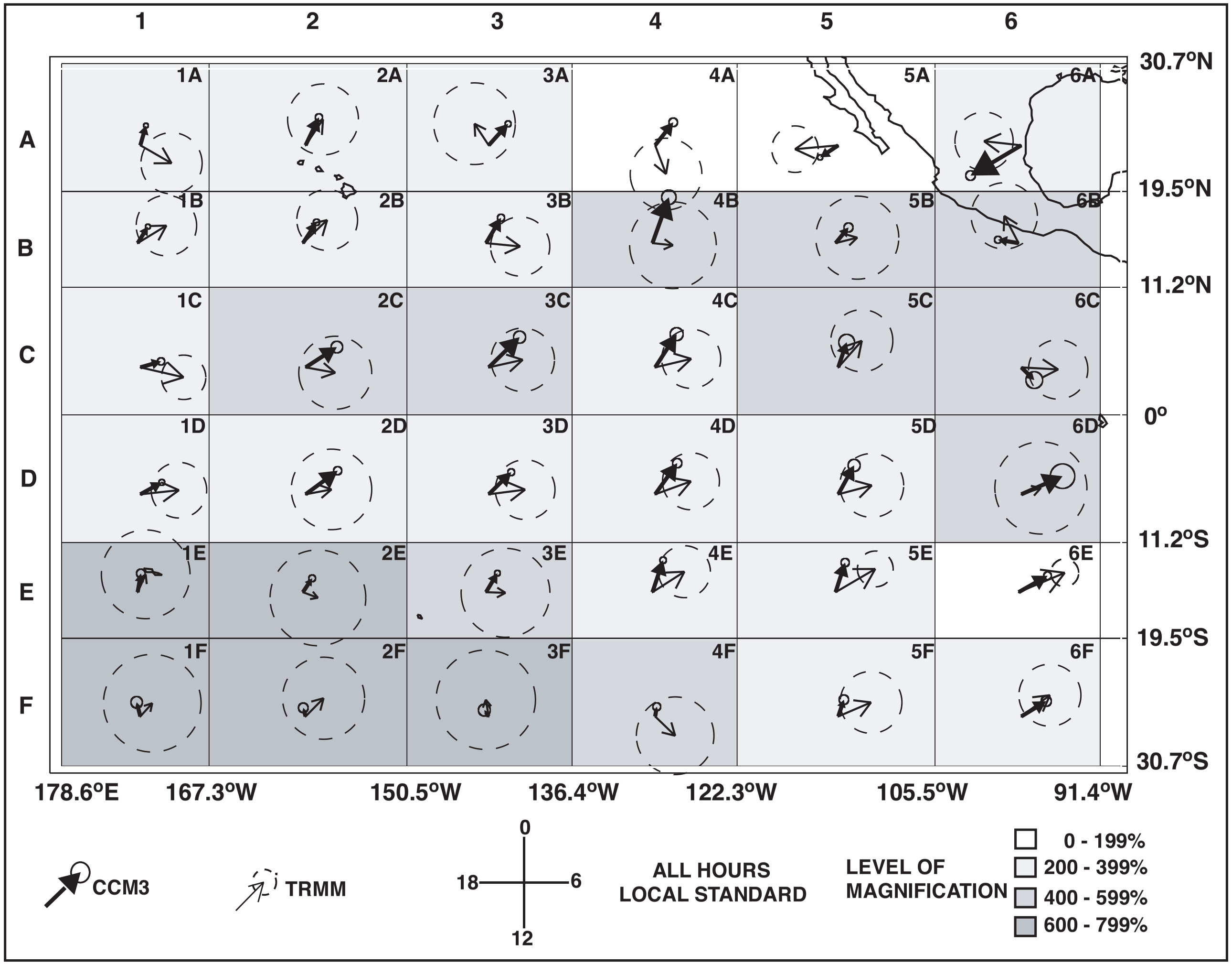

Fig. 22. Phase of the climatological-mean diurnal cycle for regions between the International Date Line and 90°W (CCM3: heavy arrow; TRMM: light arrow), with associated circles of uncertainty.

diurnal cycles over land and ocean. Region 6A is primarily continental. For most regions, the TRMM uncertainty circles surround the origins of its arrows. Thus, if the statistical assumptions stated above are approximately valid, then for most regions, the TRMM results are not statistically significant at the 5% level. However, the TRMM amplitudes are generally consistent with those of the model, while the TRMM phases are consistently several hours later than those of the model. There are a few exceptions where phases compare quite well. These are found near the western and eastern boundaries of the zone (in 2A, 2B, and 1E and 6D, 6E, and 6F respectively). Amplitudes do not agree quite as well in the eastern boxes (6D, 6E, and 6F), with CCM3 about twice as large as TRMM in 6D and less than half as large in 6E and 6F. To make conclusions about model-satellite differences over the remaining area in this sector, we average the TRMM data over even larger regions, or“zones”, as seen in Figure 23 and recompute our least-squares fit parameters.

The results of the least-squares fits to the climatological-mean zone-mean hourly precipitation rates for the northeastern Tropical Pacific zone are shown in Figure 24(a). Averaging the TRMM data over this large zone significantly reduces the size of the TRMM uncertainty circle, as seen in the corresponding individual regions. Both the diurnal cycles in CCM3 and in TRMM are of about the same magnitude, roughly 10-15% of the daily mean, and thus are relatively weak over this oceanic zone. Both exhibit early morning peaks in precipitation, though that for CCM3 precedes that of TRMM by approximately 2 hours. Over the southeastern Tropical Pacific Ocean zone to the south (Figure 24(b), the amplitudes of the diurnal cycles are comparable (about 10 - 15% of the daily mean), but the phases differ by 3 hours, with CCM3 leading TRMM, although the uncertainty circles are fairly large.

Figure 25 shows the phases and magnitudes of the diurnal harmonic fits to the diurnal cycles in regions between 90°W and the Prime Meridian. This sector of the Tropics provides a nice sample of the diurnal cycle over both ocean and land. We begin over South

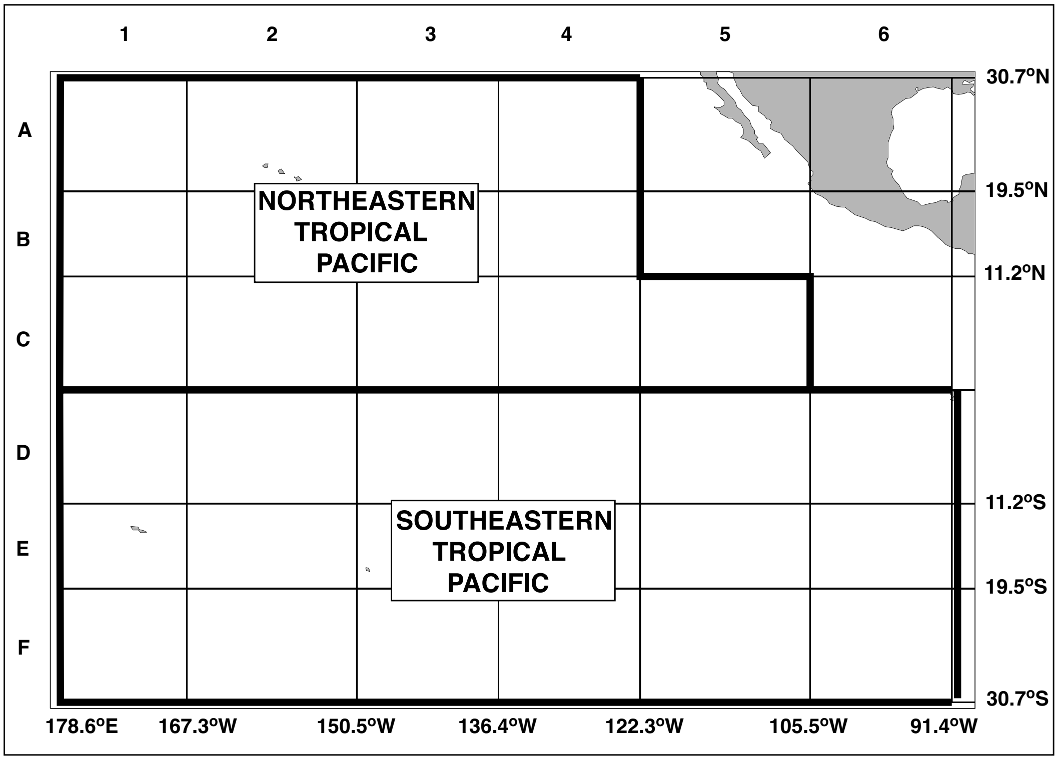

Fig. 23. Map showing the boundaries of the two zones between the International Date Line and 90°W over which CCM3 and TRMM hourly precipitation rates were averaged for comparison.

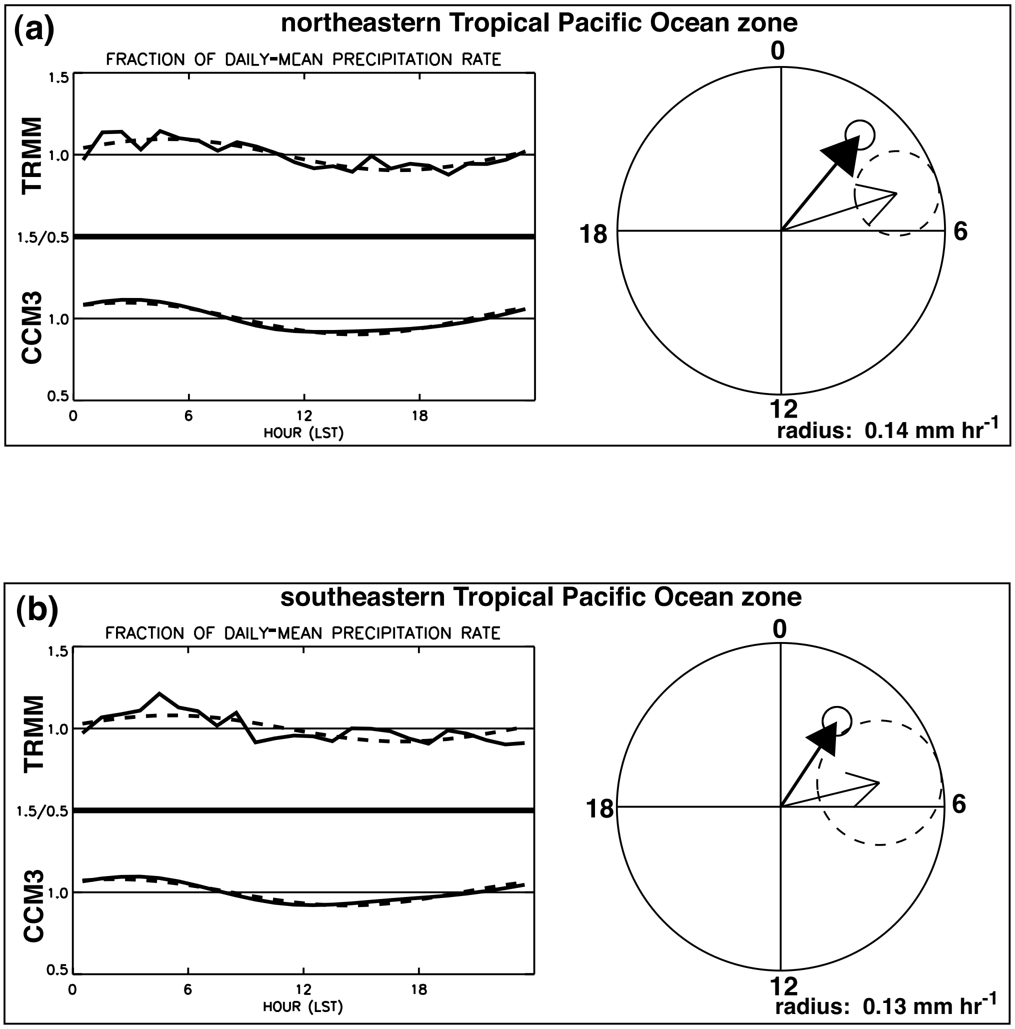

Fig. 24. The TRMM and CCM3 climatological-mean hourly precipitation for the northeastern Tropical Pacific Ocean zone (a) and for the southeastern Pacific Ocean zone (b), expressed as a fraction of daily mean (solid) with its diurnal harmonic fit (dashed) on the left. On the right, the phases and amplitudes of the diurnal harmonic fits are expressed in arrow-uncertainty circle format (CCM3: heavy arrow, solid circle; TRMM: light arrow, dashed circle).

America, where the comparison between CCM3 and TRMM is relatively straightforward: uncertainty circles are not too large in these regions. CCM3 demonstrates peaks in daily rainfall during the early to mid-afternoon hours (evening in the eastern coastal regions, where the diurnal cycle of the oceans may be mixed in). Over these regions, the model is in fair agreement with TRMM in terms of the timing of the peak. Such an agreement is particularly evident in regions 8D, 9D, and 9F, and not so much in region 9E, where the model's peak precedes that of the observations by nearly 2 hours. Despite its reasonable success with timing for most regions of South America, the model overestimates the amplitude of the diurnal variation, relative to the observations. For example, in region 9F, the model's amplitude is about 4 times as large as TRMM's. Again, region 9E looks to be the exception. Though the phases do not agree as well in this region, the magnitudes of diurnal variation are comparable.

The model-satellite comparison is relatively straightforward over western Africa (regions 12A and 12B). Here the uncertainties associated with the TRMM fits to the diurnal harmonics are comparatively small. In region 12A, the model and satellite differ substantially in phase and in amplitude, with the model preceding TRMM by nearly 11 hours in its daily precipitation peak, exhibiting the maximum precipitation during the morning instead of during the afternoon. In addition, the amplitude of the model's peak is at least 50% smaller. By contrast, in region 12B, the model's diurnal harmonic amplitude is at least twice that of TRMM and the peak in its harmonic is only about 4 hours earlier.

In regions of the northern Tropical Atlantic (rows A and B, columns 9 and 10), there is much uncertainty in the TRMM fits, and averaging more of the TRMM data together may support more conclusive comparisons (see below). In the southern Tropical Atlantic, south of the Equator and east of South America, (rows D, E, and F, columns 11 and 12), there are similarly-large uncertainties (regions 11F, 12D and 12F especially). The exceptions lie in regions 11D, 11E, and 12E. The model's peak in daily rainfall is seen to precede that

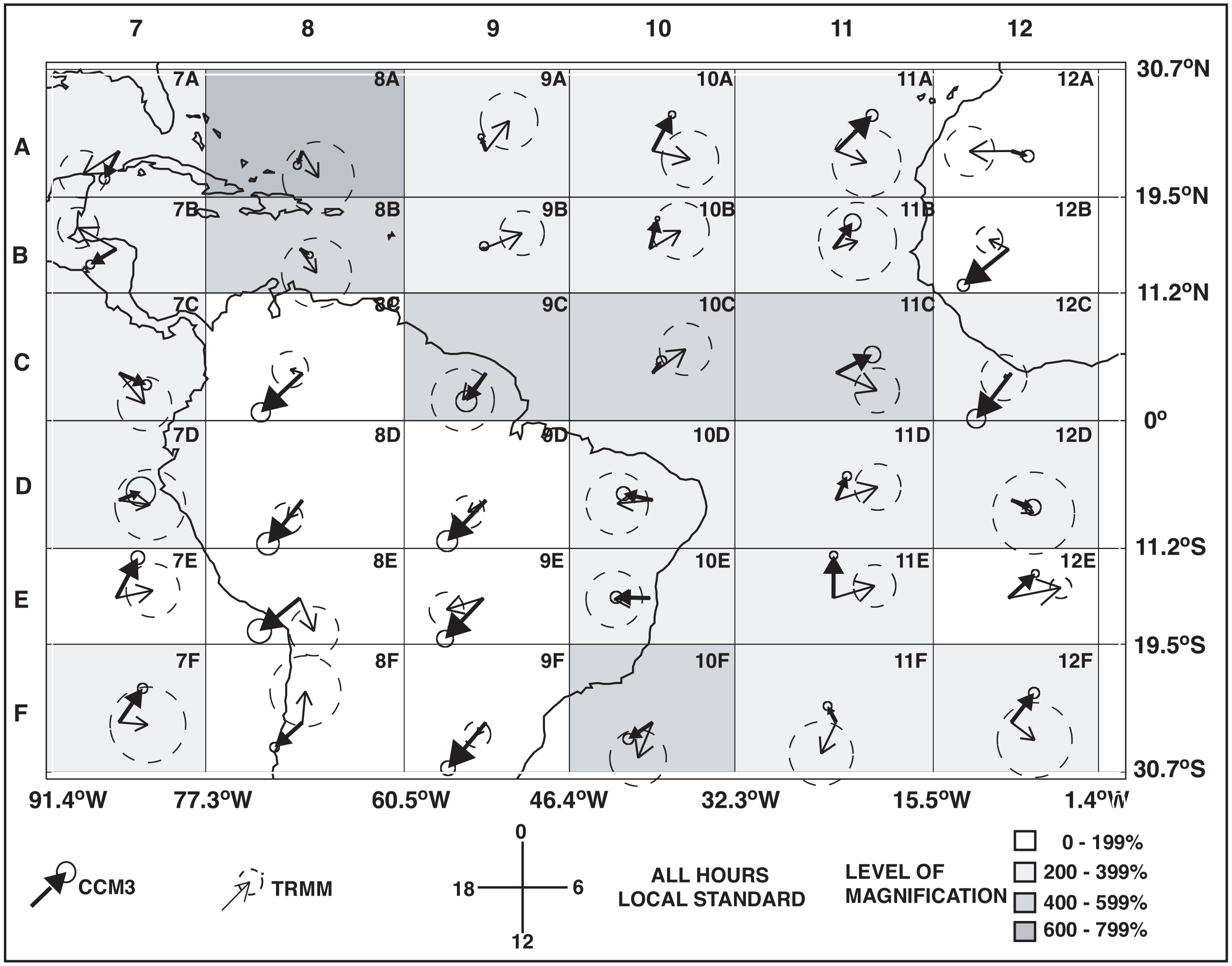

Fig. 25. Same as in Figure 22 except for regions between 90°W and the Prime Meridian.

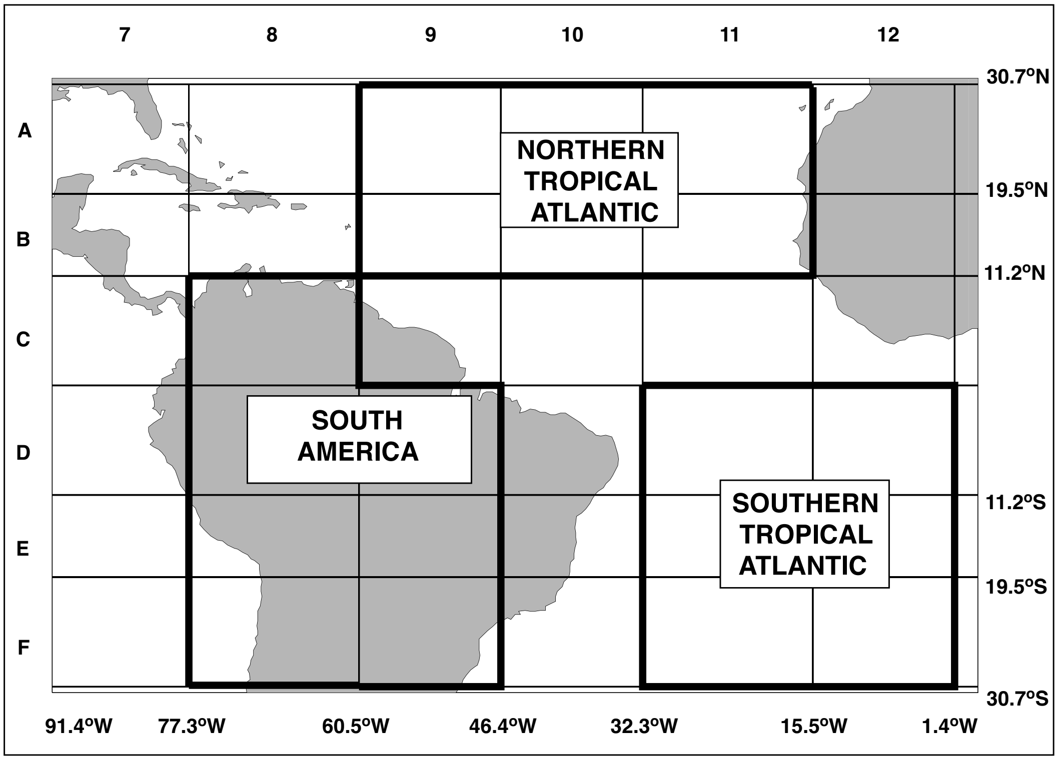

Fig. 26. Map showing the boundaries of the three zones between 90°W and the Prime Meridian over which CCM3 and TRMM hourly precipitation rates were averaged for comparison.

of the observations by about 2 hours in 12E, by 3 hours in 11D, and by nearly 5 hours in 11E. As we do for the sector to the west, we average the model output and satellite data in this sector over larger zones, as depicted in Figure 26 and compute the least squares fits for analysis on larger scales.

Averaging the model output and satellite data over South America regions (Figure 27(a)) confirms earlier findings on the regional scale. The amplitude of the CCM3 diurnal cycle is about 3 times the amplitude of the TRMM diurnal cycle, though the phases of the diurnal cycles are reasonably collocated in time, in mid-afternoon. For the northern Tropical Atlantic zone (Figure 27(b)), averaging does little to reduce the size of the uncertainty circle surrounding the TRMM arrow. However, it is clear that both the model and satellite show daily rainfall peaks in the early morning hours (between midnight and dawn), with the CCM3 peak coming about 3 to 4 hours before the TRMM peak. Over the southern Tropical Atlantic zone (Figure 27(c)), the TRMM uncertainty circle is large enough to indicate that there is no significant diurnal cycle present in the data. The large uncertainty might result from averaging over too many regions here, lumping together regions whose fits to the diurnal harmonic widely differ.

Figure 28 shows the phases and amplitudes of the fits of the CCM3 and TRMM precipitation rates to the diurnal harmonic for regions between the Prime Meridian and 90°E. Much of this sector of the Tropics is land and includes the majority of the African continent. With a few exceptions, over much of interior Africa (column 14 and regions 13A and 13B), the CCM3 diurnal cycle peaks relatively strongly in mid-afternoon, though it peaks slightly earlier in the Congo regions of 14C and 14D. In most regions, the model's peak precedes that of TRMM by 2 to 4 hours, with the largest phase differences generally located north of the Equator in regions 13B, 14B, and 14C. South of the Equator, there is slightly better agreement between the simulation and the observations. In regions 14D and 14E, the uncertainty circles overlap in phase. As for the amplitudes, CCM3 and TRMM differ most in the Congo regions 14C and 14D and agree best in regions 13B, 14B, 14E and 14F, given the size of the TRMM uncertainty circle. Regions 13A and 14A in the Sahara Desert are the significant outliers in interior Africa. In region 13A, as in region 12A (see Figure 25) to the west, CCM3 shows a peak in daily precipitation just after dawn. As they do in 12A, the satellite observations fairly certainly indicate a peak in the late afternoon or evening (between one quarter and one half of a cycle after the model). In 14A, the model exhibits a strong peak in its diurnal cycle near noon, while the TRMM satellite data show no significant diurnal cycle at all or are too sparse for a good fit. In contrast to the

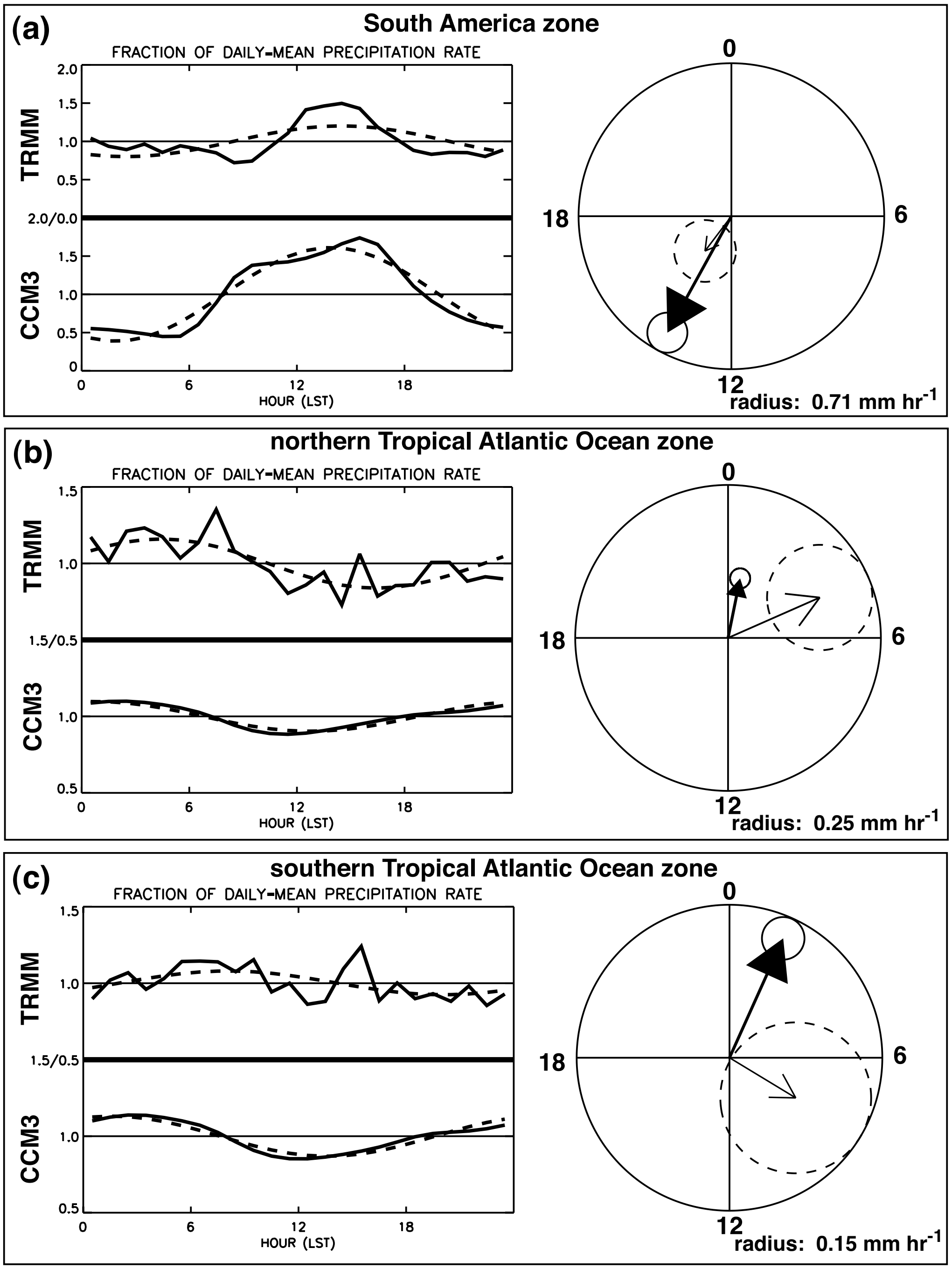

Fig. 27. Same as in Figure 24 except for the South America zone (a), the northern Tropical Atlantic Ocean zone (b), and the southern Tropical Atlantic Ocean zone (c).

inhomogeneities over interior Africa, in eastern Africa (column 15), the model output and satellite data agree rather uniformly. There is overlap in phase and in magnitude in all of these regions save 15F, with peaks in daily precipitation occurring in mid to late afternoon.

Over regions of south Asia, there is good agreement in the phase of the diurnal cycle in regions 16B and 17A with peaks in mid to late afternoon. The CCM3 amplitude is slightly smaller than that of TRMM in region 16B, but the amplitudes are comparable in 17A. In region 16A, the model produces a robust diurnal signal, which is nonexistent in the TRMM observations. Monthly-mean precipitation rates also disagree in the region, as shown in a previous section. In regions 17A and 18A, over the Indian subcontinent, the phases are in fairly good agreement, given the magnitude of the uncertainty in the fit of the TRMM data here.

Over the Indian Ocean, it is difficult to make a comparison between the model and the satellite. The uncertainties associated with fitting the TRMM precipitation rates to the diurnal harmonic are quite large here. Where TRMM shows a significant diurnal variation (regions 17E and 18E), the model-satellite differences in phase and amplitude are generally small.

For this longitude sector, we average the output and data over large zones whose boundaries are depicted in Figure 29. Figure 30(a) shows the diurnal cycles of precipitation for TRMM and CCM3 and their fits to the diurnal harmonics for regions in the northern Africa zone. Over this zone, the CCM3 diurnal cycle is larger than that of TRMM, with the model's peak in daily rainfall occurring about 3 hours earlier than observed. As seen in the regional comparison, the difference certainly is largest over region 13A, in the Saharan Desert. Over southern Africa (Figure 30(b)), the amplitude of the model's diurnal cycle is between 50 and 60% of the daily mean while that of the observations is roughly half. The phases of the diurnal cycles are in fairly good agreement here, given the size of the TRMM uncertainty circle; however, the phase difference is more apparent in the means plot where

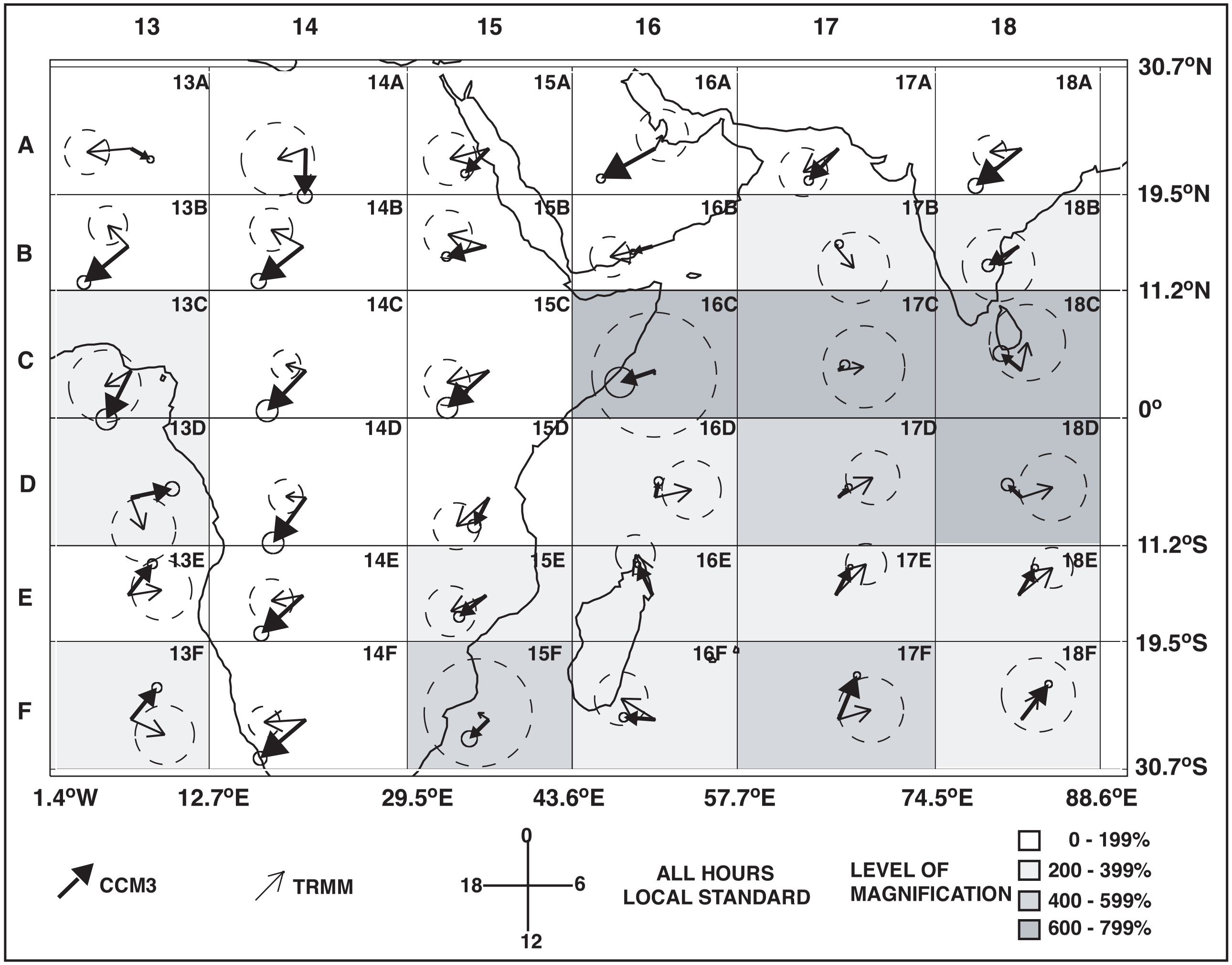

Fig. 28. Same as in Figure 22 except for regions between the Prime Meridian and 90°E.

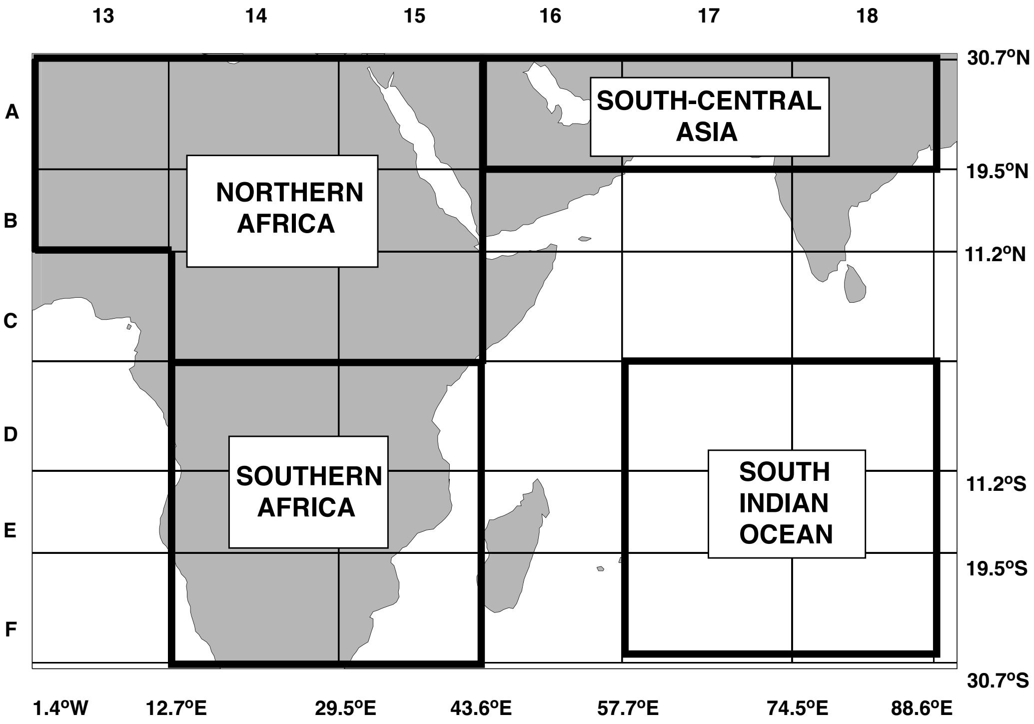

Fig. 29. Map showing the boundaries of the three zones between the Prime Meridian and 90°E over which CCM3 and TRMM hourly precipitation rates were averaged for comparison.

CCM3 leads the TRMM observations by 2 to 3 hours. In the south-central Asia zone (Figure 31(a)), the phases are in fairly good agreement, with the CCM3 arrow falling inside the TRMM uncertainty circle, whose radius indicates a peak anywhere from 1400 to approximately 1900. While the model's amplitude appears only 80% larger in the zone-mean, it should be noted that the difference is significantly larger over region 16A, the eastern Arabian peninsula, where TRMM indicates little to no regular diurnal variation at all.

Averaging the model output and satellite data over the South Indian Ocean zone (Figure 31(b)) substantially aids in the comparison of the diurnal cycles. The uncertainty asso-

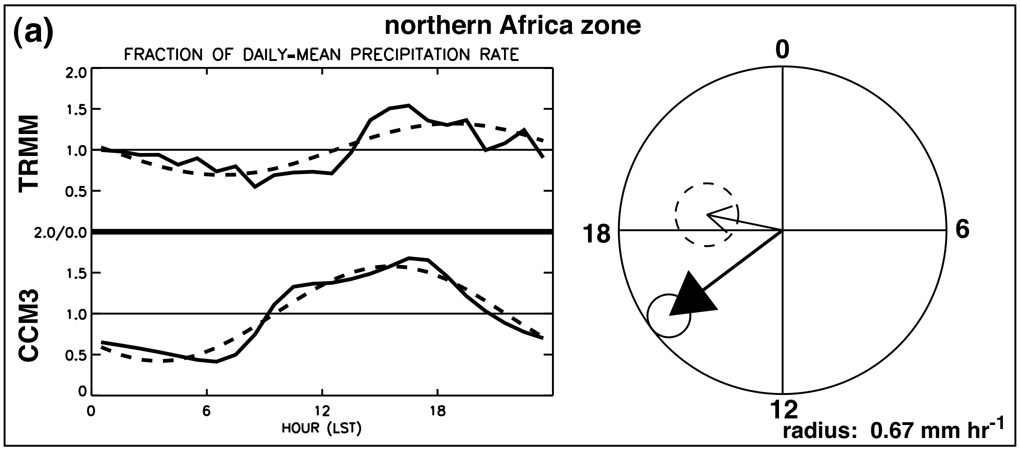

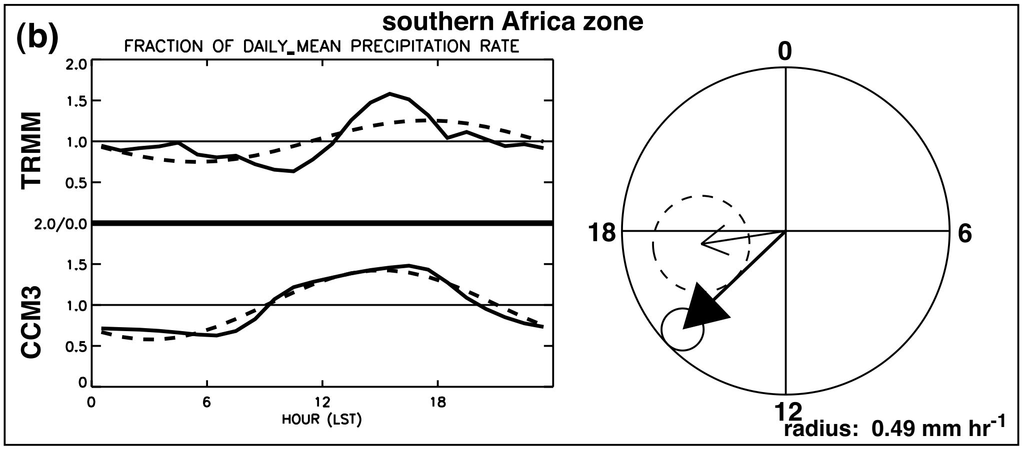

Fig. 30. Same as in Figure 24 except for the northern Africa zone (a), and the southern Africa zone (b).

ciated with the fit of the TRMM data to the diurnal harmonic is smaller at this large spatial scale. Though the diurnal cycles are quite small over this oceanic zone and require a great amount of magnification to see on the regional scales, it is evident on the zone scale that the simulated diurnal cycle is about half as large as that which is observed. Its peak, shortly after midnight, precedes that of the observations by about 2 hours.

Figure 32 shows the phases and amplitudes of the fits of the CCM3 and TRMM precipitation rates to the diurnal harmonic for regions between 90°E and the International Date Line. For many regions in this sector, large uncertainties in the least-squares estimates of the diurnal harmonics makes model-satellite comparisons difficult. There are a few exceptions where comparisons can be made easily. For example, CCM3 and TRMM compare relatively well in both phase and amplitude in region 19B. In contrast, in neighboring regions 19A and 20A, the model simulates a strong diurnal variation, which is not seen in the observations. There are two regions over the Maritime Continent in which CCM3 and TRMM can be compared easily. In region 19D over the eastern Equatorial Indian Ocean, the model-simulated diurnal cycle agrees well with the observed diurnal cycle in magnitude but precedes the observations in its peak by about 6 hours. Similarly, the magnitudes compare well in region 22D over Papua New Guinea, but the model's daily peak precedes that of TRMM by 5 to 6 hours. Farther south, over Australia, model-satellite differences are generally similar, with the model preceding the observations (only slightly in region 21F but by 3 to 4 hours in region 22F). There are model-satellite differences in both phase and magnitude over regions of the northwestern Tropical Pacific. CCM3 shows a much weaker diurnal cycle than that which is evident in the TRMM observations here. Its peak appear to precede that of TRMM by at least 10 hours in region 21A, by at least 6 hours in 23A, and by at least 4 hours in 22A. The phases agree better in 22B, 23B, 24B, 23C, and 24C to the south.

The boundaries of the zones over which we spatially average the CCM3 output and

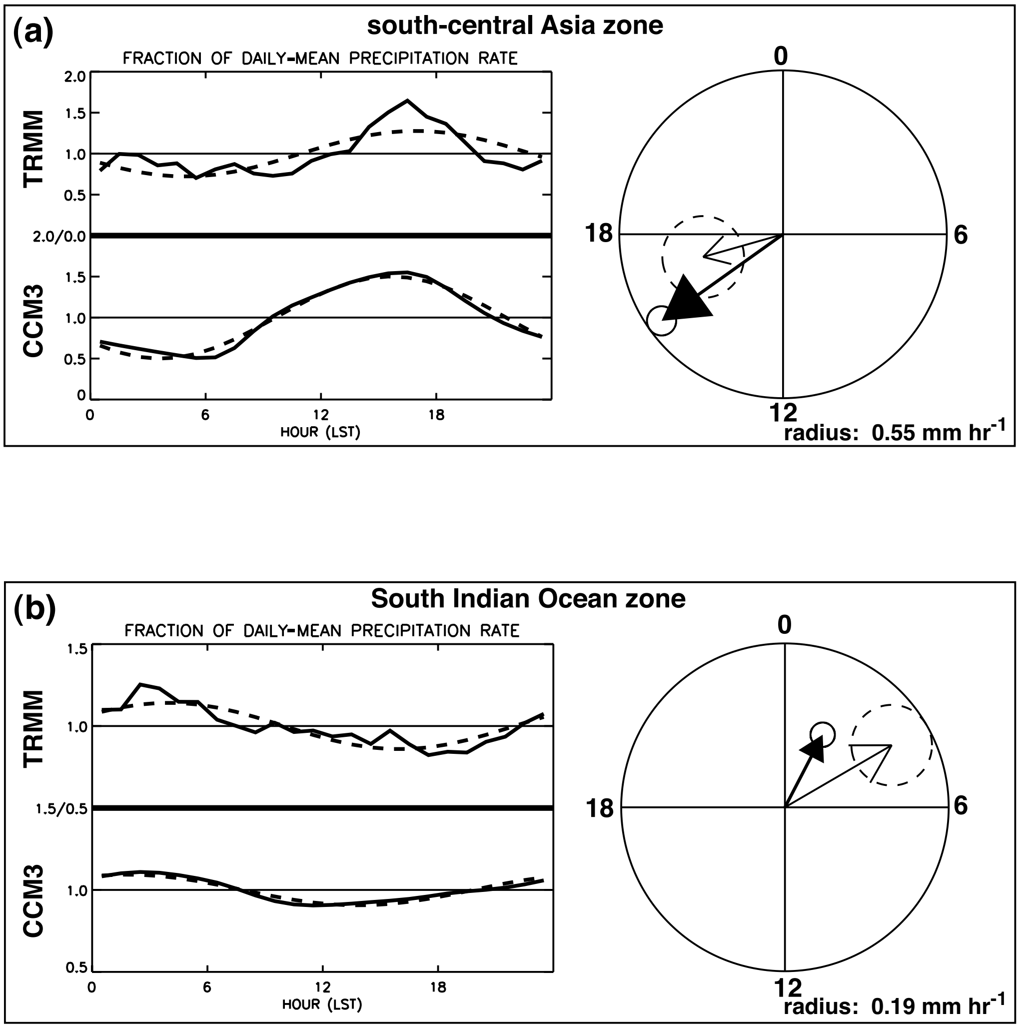

Fig. 31. Same as in Figure 24 except for the south-central Asia zone (a) and the South Indian Ocean zone (b).

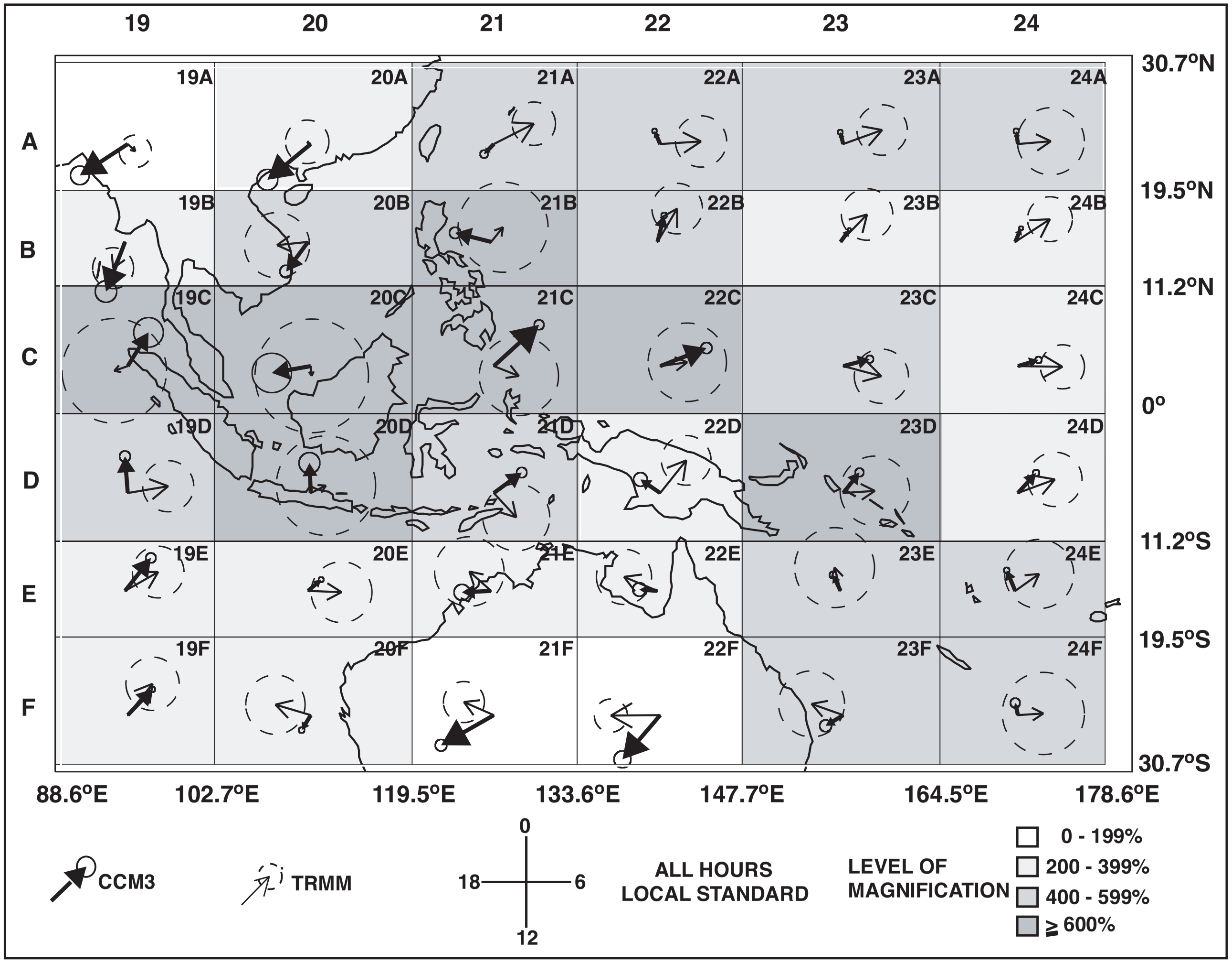

Fig. 32. Same as in Figure 22 except for regions between 90°E and the International Date Line.

the TRMM data are shown in Figure 33. The phase and amplitude comparisons for these zones are shown in Figures 34 - 35. For the southeast Asia zone (Figure 34(a)), the model simulates a moderately strong diurnal variation of precipitation, approaching 20-30% of the daily mean. Contrast this variation with that observed by TRMM over this zone: observations show little to no diurnal variation at all, which is confirmed by a poor fit to the diurnal harmonic. The fit of the CCM3 output to this harmonic is quite good by comparison and indicates a daily peak in precipitation in mid-afternoon. Thus our averaging over these regions of the Tropics indicate that the very regular diurnal variation of precipitation as simulated by the model does not compare well with TRMM observations, which indicate a variation that is much more irregular. To the south, both model and satellite show little to no diurnal cycle of precipitation over the Maritime Continent (Figure 34(b)), but partly due to the fact that we average over regions which contain both land and ocean and thus presumably very different diurnal cycles. Certainly, there is a pronounced diurnal signal over the far eastern Equatorial Indian Ocean (region 19D) and over Papua New Guinea (region 22D), as seen by TRMM and as simulated by the model. The differences in phase over these regions is noticeable: CCM3 precedes TRMM in the peak of daily rainfall by 1 to 2 hours in region 19D and by 2 to 3 hours in region 22D. Unfortunately, it would be difficult to make comparisons over the other islands in this region due to TRMM's sampling errors. The Australia zone (Figure 34(c)) is entirely land, and a pronounced diurnal signal is evident in both the model output and the satellite data. Over this zone, the difference is primarily one of phase, as magnitudes agree quite well. The CCM3 output shows an ample peak in precipitation in mid-afternoon, at least 5 hours earlier than the daily peak evident in the TRMM data (evening).

Over the ocean zones to the east (Figure 35), the TRMM diurnal signal shows up much better than on the regional scales considered above. Diurnal variations, as simulated by CCM3 and as observed by TRMM are small in these zones of the western Tropical Pacific.

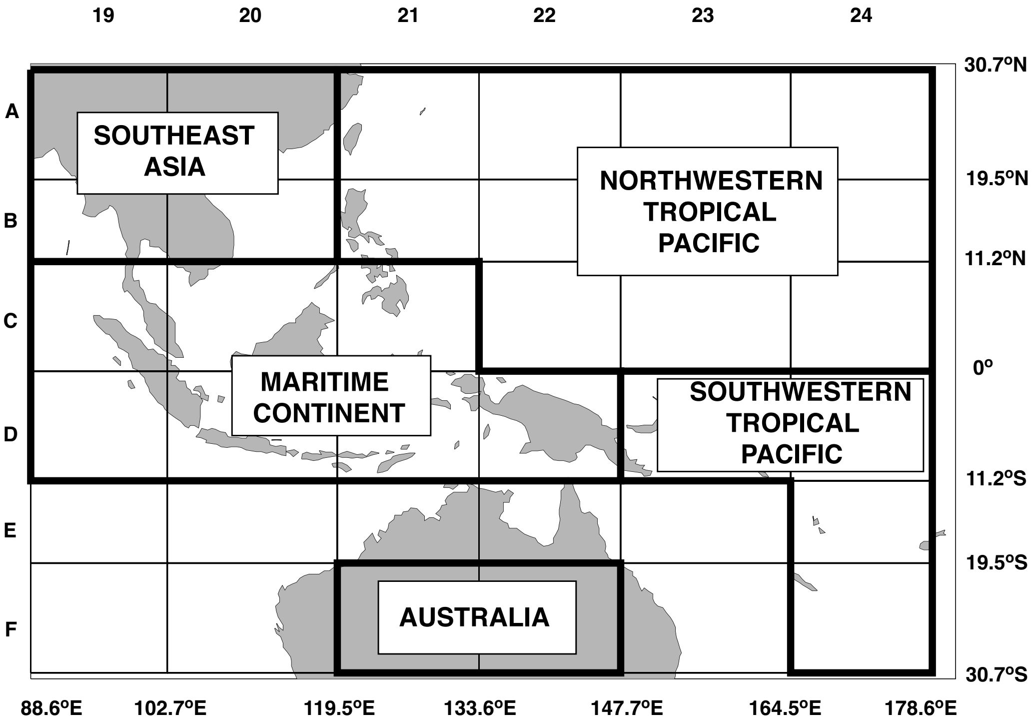

Fig. 33. Map showing the boundaries of the zones between 90°E and the International Date Line over which CCM3 and TRMM hourly precipitation rates were averaged for comparison.

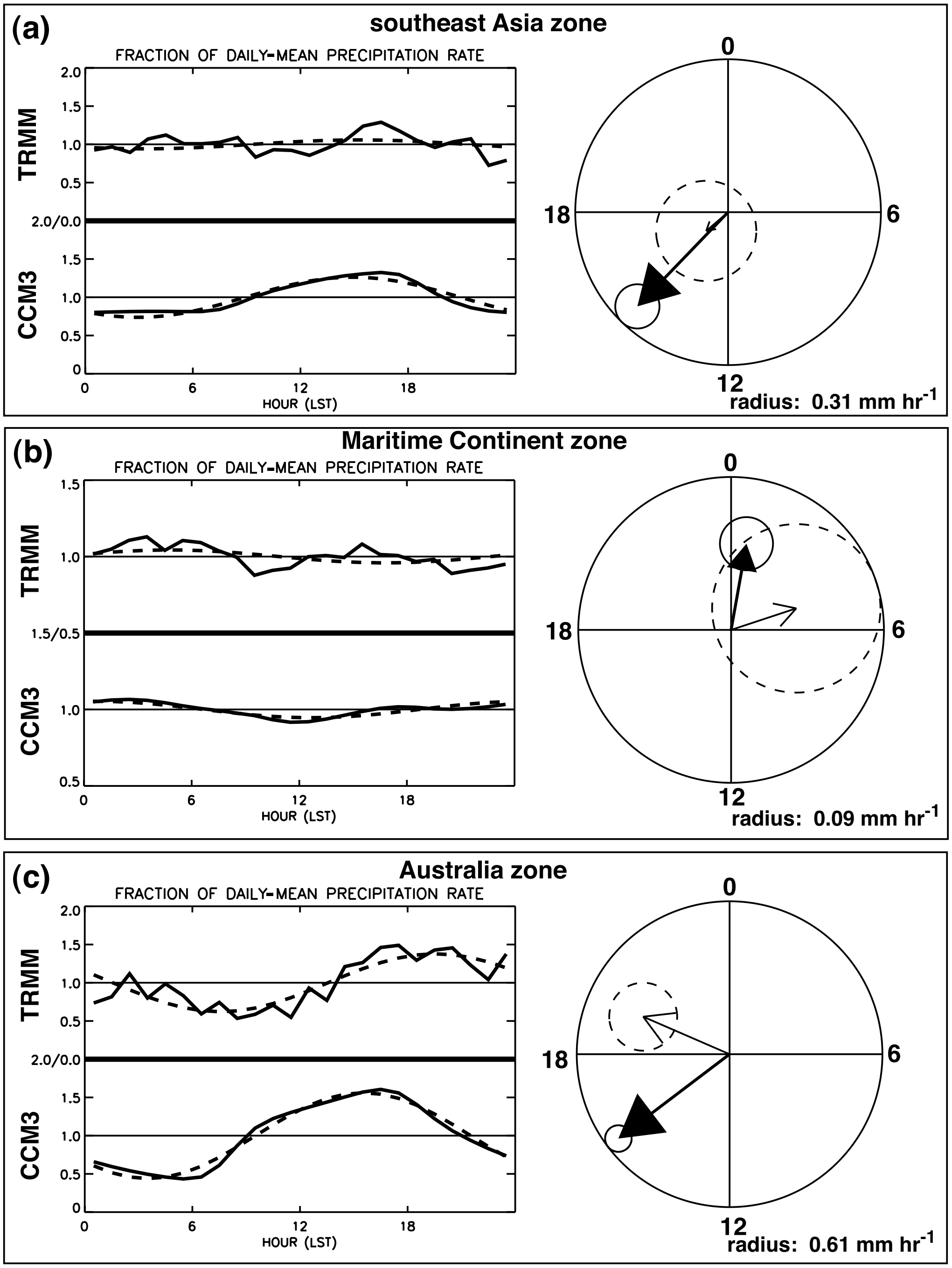

Fig. 34. Same as in Figure 24 except for the southeast Asia zone (a), the Maritime Continent zone (b), and the Australia zone (c).

The CCM3 diurnal variation is smaller than that observed by TRMM over the northwestern Tropical Pacific (Figure 35(a)) but is of comparable magnitude to the south (Figure 35(b)). Over the northwestern zone, CCM3 leads the TRMM peak by 2 to 3 hours. However in 21A, it leads TRMM by 10 to 11 hours. Over the southwestern zone, the model's peak precedes the predawn peak seen in the data, by 3 to 4 hours.

b. Summary

The results of this analysis show that, with a few exceptions, over much of the Tropical oceans and some of the Tropical land masses, comparisons on the regional scales defined are often quite difficult due to the large amount of uncertainty associated with fitting the TRMM data to a diurnal harmonic. Some of this uncertainty is due to insufficient sampling, while some is due to weak diurnal signals, especially over the ocean. When averaged over the geographical zones, the diurnal variations as observed by TRMM become more recognizable, and more straightforward comparisons can be made. We summarize the results of the comparisons within the geographical zones in Table I.

We find that, compared to the TRMM satellite data, CCM3 tends to overestimate the amplitude of the diurnal cycle of precipitation over most land masses considered in this study. The largest biases are found in the simulations over South Central Asia, northern Africa, and South America, where the model's amplitudes are respectively 80%, 84%, and 200% larger than those seen in the data. Smaller positive biases are found over southern Africa and Australia. At the same time, CCM3 tends to underestimate the amplitude of the diurnal cycle over some of the open oceans. This finding is consistent with the results for the later version of the NCAR model, CCSM2 (Dai and Trenberth 2004). Examples include the southwestern Tropical Pacific, the northern Tropical Atlantic, and the northwestern Tropical Pacific Oceans where the amplitudes are respectively 35%, 39% and 57%

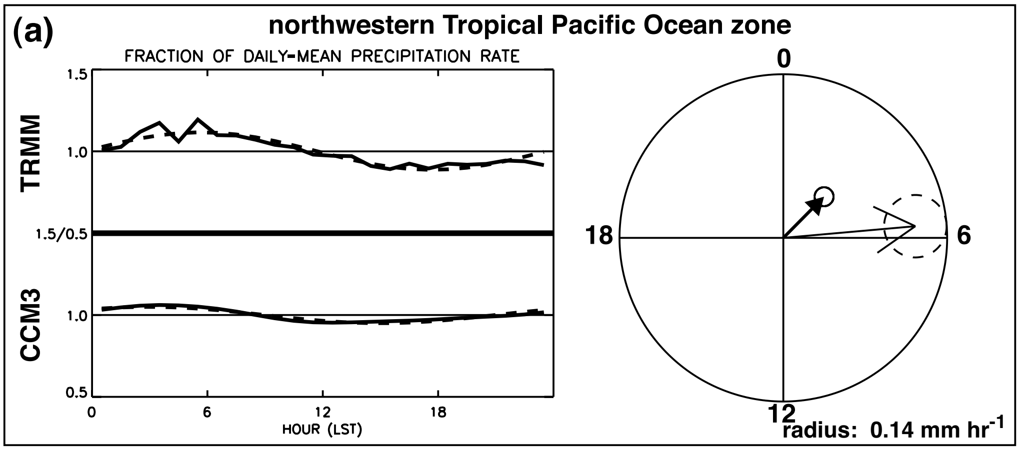

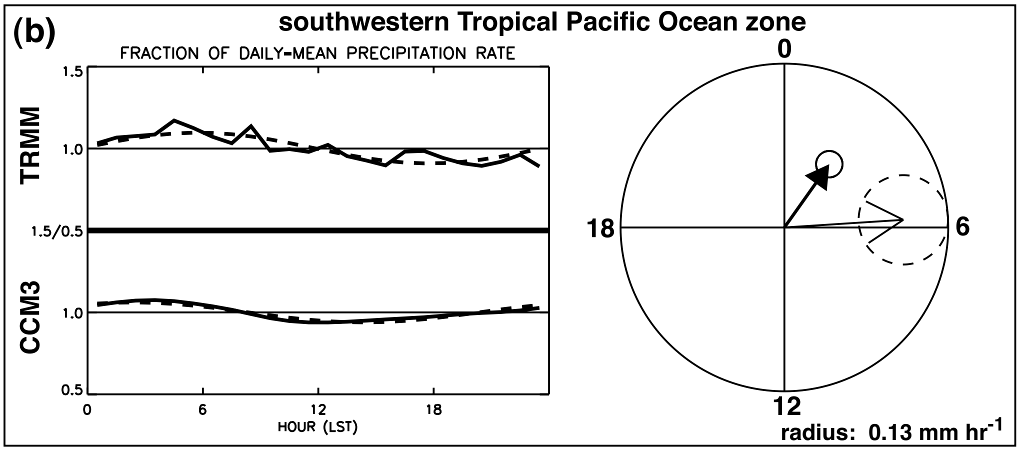

Fig. 35. Same as in Figure 24 except for the northwestern Tropical Pacific Ocean zone (a) and the southwestern Tropical Pacific Ocean zone (b).

smaller than those seen in the data. In the model, the phase of the diurnal cycle consistently precedes the data in the majority of the regions we analyze. This finding is not inconsistent with the results of (Dai and Trenberth 2004) for CCSM2, in which deep moist convection is found to initiate prematurely. Largest phase differences tend to occur over northern Africa (3 to 4 hours) and Australia (4 hours) as well as over the southern Tropical Atlantic (6 to 7 hours), though there is a large amount of uncertainty in the fitting of the TRMM data over this last zone. Elsewhere, there are isolated regions where the model-satellite phase differences are significant. For example, the model leads the data by 5 to 6 hours over Papua New Guinea and by nearly 10 to 11 hours over a region of the northwestern Tropical Pacific.

The strong forcing by the diurnal cycle of solar radiation provides an important test of the ability of climate models to simulate many processes in the climate system. The model-satellite differences detected in this study provide information that should be useful both for understanding the climatic role of convective processes and for improving parameterizations of surface and boundary-layer processes and deep convection.

Table I. CCM3 ZONE-AVERAGED DIURNAL CYCLE RELATIVE TO TRMM

ZONE	AMPLITUDE	PHASE
NE Tropical Pacific Ocean	similar[1]	precedes by approx. 2 hours
SE Tropical Pacific Ocean	similar	precedes by 3 hours
South America	200% larger[2]	similar
N Tropical Atlantic Ocean	39% smaller	precedes by 3 - 4 hours
S Tropical Atlantic Ocean	69% smaller	precedes by 6 - 7 hours[3]
N Africa	84% larger	precedes by 3 - 4 hours[4]
S Africa	67% larger	precedes by 2 - 3 hours
SC Asia	80% larger	1 - 2 hours
S Indian Ocean	similar	precedes by approx. 2 hours
SE Asia	N/A	N/A
Maritime Continent	N/A	N/A[5]
Australia	48% larger	precedes by approx. 4 hours
NW Tropical Pacific Ocean	57% smaller	precedes by 2 - 3 hours[6]
SW Tropical Pacific Ocean	35% smaller	precedes by 3 - 4 hours

---

[1] *similar*: Amplitude difference is less than 10% or phase difference is less than 1 hour.

[2] Largest in southeastern South America, region 9F.

[3] Large amount of uncertainty in TRMM fit here.

[4] Precedes by 9 to 10 hours in Saharan Desert region 13A.

[5] Precedes by 5 to 6 hours in Papua New Guinea, region 22D.

[6] Precedes by 10 to 11 hours in northwestern Tropical Pacific region 21A.

CHAPTER VI

A MODEL SENSITIVITY STUDY

When the CCM3 deep convective parameterization was first implemented in the Canadian Climate Centre GCM, the hope was that the scheme would improve upon the deficiencies of the previous parameterization, which was a simple, moist adiabatic adjustment scheme. It was found to reduce a noticeable cold bias in the tropical troposphere and to improve simulation of the Indian and southeast Asian monsoons. However, it's shortcomings were found to be that it produced too much drying in the lower levels of the atmosphere with too much cooling at the surface and that it was not considered a good parameterization for shallow convection (Zhang and McFarlane 1995). It is a complicated scheme, compared to its simple moist convective adjustment (Manabe et al. 1965) and mass flux (Arakawa and Shubert 1974; Kuo 1974; Tiedtke 1989) predecessors, but despite its complexity and its improvements, it may still be deficient at simulating well precipitation in the Tropics. The results of the above analyses indicate that there exist large biases in CCM3-simulated precipitation over various regions, as evidenced in the annual and/or diurnal cycles. It would be a difficult task to separate the contributions of precipitation by the deep-convective and shallow-convective schemes since the sum of the contributions is represented as one model variable. However, the results of a short experiment, described herein, indicate that some improvements in model-simulated precipitation biases result in parameter adjustments in the deep convective scheme of (Zhang and McFarlane 1995).

One of the only "free" parameters in the deep convective parameterization of CCM3 is the convective adjustment time scale (τ). As described above, and as can be seen from equations (2.53), (2.54), (2.34), (2.54), and (2.44), τ is the rate of $CAPE$ consumption, which governs the rate at which the adjustment to stability occurs (equation (2.53)). Cloud-base mass flux (M_b) is inversely proportional to τ (equation (2.54)), and the mass flux of an updraft (M_u) is directly proportional to M_b (equation (2.34)). The total cloud liquid water converted to rain (R_r) at any level is proportional to M_u (equation (2.43)), and total precipitation (PCP) is the sum over all levels of R_r (equation (2.44)). Therefore, it is hypothesized that changes in τ will act to change the total amount of PCP produced by the model. It is hypothesized that increasing τ will result in an overall decrease in deep convective precipitation (and thus total precipitation) but that it will increase the *duration* of precipitation events, possibly delaying the model's daily peak in precipitation so as to align it more closely with the observations.

The sensitivity test is carried out as follows. First, one of the above eight realization configurations is chosen for the test. That is, if the configuration for realization 1 is chosen, the temperature field following the experimental 1996 run will be perturbed identically. Three separate values for τ are tested, each one a percentage of the original $\tau_0 = 7200$ s (2 hours): $\tau_{1,2,3} = s_{1,2,3}\tau_0$, where s is a fraction representing the percentage. The values chosen are $\tau_1 = 0.8\tau_0 = 5760$ s (1.6 hours), $\tau_2 = 1.2\tau_0 = 8640$ s (2.4 hours), and $\tau_3 = 1.5\tau_0 = 10800$ s (3 hours). Simulations were run for a total of 28 months (i.e., from September, 1996 through December, 1998) to provide one year of output for comparison to TRMM data. Maps of the 1998 seasonal-mean CCM3-TRMM differences in total precipitation for all four values of τ (including τ_0) are shown in Figures 36 - 39.

In the seasonal-mean difference maps, some conclusions can be made. For example, in DJF, significant reductions in wet biases over the ITCZ, west-central South America, west-central and southwestern Africa, and the north-central Indian Ocean are seen for increasing τ. The reduction in wet biases appears to get larger as τ increases. Some reduction in these wet biases can be seen even for a 20% decrease in τ, though the improvement over the ITCZ is not nearly as satisfying. In MAM, the improvements with increasing τ are not as readily identifiable. The only one of any significance is over central Africa with a secondary improvement over the central Equatorial Atlantic. Elsewhere, changes in τ (de-

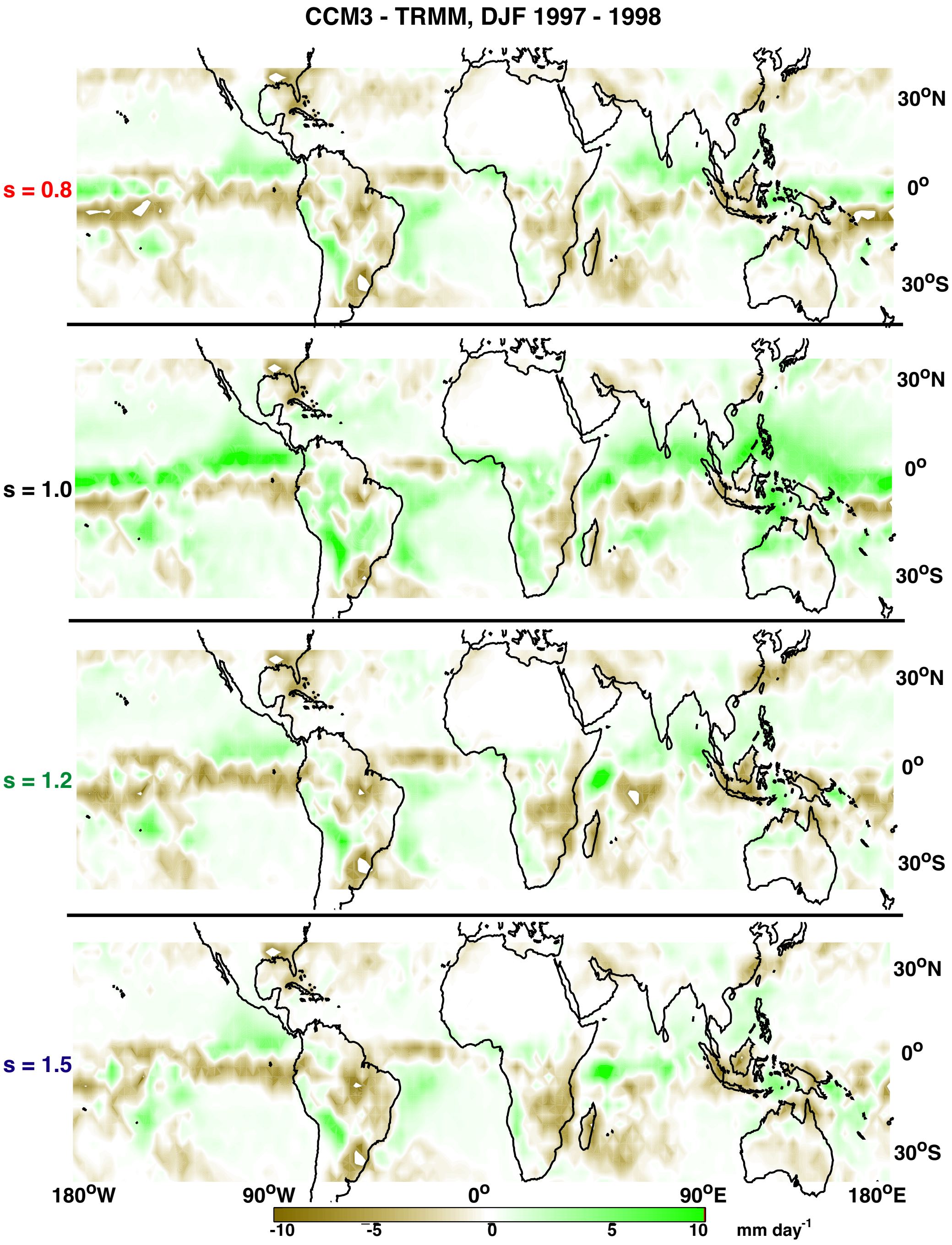

Fig. 36. Difference between CCM3 and TRMM precipitation rate (mm hr^{-1}) as averaged over DJF, 1998 for four separate values of $\tau = s\tau_0$.

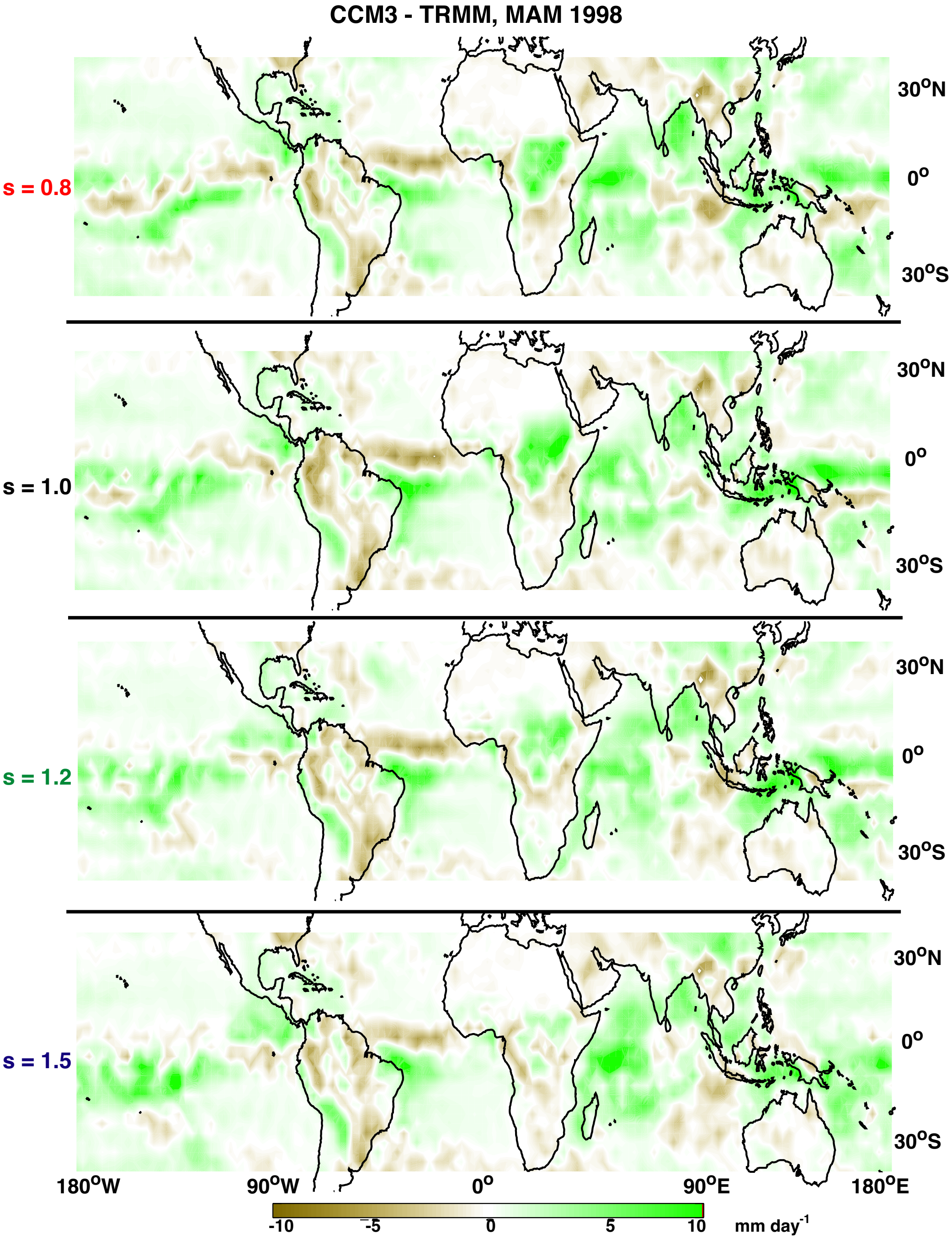

Fig. 37. Difference between CCM3 and TRMM precipitation rate (mm hr^{-1}) as averaged over MAM, 1998 for four separate values of $\tau = s\tau_0$.

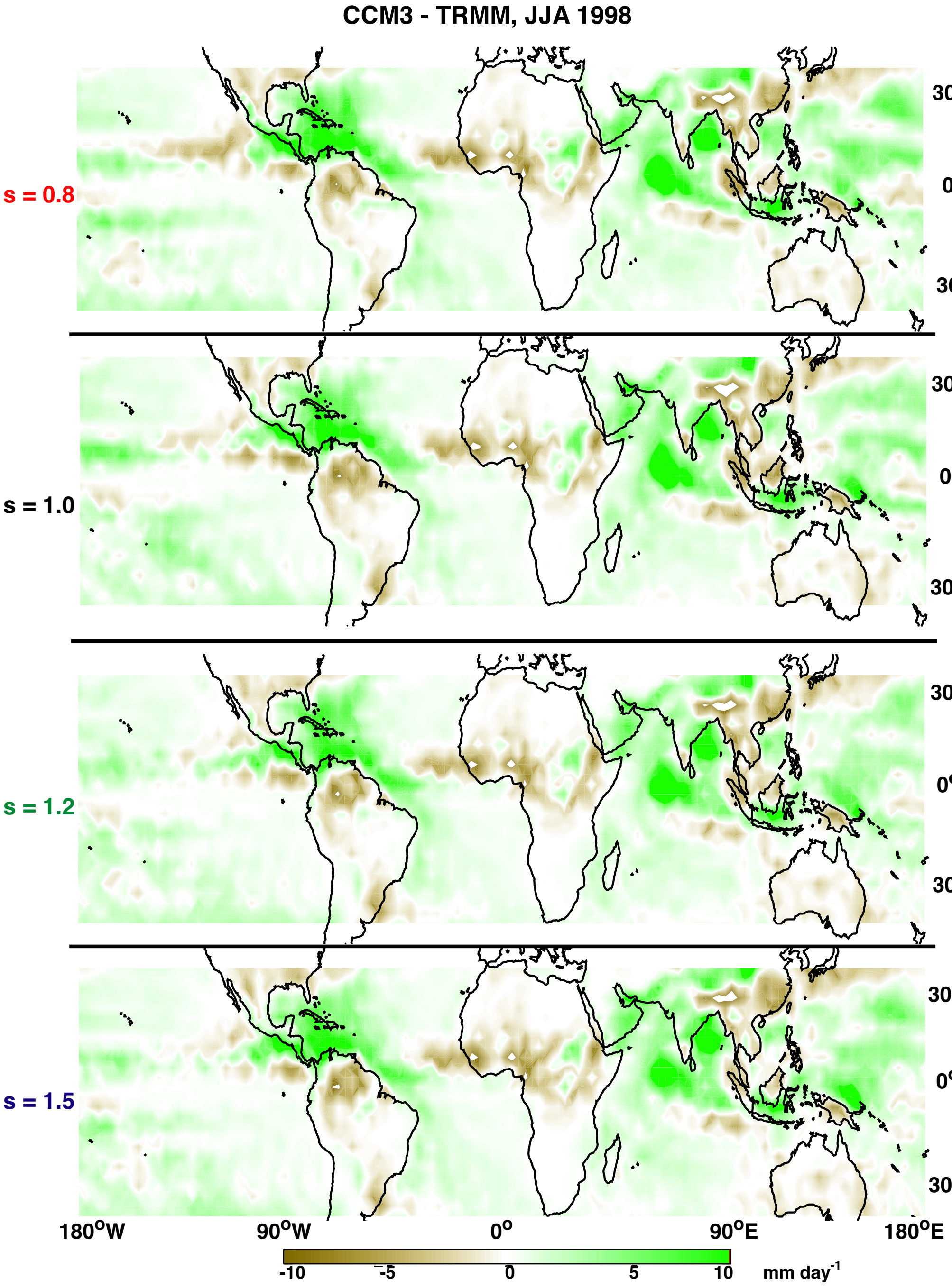

Fig. 38. Difference between CCM3 and TRMM precipitation rate (mm hr^{-1}) as averaged over JJA, 1998 for four separate values of $\tau = s\tau_0$.

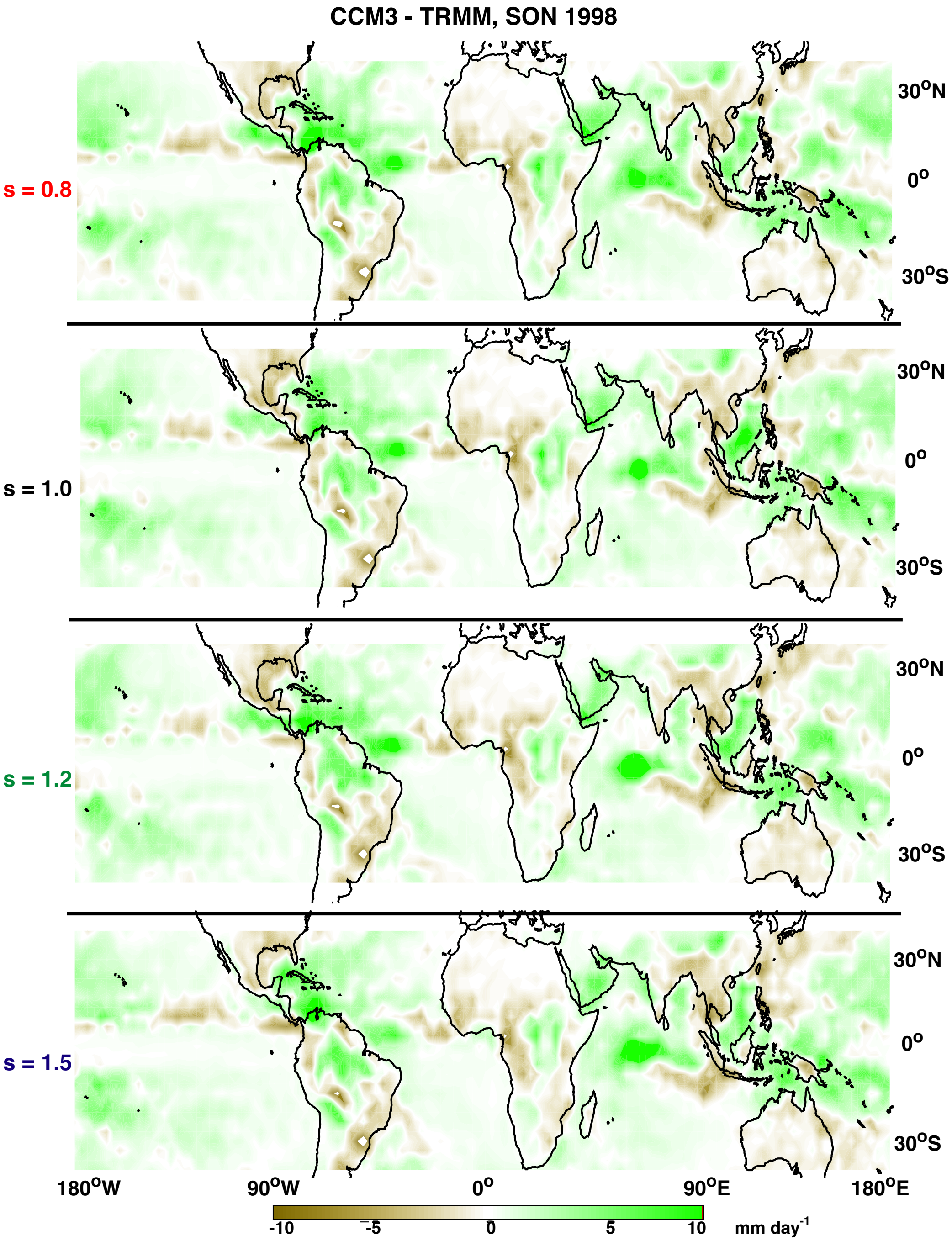

Fig. 39. Difference between CCM3 and TRMM precipitation rate (mm hr^{-1}) as averaged over SON, 1998 for four separate values of $\tau = s\tau_0$.

crease and increases) are not particularly noteworthy at this time-averaging scale. In JJA, improvements are even less noticeable. There does seem to be a decrease in the oceanic wet biases as τ increases, but the decreases are not nearly as pronounced as in DJF. One land area which sees some improvement is one of the problem regions identified in the annual cycle comparison: the Arabian peninsula. Here, the extreme wet bias appears to shrink in size as τ increases. In fact for $\tau = 1.5\tau_0$, the comparison between CCM3 and TRMM is relatively good over the southwestern tip of the peninsula. Finally, in SON, improvements for increasing values of τ are virtually nonexistent. Wet biases over the Caribbean and South America appear unaffected by changing τ. However, there is a hint of improvement in wet biases (particularly, a reduction in intensity) over central Africa and the Arabian peninsula, though these improvements are in some sense countered by an apparent increase in the wet bias over the central Indian Ocean. It is interesting to note that, aside from this one exception, increasing τ does not appear to *enhance* any wet or dry biases. Thus overall, a preliminary conclusion can be made that at certain times of the year and in certain locations, increasing τ appears to reduces model wet biases.

For a closer look at changes in the annual cycles, regional-mean monthly-mean precipitation rates are plotted for 12 geographical zones in the Tropics in Figures 40 and 41. Note that these geographical zones are the same as those defined in the diurnal cycle analysis.

The annual cycle plots indicate that there is no geographically-uniform improvement in monthly-mean precipitation rates due to increasing τ. The only geographical zones which show systematic and significant improvements in their annual cycles for increasing τ are the northern and southern Africa zones. While the smallest total difference is seen in northern Africa, the month-to-month variation appears closer to the observations in southern Africa. More interesting is the fact that some zones tend to favor a lower τ while other favor a higher τ. Thus, it becomes increasingly evident that a geographically-variable value of τ may improve the overall annual-cycle simulation in the Tropics.

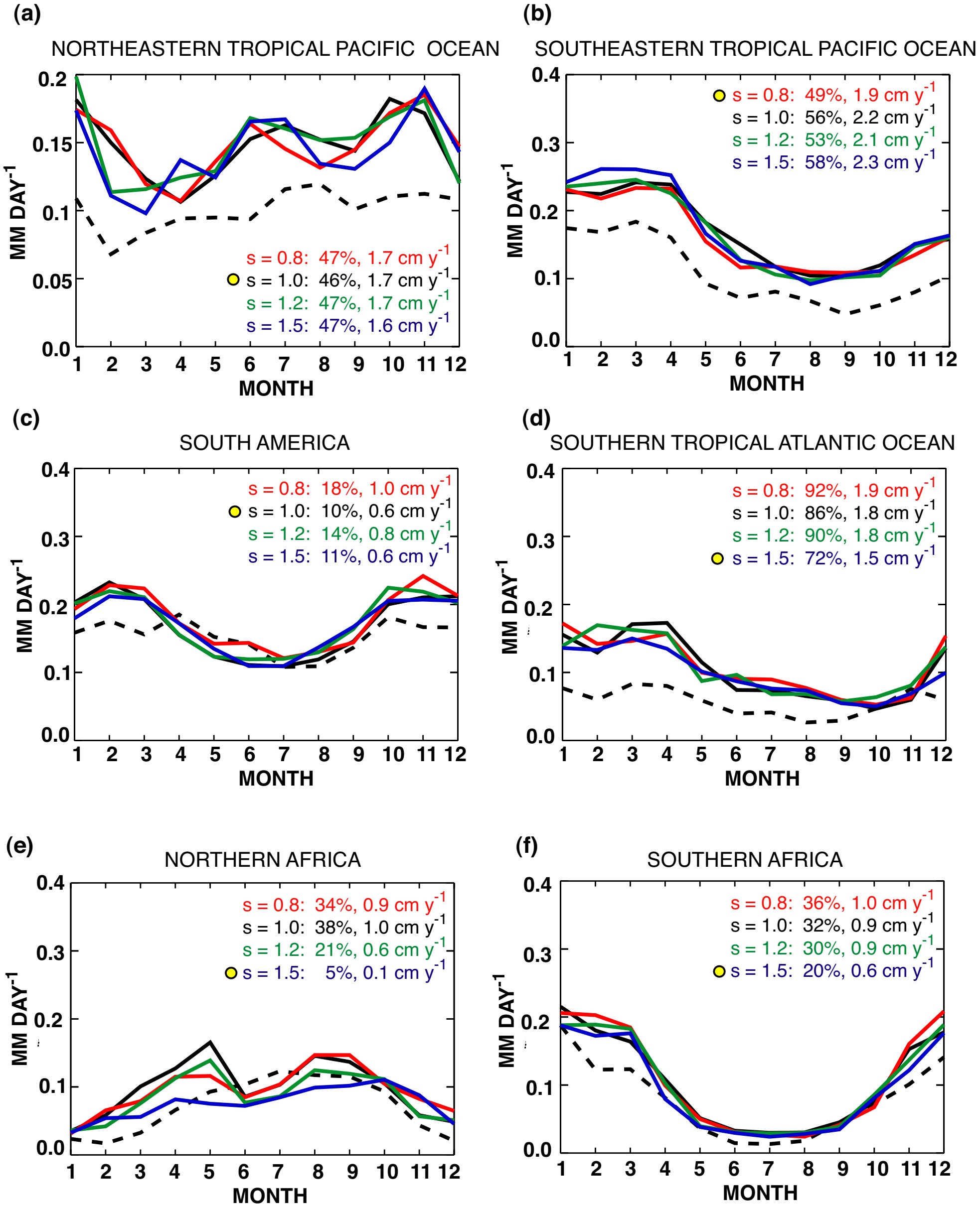

Fig. 40. Monthly-mean precipitation rates (mm day^{-1}) for 1998 for various western geographical zones in the Tropics. The red curve represents a simulation with $\tau = 0.8\tau_0$, the black curve represents a simulation with $\tau = \tau_0$, the green curve represents a simulation with $\tau = 1.2\tau_0$, and the blue curve represents a simulation with $\tau = 1.5\tau_0$. The dashed black curve represents the TRMM monthly means. Plots are annotated with the relative and absolute differences per year in % and cm y^{-1} respectively. The yellow dot indicates the "best" comparison.

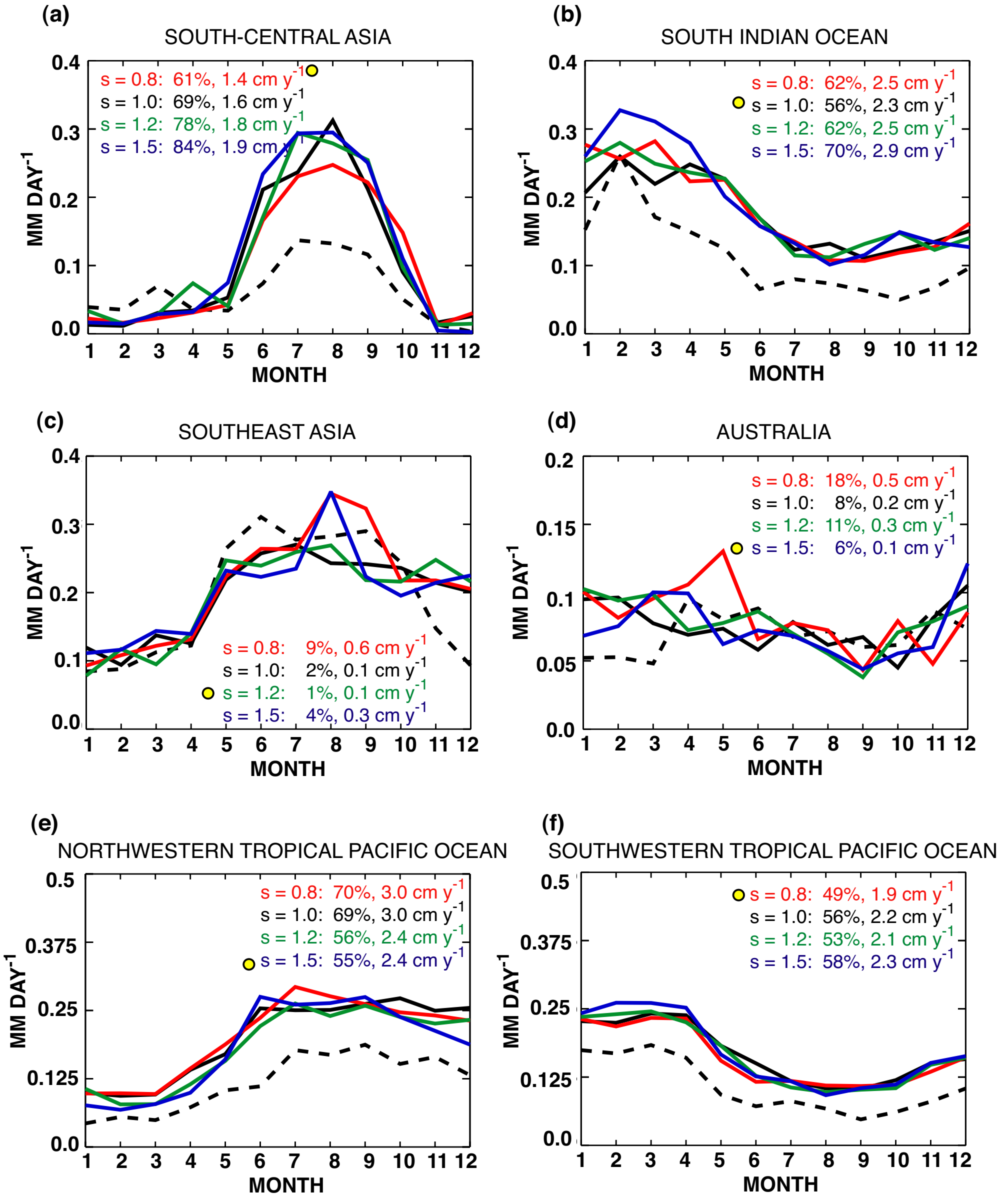

Fig. 41. Same as in Figure 40 except for eastern geographical zones.

More systematic improvements can be witnessed in the zone-mean annual-mean diurnal cycles. A closer look at changes in the diurnal cycles in the above geographical zones can be seen in Figures 42 and 43.

Increasing τ tends to reduce the diurnal cycle amplitude bias in just about all the geographical zones represented in Figures 42 and 43. Improvements are particularly pronounced over the land masses. The original hypothesis, that increasing the convective adjustment time scale would delay the peak in daily precipitation, appears to be unjustified, however, since changes in τ evidently have no effect on the phase of the diurnal cycle.

Sufficiently convinced that increasing τ decreases positive amplitude biases in the diurnal cycles of precipitation for a single year, a single simulation of $\tau = 1.5\tau_0$ was continued for the remainder of the comparison period (i.e., through August, 2001). Figures 44 and 45 show the diurnal cycles for $\tau = \tau_0$ and $\tau = 1.5\tau_0$ averaged over the comparison period.

Averaged over the 44-month comparison period, the CCM3 diurnal cycle of precipitation shows better agreement with TRMM for the longer convective adjustment time ($\tau = 1.5\tau_0$) for the land masses of South America, northern and southern Africa, south-central Asia, southeast Asia, and Australia. There is a slight improvement over the southern Tropical Atlantic, but in general, diurnal cycles in oceanic zones tend to favor the lower convective adjustment time (τ_0).

In spite of the noticeable improvements seen in the climatological-mean zone-mean diurnal cycles of Figures 44 and 45, maps of the climatological seasonal-mean CCM3-TRMM differences in precipitation are not convincing evidence that increasing τ makes any significant reduction in the model-satellite differences. These maps are shown in Figure 46 and are in some contrast with that for just 1998.

A similar experiment was conducted by (Giorgi and Shields 1999), who tested the sensitivity of the (Zhang and McFarlane 1995) deep convective scheme in a regional general

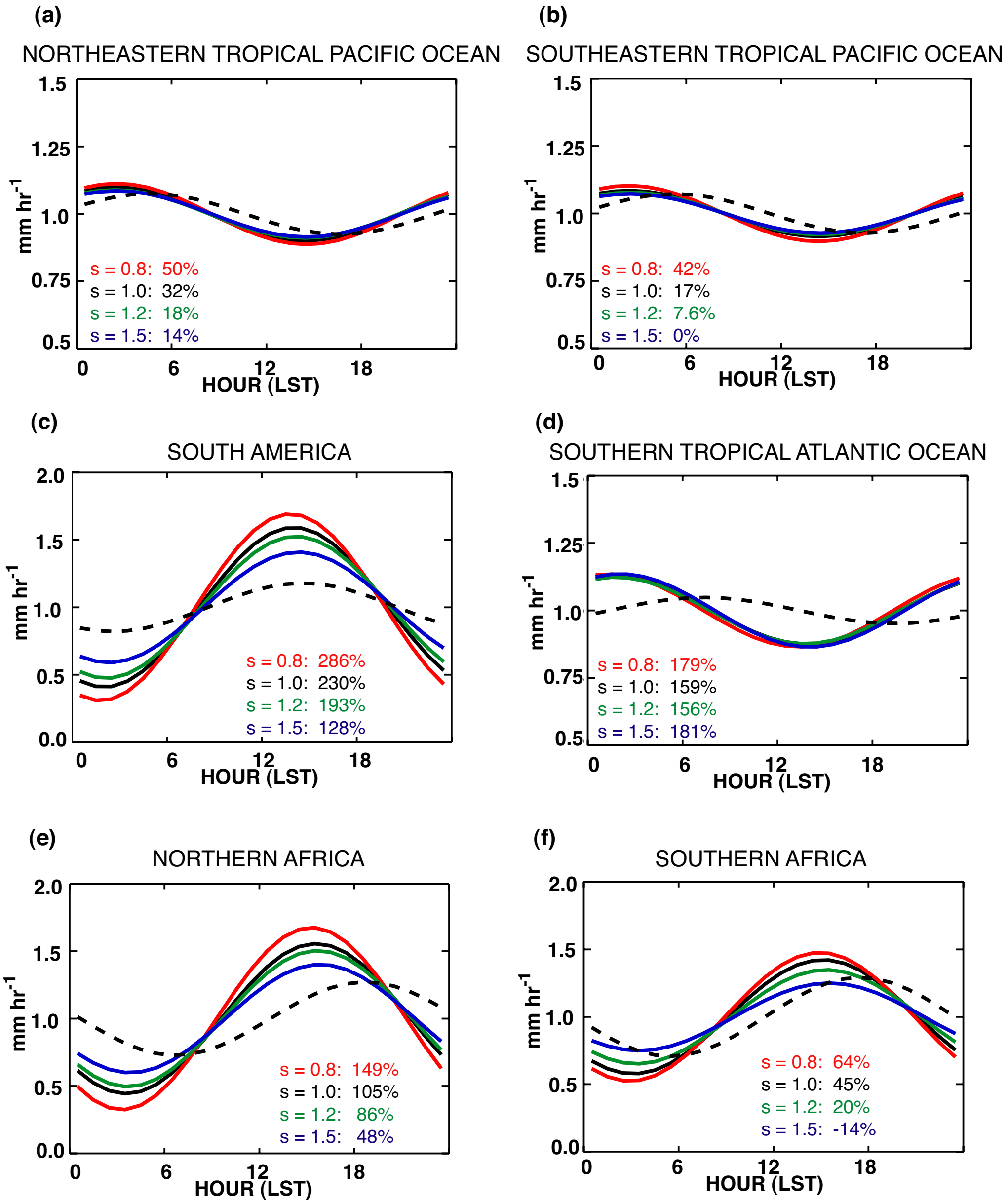

Fig. 42. Hourly-mean precipitation rates (mm hr^{-1}) averaged over 1998 for western geographical zones. The red curve represents a simulation with $\tau = 0.8\tau_0$, the black curve represents a simulation with $\tau = \tau_0$, the green curve represents a simulation with $\tau = 1.2\tau_0$, and the blue curve represents a simulation with $\tau = 1.5\tau_0$. The dashed black curve represents the TRMM monthly means. Plots are annotated with the relative differences amplitude (in %).

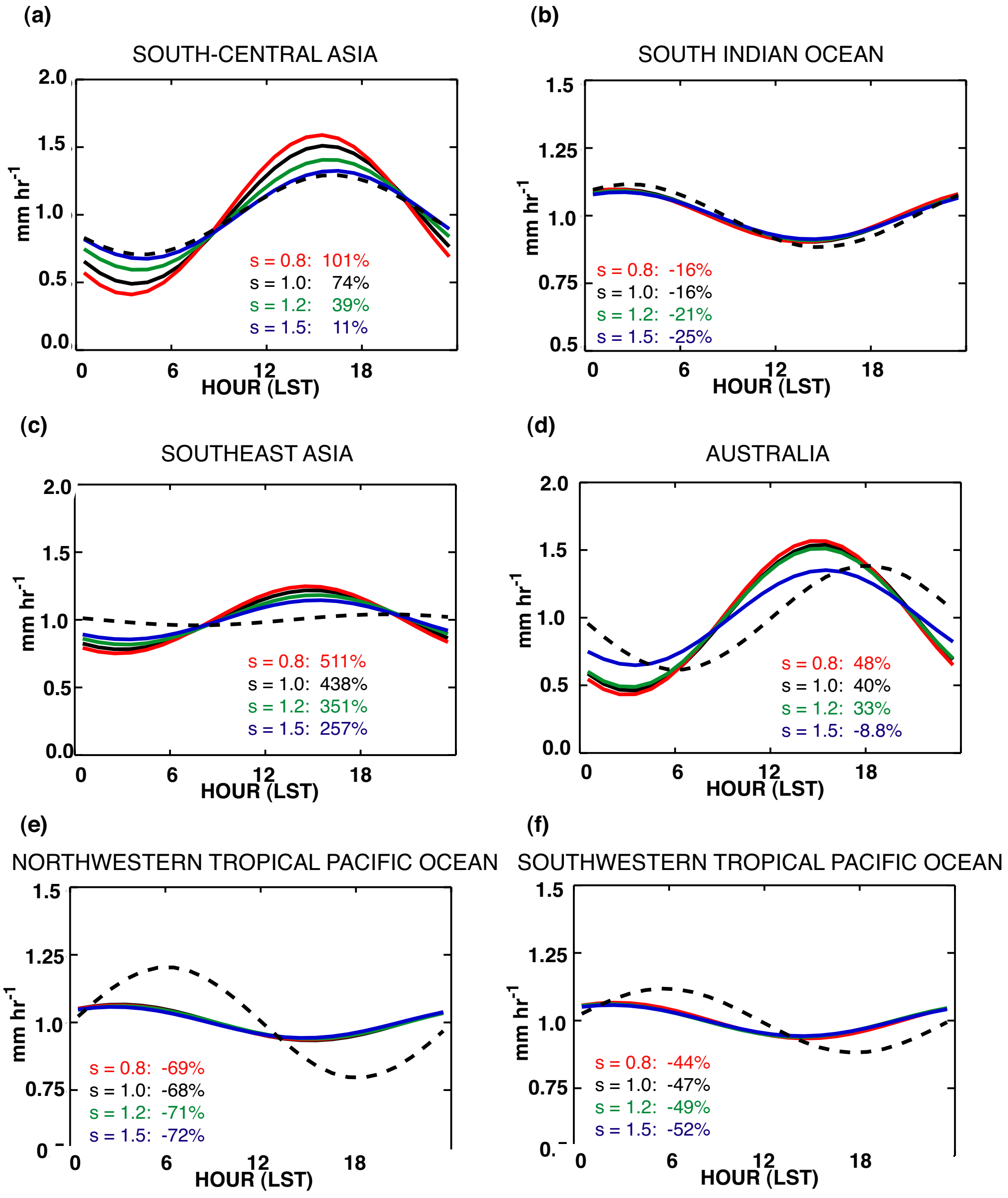

Fig. 43. Same as in Figure 42 except for eastern geographical zones.

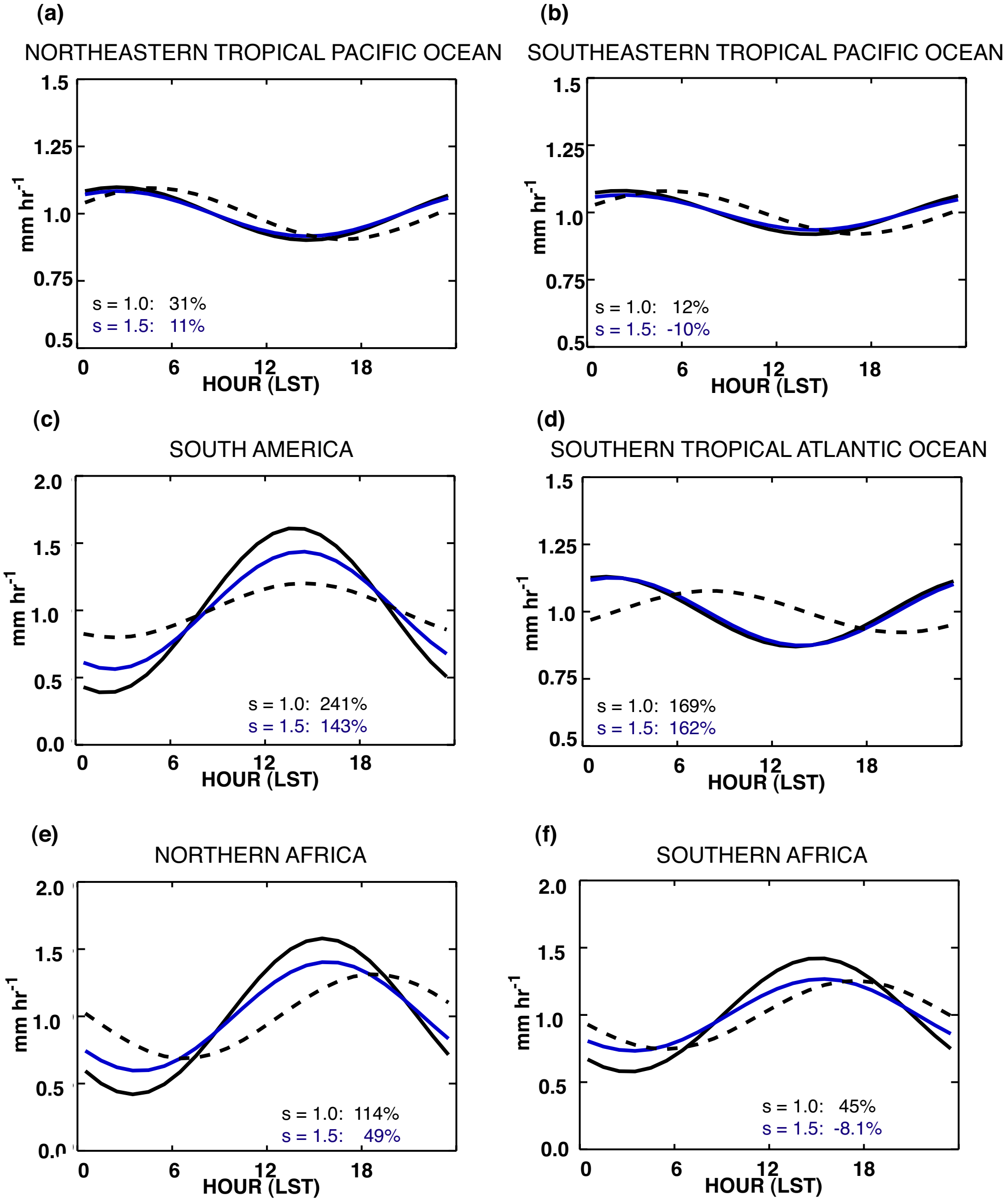

Fig. 44. Hourly-mean precipitation rates (mm hr^{-1} averaged over the 44-month comparison period for western geographical zones. The black curve represents a simulation with $\tau = \tau_0$, the blue curve represents a simulation with $\tau = 1.5\tau_0$, and the dashed black curve represents the TRMM monthly means. Plots are annotated with the relative differences amplitude (in %).

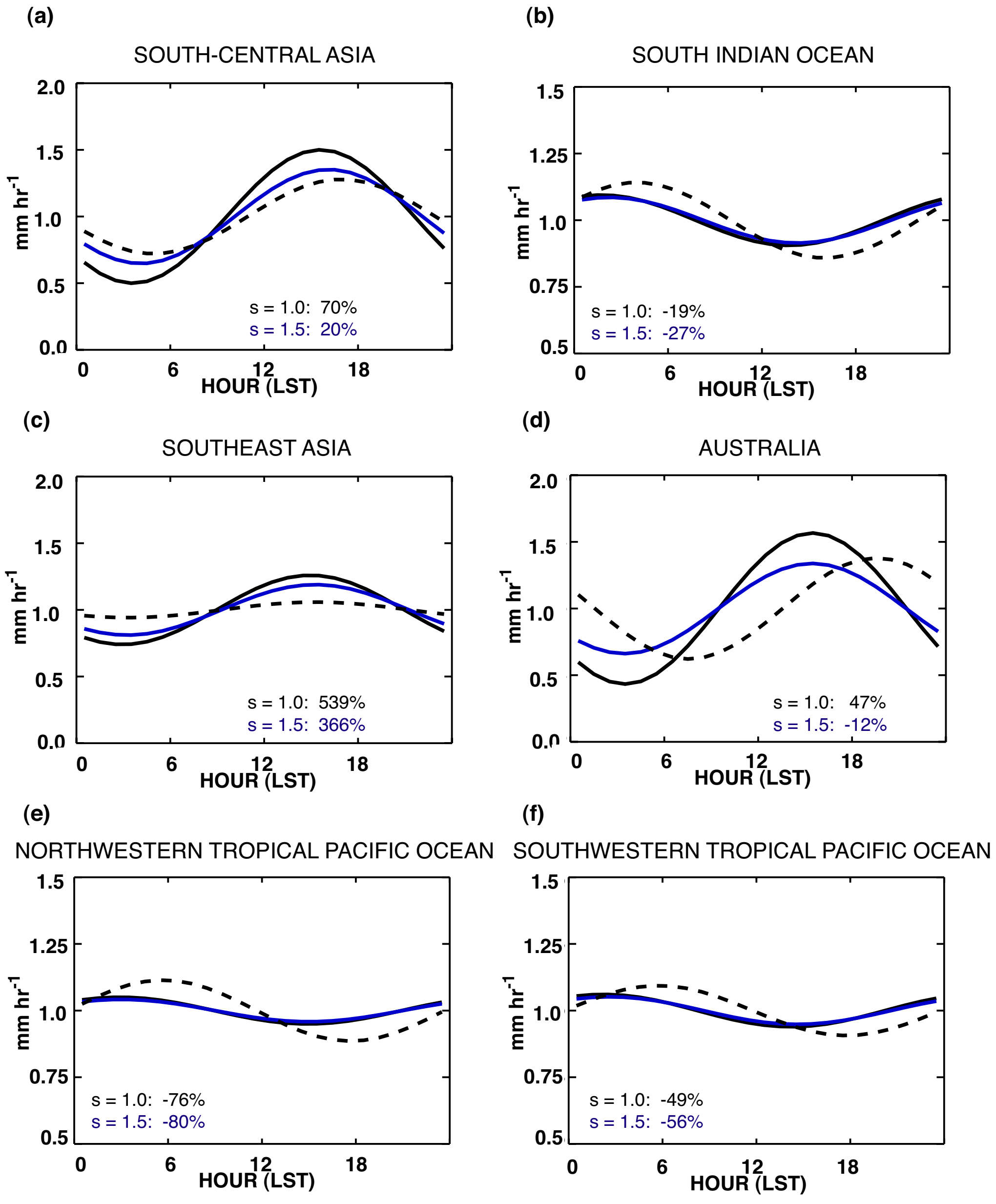

Fig. 45. Same as in Figure 44 except for eastern geographical zones.

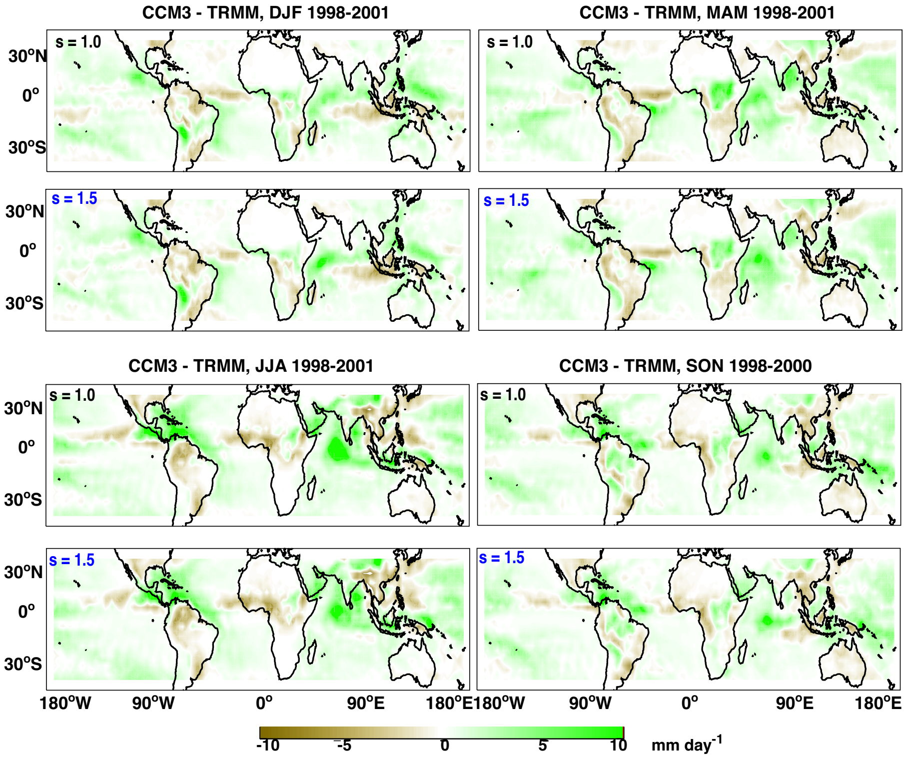

Fig. 46. Difference between CCM3 and TRMM precipitation rate (mm hr^{-1}) as averaged over 4 three month seasons for 1998-2001 for $\tau = \tau_0$ and $\tau = 1.5\tau_0$.

circulation model. Their findings indicate a general decrease in convective precipitation when τ is increased by 400%. They also find that total precipitation changes little since non-convective precipitation increases to compensate. We find that the fraction of precipitation that is non-convective (the large-scale stable form) does not change appreciably in the Tropics with a 50% increase in τ. The non-convective fraction remains at around 8%. However, the fraction of convection which is shallow or mid-level in nature *may* increase though this compensation has not been verified.

Therefore, in summary, the results of this sensitivity experiment indicate that increasing τ in the deep convective scheme of CCM3 decreases the amplitudes of the diurnal cycles over land regions in the Tropics, bringing them into closer agreement with those of the TRMM observations. In the annual average, it is difficult to ascertain any appreciable improvement in the simulation of Tropical precipitation, relative to TRMM, except during 1998. Averaging over 44 months shows little reduction in the model-satellite long-time-mean differences. It is speculated that a decrease in deep convection may be compensated by an increase in shallow and mid-level convection, resulting in little change in long-time mean averages. However, these findings need to be investigated. Since τ is also a free parameter in the shallow and mid-level convective scheme, its value could also be adjusted here as well. It appears plausible that a geographically-uniform specified value for τ may be unrealistic for simulation of precipitation over the Earth. Diurnal cycle improvements support the idea that the value of τ may need to be higher over land than over the oceans.

CHAPTER VII

SUMMARY AND CONCLUSIONS

CCM3 is a three-dimensional global spectral model that predicts all the atmospheric variables important to climate processes using prognostic equations derived from equations which specify conservations of momentum, energy, and mass, in accordance with Newton's Second Law and the First Law of Thermodynamics. For most purposes, and for the simulations in this study, CCM3 runs at a horizontal resolution of T42 which prescribes a roughly uniform horizontal grid spacing of 2.8°. In addition, the model has 18 vertical levels. Many processes in the atmosphere occur on spatial scales which are much smaller than those of the model's horizontal grid. These processes are parameterized. That is, their contributions to the tendencies of grid-scale atmospheric variables are specified explicitly in terms of grid-scale quantities. Physical parameterizations which are important to precipitation are those for deep and shallow or mid-level convection and large-scale stable condensation. The deep convective parameterization is a mass-flux scheme which characterizes updrafts and downdrafts as ensembles of plumes. The cloud base mass flux is a function of the amount of $CAPE$ consumed to eliminate hydrodynamic instability; the consumption occurs over a globally and temporally - uniform time scale. The amount of precipitation due to the convective adjustment is directly proportional to this time scale. Where the deep convective scheme fails to eliminate instability, the shallow and mid-level convective scheme assumes the responsibility. This scheme is also a mass flux scheme but does not characterize updrafts and downdrafts as does the deep convective scheme. Instead, the adjustment to stability is accomplished via transport of energy and moisture by a convective mass flux that is a complicated function of a detrainment parameter and a convective adjustment time scale, separate from the one used in the deep convective scheme. Finally, when the atmosphere is stable, but supersaturated at a location, the mass of water vapor and the temperature at this location are adjusted so as to restore unit mixing ratio. The condensate which results from this adjustment rains out; however, a fraction (roughly one fifth) is evaporated before reaching the ground to moisten the atmosphere. The combination of all processes result in the simulation of precipitation by the model.

The TRMM satellite is the product of a joint mission between the U.S. National Aeronautics and Space Administration (NASA) and the Japanese National Space Development Agency (NASDA). It was launched in November, 1997 and continues orbiting at the time of this writing. It orbits at a low inclination angle for better sampling coverage of the low latitudes of Earth. One of its primary purposes is to provide climate modelers with the horizontal distribution of latent heating in the Tropics to better improve their models. Since rain is such a good emitter and scatterer of microwave energy, a microwave radiometer and a precipitation radar are mounted on the satellite for remote retrieval of rainfall rates. This study uses the combination of measurements from both instruments for essentially instantaneous data available hourly for 0.5° by 0.5° grid boxes between 38°S and 38°N. Its sampling of a single grid box is somewhat fragmentary since it cannot view all locations at all times. Optimally, the frequency of its observation of a single 0.5° by 0.5° grid box on Earth's surface is once to twice per day at a different time each day, due to its orbital precession. Sampling errors can be large, but averaging the data on sufficiently large space and time scales helps reduce them.

This study compares precipitation simulated by CCM3 with that observed by the TRMM satellite over a 44-month period, from January, 1998 through August, 2001. Both the annual and diurnal cycles of precipitation are compared in large geographical regions. Annual cycles are compared with time series of regional-mean monthly-mean precipitation rates. Diurnal cycles are compared with time series of regional-mean comparison-period-mean hourly precipitation rates. In the comparison of annual cycles, large model wet biases are found over the western edges of the Atlantic, Indian, and Pacific Ocean basins, generally north of 10°S. Most wet biases north of the Equator are wet biases in the wet season or wet biases in model-generated artificial wet seasons. The model also exhibits wet biases over some land masses, particularly over Central America, the Congo region of Africa, and the Arabian peninsula, where it appears to simulate a monsoon every summer. In general, regional-mean monthly means agree better in the Southern Hemisphere than in the Northern Hemisphere and over land regions than over ocean regions.

The comparison of diurnal cycles shows that the model's peak in daily precipitation is biased too early just about everywhere that a significant diurnal variation exists. Largest phase differences occur over the Atlantic Ocean, northern Africa, Australia, and the southwestern Tropical Pacific Ocean. The model shows large positive biases in the amplitude of the diurnal cycle over South America, northern and southern Africa, and south-central Asia. A model sensitivity study shows that increasing the convective adjustment time scale of the deep-convective scheme reduces these large positive amplitude biases, but has no effect on reducing phase differences. Unfortunately, increasing the convective adjustment time has little effect on the model-satellite differences in seasonal-mean and annual-mean precipitation rate, which may be due to the compensatory effect of an increasing level of shallow convection. This last assertion needs to be verified.

Predictive abilities of general circulation models are limited by the unrealistic simulation of atmospheric variables such as precipitation. Precipitation in the Tropics is a primary source of energy to the general circulation of the atmosphere. Variations in its amount and horizontal distribution are manifested in the variations of other atmospheric variables. The most famous example of this manifestation is the El Niño Southern Oscillation phenomenon, whose teleconnections have been the foci of previous studies. Therefore, it is imperative that general circulation models simulate the amount of precipitation as accurately as possible, or within some range of “comfortable” values. Defining this range is a difficult statistical problem and beyond the scope of the present study. Hourly rainfall is highly non-Gaussian, which limits the use of conventional statistical tests for estimating the significance of model-data differences. Even the statistical test used in analyzing the model-satellite differences in the diurnal cycles presented herein may not even be appropriate as for several regions, the distributions of the least-squares residuals have been confirmed to be distinctly non-Guassian, even for large sample sizes. Assigning some levels of significance to the magnitudes of the differences found in this project would be a natural direction in which to proceed. Another possible, and useful, direction would be to more thoroughly investigate the source of large systematic model biases. The preliminary sensitivity study described above indicates that the source of some of the systematic biases (the diurnal cycle amplitude biases over land regions) may be in the deep-convective parameterization. Interestingly, this result, while encouraging, was not an anticipated outcome from a test which intended to measure shifts in the phase of the simulated diurnal cycle. Hence, not only is it important for GCMs to accurately simulate the amount of precipitation correctly, it is also important that they accurately simulate its distribution in time. Analyzing, and comparing to observations, its annual and diurnal cycles is a good test of how the model's physical parameterizations respond to the annual and diurnal variations in solar insolation. Evidently, CCM3 may be responding too aggressively to changes on the diurnal time scale as evidenced by its consistently-too-early peak in daily precipitation. The universality of this bias is at least as convincing as a statistical test in pleading the case for parameterization improvement.

REFERENCES

Adler, R. F., G. J. Huffman, D. T. Bolvin, S. Curtis, and E. J. Nelkin, 2000: Tropical rainfall distributions determined using TRMM combined with other satellite and rain gauge information. *J. Appl. Meteor.*, **39**, 2007–2023.

Albright, M. D., E. E. Recker, R. J. Reed, and R. Dang, 1985: The diurnal variation of deep convection and inferred precipitation in the central tropical Pacific during January-February 1979. *Mon. Wea. Rev.*, **113**, 1663–1680.

Anderson, T., 1978: *The statistical analysis of time series*. John Wiley & Sons, 704 pages.

Arakawa, A. and W. Shubert, 1974: Interaction of cumulus cloud ensemble with the large-scale environment, Part I. *J. Atmos. Sci.*, **31**, 674–701.

Barnett, T. P., 1995: Monte Carlo climate forecasting. *J. Climate*, **8**, 1005–1022.

Bell, T. L. and P. K. Kundu, 1996: A study of the sampling error in satellite rainfall estimates using optimal averaging of data and a stochastic model. *J. Climate*, **9**, 1251–1268.

— and — 2000: Dependence of satellite sampling error on monthly averaged rain rates: Comparison of simple models and recent studies. *J. Climate*, **13**, 449–462.

— and — 2003: Comparing satellite rainfall estimates with rain gauge data: Optimal strategies suggested by a spectral model. *J. Geophys. Res.*, **108**, doi:10.1029/2002JD002641.

— , — , and C. D. Kummerow, 2001: Sampling errors of SSM/I and TRMM rainfall averages: Comparison with error estimates from surface data and a simple model. *J. Appl. Metor.*, **40**, 938–954.

Betts, A. K. and C. Jakob, 2002a: Evaluation of the diurnal cycle of precipitation, surface thermodynamics, and surface fluxes in the ECMWF model using LBA data. *J. Geophys. Res.*, **107**, doi:10.1029/2001JD000427.

— 2002b: Study of diurnal cycle of convective precipitation over Amazonia using a single column model. *J. Geophys. Res.*, **107**, doi:10.1029/2002JD002264.

Bowman, K.P., 2004: Comparison of TRMM precipitation retrievals with rain gauge data from ocean buoys. *J. Climate, submitted*.

— , A. B. Phillips, and G. R. North, 2003: Comparison of TRMM rainfall retrievals with rain gauge data from the TAO/TRITON buoy array. *Geophys. Res. Letters*, in press.

Brier, G. W. and J. S. Simpson, 1969: Tropical cloudiness and precipitation related to pressure and tidal variations. *Quart. J. Roy. Meteor. Soc.*, **95**, 120–147.

Busuioc, A., H. von Storch, and R. Schnur, 1999: Verification of GCM-generated regional seasonal precipitation for current climate and of statistical downscaling estimates under changing climate conditions. *J. Climate*, **12**, 258–272.

Cess, R., 1985: Nuclear war: Illustrative effects of atmospheric smoke and dust upon solar radiation. *Climate Change*, **7**, 237–251.

Chang, A., L. Chiu, and G. Yang, 1995: Diurnal cycle of oceanic precipitation from SSM/I data. *Mon. Wea. Rev.*, **123**, 3371–3380.

Chen, M., R. E. Dickinson, X. Zeng, and A. N. Hahmann, 1996: Comparison of precipitation observed over the continental United States to that simulated by a climate model. *J. Climate*, **9**, 2233–2249.

Chen, T.-C. and M.-C. Yen, 1994: Interannual variation of the Indian monsoon simulated by the NCAR Community Climate Model: Effect of the tropical Pacific SST. *J. Climate*, **7**, 1403–1415.

Cronin, M. F. and M. J. McPhaden, 1999: Diurnal cycle of rainfall and surface salinity in the western Pacific warm pool. *Geophys. Res. Lett.*, **26**, 3465–3467.

Dai, A., 2001: Global precipitation and thunderstorm frequencies. Part II: diurnal variations. *J. Climate*, **14**, 1112–1128.

— , F. Giorgi, and K. E. Trenberth, 1999: Observed and model-simulated diurnal cycles of precipitation over the contiguous United States. *J. Geophys. Res.*, **104**, 6377–6402.

— and K. E. Trenberth, 2004: The diurnal cycle and its depiction in the Community Climate System Model. *J. Climate*, **17**, 930–951.

Deshpande, J., A. Gore, and A. Shanubhogue, 1995: *Statistical analysis of nonnormal data*. John Wiley and Sons.

Ebert, E. and J. Curry, 1992: A parameterization of ice cloud optical properties for climate models. *J. Geophys. Res.*, **97**, 3831–3836.

Espenshade, E. B., Jr, ed., 1995: *Goode's world atlas*. Rand McNally, 19th edition.

Giorgi, F. and C. Shields, 1999: Tests of precipitation parameterizations available in latest version of NCAR regional climate model (regcm) over continental United States. *J. Geophys. Res.*, **104**, 6353–6375.

Gray, W. M. and R. W. Jacobson, 1977: Diurnal variation of deep cumulus convection. *Mon. Wea. Rev.*, **105**, 1171–1188.

Hack, J., 1994: Parameterization of moist convection in the National Center for Atmospheric Research Community Climate Model (CCM2). *J. Geophys. Res.*, **99**, 5551–5568.

Henderson-Sellers, A., 1996: *A Climate Modelling Primer*. John Wiley and Sons.

Holtslag, A. and B. Boville, 1993: Local versus nonlocal boundary-layer diffusion in a global climate model. *J. Climate*, **6**, 1825–1842.

Huang, J., 2001: *An algorithm for retrieval of monthly rainfall over the oceans from the TRMM microwave imager (TMI)*. Ph.D. thesis, Texas A&M University.

Janowiak, J. E., P. A. Arkin, and M. Morrissey, 1994: An examination of the diurnal cycle in oceanic tropical rainfall using satellite and in situ data. *Mon. Wea. Rev.*, **122**, 2296–2311.

Kendrew, W., 1961: *Climates of the Continents*. Oxford University Press, 5th edition.

Kiehl, J., J. Hack, G. Bonan, B. Boville, B. Briegleb, D. Williamson, and P. Rasch, 1996: Description of the NCAR Community Climate Model (CCM3). Technical Report NCAR/TN-420+STR, NCAR, available from National Center for Atmospheric Research, Boulder, CO 80307.

Kirkyla, K. I. and S. Hameed, 1989: Harmonic analysis of the seasonal cycle in precipitation over the United States: a comparison between observations and a general circulation model. *J. Climate*, **2**, 1463–1475.

Kraus, E. B., 1963: The diurnal precipitation change over the sea. *J. Atmos. Sci.*, **20**, 551–556.

Kummerow, C., W. Barnes, T. Kozo, J. Shiue, and J. Simpson, 1998: The Tropical Rainfall Measuring Mission (TRMM) sensor package. *J. Atmos. Oceanic Technol.*, **15**, 809–817.

— , J. Simpson, O. Thiele, W. Barnes, A. Chang, E. Stocker, R. Adler, A. Hou, R. Kakar, F. Wentz, P. Ashcroft, T. Kozu, Y. Hong, K. Okamoto, T. Iguchi, H. Kuroiwa, E. Im, Z. Haddad, G. Huffman, B. Ferrier, W. Olson, E. Zipser, E. Smith, T. Wilheit, G. North, T. Krishnamurti, and K. Nakamura, 2000: The status of the Tropical Rainfall Measuring Mission (TRMM) after two years in orbit. *J. Appl. Meteor.*, **39**, 1965–1982.

Kuo, H.-L., 1974: On formation and intensification of tropical cyclones through latent heat release by cumulus convection. *J. Atmos. Sci.*, **44**, 987–1008.

Lau, K.-M. and H. Wu, 2001: Principal modes of rainfall-SST variability of the Asian summer monsoon: a reassessment of the monsoon-ENSO relationship. *J. Climate*, **14**, 2880–2895.

Lin, X., L. D. Fowler, and D. A. Randall, 2002: Flying the TRMM satellite in a general circulation model. *J. Geophys. Res.*, **107**, doi:10.1029/2001JD000619.

— , D. A. Randall, and L. D. Fowler, 2000: Diurnal variations of the hydrologic cycle and radiative fluxes: comparisons between observations and a GCM. *J. Climate*, **13**, 4159–4179.

Lindzen, R. S., 1992: Turbulence and stress swing to gravity wave and tidal breakdown. *J. Geophys. Res.*, **86**, 9707–9714.

Liou, K., 1992: *Radiation and Cloud Processes in the Atmosphere*. Oxford University Press.

Lorenz, E. N., 1963: Deterministic nonperiodic flow. *J. Atmos. Sci.*, **20**, 130–141.

Manabe, S., J. Smagorinsky, and R. Strickler, 1965: Simulated climatology of a general circulation model with a hydrologic cycle. *Mon. Wea. Rev.*, **93**, 769–798.

McFarlane, N., 1987: The effect of orographically excited wave drag on the general circulation of the lower stratosphere and troposphere. *J. Atmos. Sci.*, **44**, 1775–1800.

McGarry, M. M. and R. J. Reed, 1978: Diurnal variations in convective activity and precipitation during phases II and III of GATE. *Mon. Wea. Rev.*, **106**, 101–113.

Meisner, B. N. and P. A. Arkin, 1987: Spatial and annual variations in the diurnal cycle of large-scale tropical convective cloudiness and precipitation. *Mon. Wea. Rev.*, **115**, 2009–2032.

Mo, K. C. and R. W. Higgins, 1998: Tropical influences on California precipitation. *J. Climate*, **11**, 412–430.

Montroy, D. L., 1997: Linear relation of central and eastern North American precipitation to tropical Pacific sea surface temperature anomalies. *J. Climate*, **10**, 541–558.

Negri, A. J. and T. L. Bell, 2002: Sampling of the diurnal cycle of precipitation using TRMM. *J. Atmos. & Oceanic. Tech.*, **19**, 1333–1344.

Nesbitt, S. W. and E. J. Zipser, 2003: The diurnal cycle of rainfall and convective intensity according to three years of TRMM measurements. *J. Climate*, **16**, 1456–1475.

Pant, G. and K. R. Kumar, 1997: *Climates of South Asia*. John Wiley & Sons.

Population Reference Bureau, 2003: World population data sheet.
URL `http://www.prb.org`

Ramanathan, V., 1976: Radiative transfer within the earth's troposphere and stratosphere: A simplified radiative-convective model. *J. Atmos. Sci.*, **33**, 1330–1346.

— and P. Downey, 1986: A nonisothermal emissivity and absorptivity formulation for water vapor. *J. Geophys. Res.*, **91**, 8649–8666.

Randall, D. A., Harshvardhan, and D. A. Dazlich, 1991: Diurnal variability of the hydrologic cycle in a general circulation model. *J. Atmos. Sci.*, **48**, 40–62.

Reed, R. J. and K. D. Jaffe, 1981: Diurnal variations of summer convection over West Africa and the tropical eastern Atlantic during 1974 and 1978. *Mon. Wea. Rev.*, **109**, 2527–2534.

Robert, A. J., 1966: The integration of a low order spectral form of the primitive meteorological equations. *J. Meteor. Soc. Japan*, **44**, 237–245.

Ropelewski, C. and M. Halpert, 1987: Global and regional scale precipitation patterns associated with the El Niño/Southern Oscillation. *Mon. Wea. Review*, **115**, 1606–1626.

— 1989: Precipitation patterns associated with the high index phase of the Southern Oscillation. *J. Climate*, **2**, 268–284.

Sharma, A. K., A. T. C. Chang, and T. T. Wilheit, 1991: Estimation of the diurnal cycle of oceanic precipitation from SSM/I data. *Mon. Wea. Rev.*, **119**, 2168–2175.

Shin, K.-S. and G. R. North, 1988: Sampling error study for rainfall estimate by satellite using a stochastic model. *J. Appl. Meteor.*, **27**, 1218–1231.

Simpson, J., R. F. Adler, and G. R. North, 1988: A proposed Tropical Rainfall Measuring Mission (TRMM) satellite. *Bull. Am. Meteorol. Soc.*, **69**, 278 – 294.

Slingo, J., 1987: The development and verification of a cloud prediction scheme for the ECMWF model. *Quart. J. Roy. Meteor. Soc.*, **113**, 899–927.

— 1989: A GCM parameterization for the shortwave radiative properties of water clouds. *J. Atmos. Sci.*, **46**, 1419–1427.

Sperber, K. and T. Palmer, 1996: Interannual tropical rainfall variability in general circulation model simulations associated with the Atmospheric Model Intercomparison Project. *J. Climate*, **9**, 2727–2750.

Sundqvist, H.: 1998, Parameterization of condensation and associated clouds in models for weather prediction and general circulation simulation. *Physically Based Modelling and Simulation of Climate and Climatic Change*, Kluwer Academic Press, 433–461.

Taylor, K. E., D. Williamson, and F. Zwiers, 2000: The sea surface temperature and sea-ice concentration boundary conditions for AMIP II simulations. Technical Report 60, Program for Climate Model Diagnosis and Intercomparison, Lawrence Livermore National Laboratory.

Tiedtke, M., 1989: A comprehensive mass flux scheme for cumulus parameterization in large-scale models. *Mon. Wea. Rev.*, **117**, 1779–1800.

Tracton, M. S. and E. Kalnay, 1993: Operational ensemble prediction at the National Meteorological Center: Practical aspects. *Weather and Forecasting*, **8**, 379–398.

Trenberth, K. E., A. Dai, R. M. Rasmussen, and D. B. Parsons, 2003: The changing character of precipitation. *Bull. Am. Meteorol. Soc.*, **84**, 12051217.

Trigo, R. M. and J. P. Palutikof, 2001: Precipitation scenarios over Iberia: A comparison between direct GCM output and different downscaling techniques. *J. Climate*, **14**, 4422–4446.

Vogelzang, D. and A. Holtslag, 1996: Evaluation and model impacts of alternative boundary-layer height formulations. *Bound. -Layer Meteor.*, **81**, 245–269.

Wallace, J. M., 1975: Diurnal variations in precipitation and thunderstorm frequency over the conterminous United States. *Mon. Wea. Rev.*, **103**, 419.

Wilheit, T., A. Chang, and L. Chiu, 1991: Retrieval of monthly rainfall from microwave radiometric measurements using probability distribution functions. *J. Atmos. Oceanic Technol.*, **8**, 118–136.

— , A. Chang, M. Rao, E. Rodgers, and J. Theon, 1977: A satellite technique for quantitatively mapping rainfall over the oceans. *J. Appl. Meteor.*, **16**, 551–560.

Zhang, G. and N. A. McFarlane, 1995: Sensitivity of climate simulations to the parameterization of cumulus convection in the Canadian Climate Centre general circulation model. *Atmos.-Ocean*, **33**, 407–446.

VITA

Jonathan Craig Collier was born in Hopkinsville, Kentucky on October 6, 1975. He graduated in May, 1998 from the University of Southern Mississippi with a Bachelor of Science degree in mathematics, following completion of an undergraduate thesis on Gibbs' Phenomenon for Fourier-Bessel series approximations and two internships at the Atmospheric Turbulence and Diffusion Division of NOAA's Air Resources Laboratory in Oak Ridge, Tennessee.

In August, 1998 he began graduate school at Texas A&M University in the Department of Meteorology (later named the Department of Atmospheric Sciences) on a university regents fellowship. In December, 2000, he received a Master of Science degree for his research on the transport of tracers through zonal jets in a barotropic model. Immediately thereafter, he began his doctoral research in climate model evaluation, supported by a three-year NASA Earth System Science Fellowship. He may be reached through his parents at 6824 Shore Drive, Ocean Springs, MS 39564.